DRAG MEASUREMENT OF DIFFERENT CAR BODIES
VIA
BALANCE TECHNIQUE AND MOMENTUM INTEGRAL METHOD

A THESIS SUBMITTED TO
THE GRADUATE SCHOOL OF NATURAL AND APPLIED SCIENCES
OF
MIDDLE EAST TECHNICAL UNIVERSITY

BY

GÜLSÜM ÇAYLAN

IN PARTIAL FULFILLMENT OF THE REQUIREMENTS
FOR
THE DEGREE OF MASTER OF SCIENCE
IN
MECHANICAL ENGINEERING

JANUARY 2014

Approval of the thesis:

DRAG MEASUREMENT OF DIFFERENT CAR BODIES VIA BALANCE TECHNIQUE AND MOMENTUM INTEGRAL METHOD

submitted by **GÜLSÜM ÇAYLAN** in partial fulfillment of the requirements for the degree of **Master of Science in Mechanical Engineering Department, Middle East Technical University** by,

Prof. Dr. Canan Özgen
Dean, Graduate School of **Natural and Applied Sciences**　————————————

Prof. Dr. Süha Oral
Head of Department, **Mechanical Engineering**　————————————

Prof. Dr. Kahraman Albayrak
Supervisor, **Mechanical Engineering Dept., METU**　————————————

Examining Committee Members:

Assoc. Prof. Dr. Cemil Yamalı
Mechanical Engineering Dept., METU　————————————

Prof. Dr. Kahraman Albayrak
Mechanical Engineering Dept., METU　————————————

Assist. Prof. Dr. Cüneyt Sert
Mechanical Engineering Dept., METU　————————————

Assist. Prof. Dr. M. Metin Yavuz
Mechanical Engineering Dept., METU　————————————

Dr. Tolga Köktürk
Mechanical Engineer, ASELSAN　————————————

Date:　　**22.01.2014**

I hereby declare that all information in this document has been obtained and presented in accordance with academic rules and ethical conduct. I also declare that, as required by these rules and conduct, I have fully cited and referenced all material and results that are not original to this work.

Name, Last name   : Gülsüm Çaylan

Signature   :

ABSTRACT

DRAG MEASUREMENT OF DIFFERENT CAR BODIES
VIA
BALANCE TECHNIQUE AND MOMENTUM INTEGRAL METHOD

Çaylan, Gülsüm

M.S., Department of Mechanical Engineering

Supervisor: Prof. Dr. Kahraman Albayrak

January 2014, 118 page

In this thesis study, Ahmed Body and MIRA Notchback model were investigated experimentally.

The drag coefficients of reference models were measured at three different Reynolds number via balance technique. The wakes of reference models were also investigated and the suitable location in order to measure the drag coefficient was determined via momentum integral method.

Surface pressure of two different types of vehicle models was measured at three different Reynolds number. The wakes of Ahmed Body which has blunter shapes and sharp edges and MIRA Notchback model were investigated qualitatively by using laser and smoke and photographed.

As a conclusion, it was investigated that for Ahmed Body model the drag coefficient increased as the Reynolds number increases, for MIRA Notchback model the drag coefficient decreased while the Reynolds number increases within the investigated limits.

Keywords: Aerodynamics of road vehicles, drag, momentum integral.

ÖZ

FARKLI TİP TAŞIT MODELLERİNİN BALANS YÖNTEMİ VE İNTEGRAL
MOMENTUM YÖNTEMİ İLE
SÜRÜKLENME KUVVETİNİN ÖLÇÜLMESİ

Çaylan, Gülsüm

Yüksek Lisans, Makine Mühendisliği Bölümü

Tez Yöneticisi: Prof. Dr. Kahraman Albayrak

Ocak 2014, 118 sayfa

Bu tez çalışmasında, Ahmed Body ve MIRA Notchback model olmak üzere iki farklı tip taşıt model farklı hızlarda deneysel olarak incelenmiştir.

Üç farklı hızda sürüklenme katsayısı balans sistemi kullanılarak ölçülmüştür. Ayrıca modellerin arkasında, sürüklenme katsayısının ölçülmesi için en uygun yer integral momentum yöntemi kullanılarak tespit edilmiştir.

Aerodinamik taşıt etkileşimi üzerindeki şekil etkisinin incelenmesi için kullanılan iki farklı tip taşıt modelinin üç farklı hızdaki yüzey basınçları ölçülmüştür.

Lazer ve duman kullanılarak kaba ve keskin kenarlara sahip olan Ahmed Body ile MIRA Notchback modellerin ard izleri görsel olarak incelenmiş ve fotoğraflanmıştır.

Sonuç olarak Ahmed Body model için hız arttıkça sürüklenme kuvveti katsayısının arttığı, MIRA Notchback model için ise hız arttıkça sürüklenme katsayısının azaldığı gözlemlenmiştir.

Anahtar kelimeler: Yol taşıtlarının aerodinamiği, sürüklenme, integral momentum.

To My Father

ACKNOWLEDGEMENTS

TABLE OF CONTENTS

LIST OF TABLES

LIST OF FIGURES

LIST OF SYMBOLS

A	Frontal area, $[m^2]$
C	Cross-sectional area of the duplex test section, $[m^2]$
C_D	Drag coefficient
$C_{D_{corrected}}$	Corrected drag coefficient
C_f	Surface friction drag
C_p	Pressure coefficient
C_B*	Base pressure drag coefficient
C_K*	Forebody pressure drag coefficient
C_R*	Friction drag coefficient
C_S*	Slant part pressure drag coefficient
C_W*	Total drag coefficient
D	Drag coefficient
g	Gravitational acceleration, $[m/s^2]$
I_u	Turbulence intensity
L	Length of the vehicle, $[m]$
P_{local}	Local dynamic pressure, $[Pa]$
P_∞	Static pressure at the reference, $[Pa]$
Re	Reynolds number
$Re_{x_{crit}}$	Reynolds number at the position of completed transition
S	Cross-sectional area of the model plus its mirror image, $[m^2]$
V_{local}	Local velocity, $[m/s]$
V_∞	Free stream velocity, $[m/s]$

V	Velocity of the vehicle, [m/s]
V_c	Corrected velocity, [m/s]
q	Uncorrected dynamic pressure, [Pa]
q_c	Corrected dynamic pressure, [Pa]
x_{crit}	Position of the completed transition, [m]
α	Yaw angle, [Degree]
φ	Rear slant angle, [Degree]
δ	Boundary layer thickness, [m]
$δ^*$	Displacement thickness, [m]
ε	Equivalent roughness height, [m]
μ	Absolute viscosity, [N.s/m^2]
ρ	Fluid density, [kg/m^3]
τ	Shear stress, [N/m^2]
ν	Kinematic viscosity, [m^2/s]
θ	Momentum loss thickness, [m]

CHAPTER 1

INTRODUCTION

In earlier times, the development in aerodynamic areas was carried out independent of automobile industry. The thermal engine was started to be used instead of horses about more than 100 years ago, the aerodynamics was not taken into consideration. Protecting the driver and passengers from wind, rain or mud were the main objective in those years. The importance of road vehicle aerodynamics realized after aerospace and naval technology had advanced significantly. Then, aerospace or naval industry aerodynamic principles were applied to automobile industry. But, it was understood that this approach was wrong. The most important issues for automobile industry are the increase in fuel consumption due to the air flow resistance and instability. The aerodynamic instability is the inability to clutch ground. In addition eddies on the surface caused by air separation makes controlling the road vehicles difficult. Thus, new opinions were offered. Then, many studies were conducted on aerodynamic of automobiles. Automobile designs were improved with respect to needs and economical reasons. In these days, fashion, technology, regulations, economic and competitive environment, traffic policy and social considerations affect the car concept. There should be a careful balance between them [1].
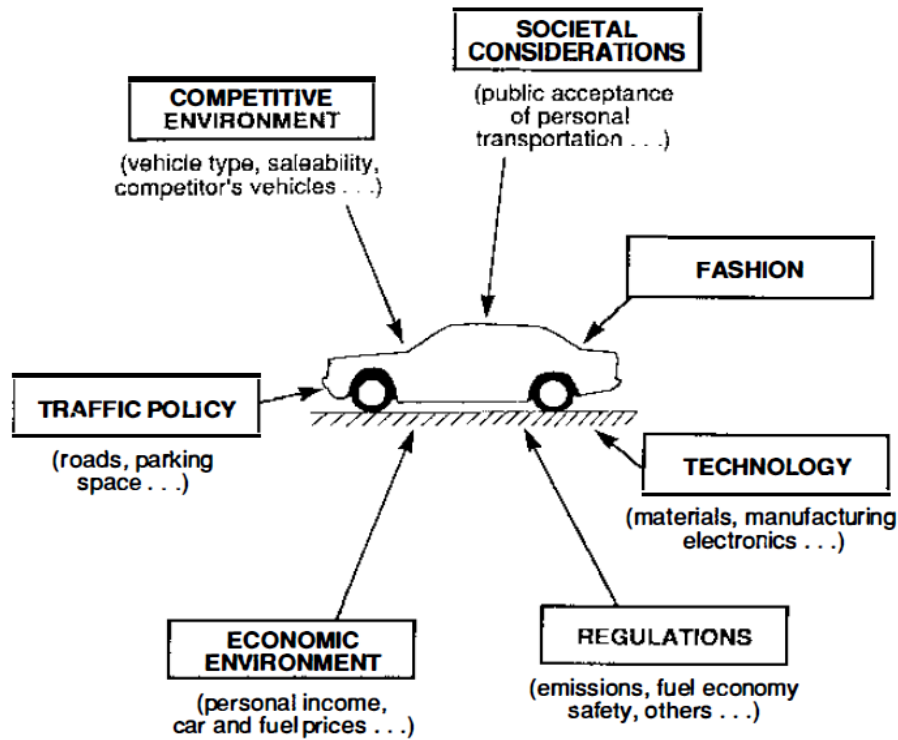
Figure 1.1 The Concept of a Car [1]

In fluid mechanics, the road vehicles are considered as bluff bodies. The road vehicle geometry is complex. The flow around the vehicle is three-dimensional. The turbulent boundary layers, flow separations and turbulent wakes occur. For bluff bodies, the main contribution to drag is the pressure drag. Hence, reduction or control of the separation of flow is the main objective in aerodynamic analysis. Function, economics, aesthetics are also important in road vehicle design [1].

In this study, the drag of vehicle models is analyzed experimentally. In Chapter 2, some previous work about reference models are presented. In Chapter 3, the air flows around the road vehicles are summarized. In Chapter 4, the experimental instrumentations and set-ups are introduced. In Chapter 5, calibrations and procedure of the experiments are described. In Chapter 6, the results of experiments and discussions are explained. Lastly, conclusions and recommendations of future work are stated in Chapter 7.

CHAPTER 2

PREVIOUS WORK

Road vehicle aerodynamics influence the performance of a ground vehicle in many ways. Fuel efficiency, stability, handling and noise levels of a vehicle are affected by aerodynamics. To understand the air flow around a road vehicle, designers have conducted the experimental tests in the wind tunnel. There are many important parameters that influence the ground vehicle aerodynamic characteristics. One of them is a wake structure. The major contribution to a drag of the vehicle is the wake flow behind the car. The region of flow separating defines the size of the separation region and the force of drag. In this study, it is intended to investigate the drag on reference models. To carry out these aims, former studies about Ahmed Body and MIRA Notchback car vehicle models are represented.

Ahmed et al [2] described a simply vehicle body to understand the distribution of surface pressure, the structure of the wake and the effects of the rear slant angle on the structure of the wake.
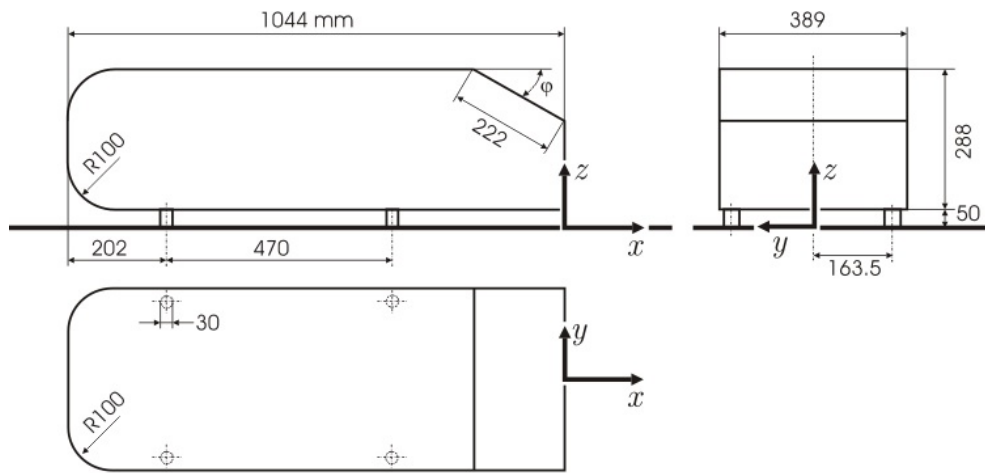
Figure 2.1 Ahmed Body [2]

A research was conducted at $\varphi = 5°,\ 12.5°,$ and $30°$ for high drag and $30°$ for low drag to figure out the relative addition to the drag from pressure on the slant, base and nose. In the symmetry plane, in order to obtain the low drag flow, a vertical splitter plate was used in the wake of the $30°$. Techniques of visualization were used to investigate the wake structure. Time- averaged velocity measurement were employed on the plane of centerline and at transverse plane in the wake. Total drag measurement was conducted for angles of slant from $\varphi\ =\ 0°\ to\ \varphi\ =\ 40°$.
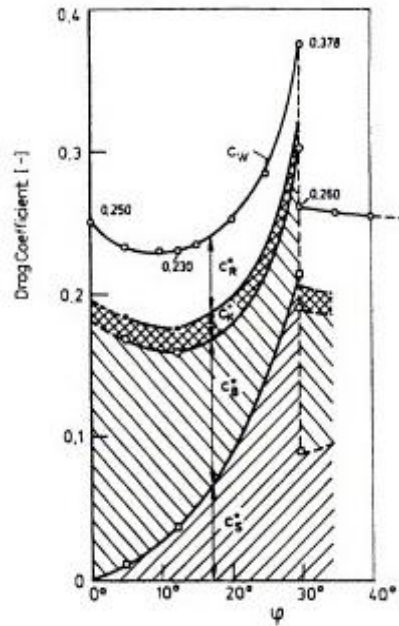
Figure 2.2 Variation of Drag with Base Slant Angle [2]

where

C_S* : slant part pressure drag coefficient

C_R* : friction drag coefficient

C_B* : base pressure drag coefficient

C_K* : forebody pressure drag coefficient

C_W* : total drag coefficient

These drag coefficient components retain specific flow features. Pressure drag coefficients were derived assuming mean values of the measured pressure to exist over the entire base, forebody or slant part area.

Configurations of time-averaged wake structure sketches for the low drag $\varphi \approx 20°$ and high drag $\varphi \approx 30°$, shown in Figure 2.3. The flow was fully attached over the

20° slant angle. There were two horseshoe vortices at downstream of the base of the Ahmed Body. These two horseshoe vortices interact with the flow which is leaving the slant, the vortices of the side-edge and the underside of the body flow. The strength of the vortices of side-edge and separation bubble formed at the slant leading edge.
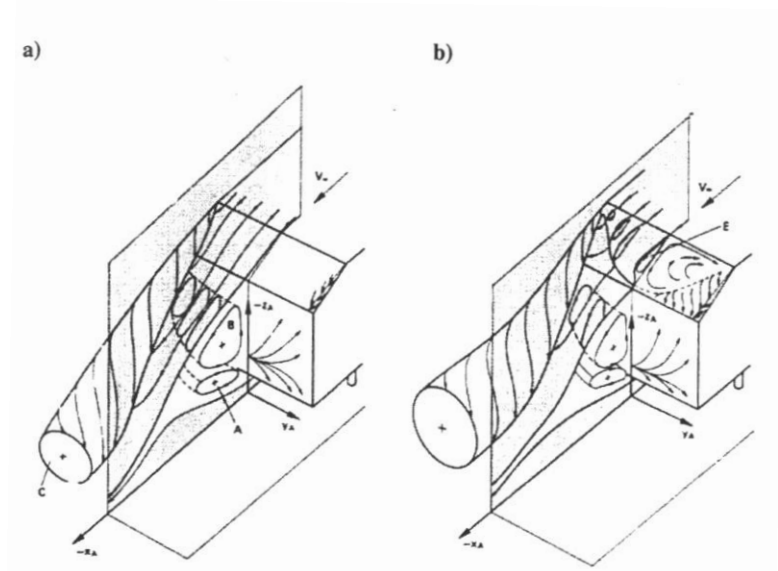
Figure 2.3 Time-averaged wake structure of the Ahmed Body [2]:a) Low Drag Flow (20°), b) High Drag Flow (30°)

Using the technique of smoke flow structures, Sims-Williams [3] did a study on time-averaged and unsteady flow structures. Using the same geometry, Sims-Williams showed the sensitivity of the flow pattern near the critical backlight angle. They conducted a detailed study when the tunnel was operated from the rest. At the beginning the state of flow would be in the low drag. After a few a minutes later, the state of flow would change to the high drag. The state would maintain indefinitely. The lower the free stream speed is, the longer the low drag flow state would become. These mentioned two flow states are shown in Figure2.4.
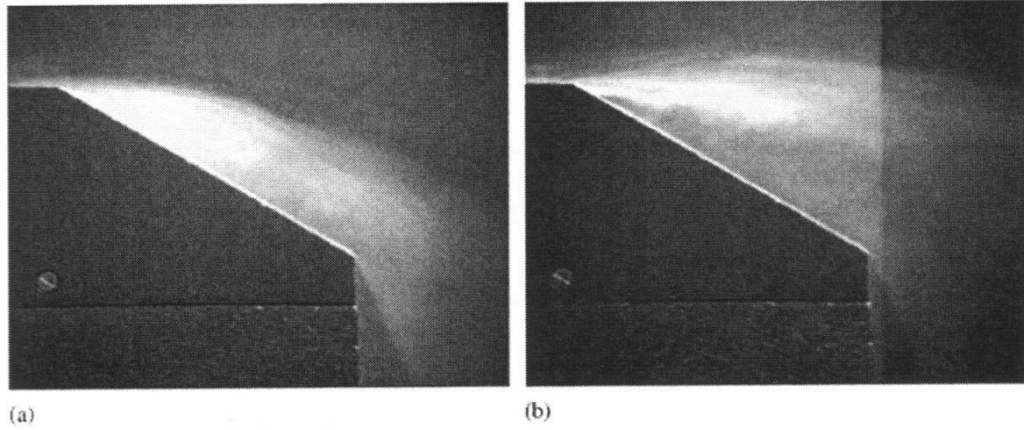
Figure 2.4 High and Low Drag Structures at the Same Backlight Angle of 30° [3] :a) Low Drag Flow (30°), b) High Drag Flow (30°).

Duell and George [4] and Berger et al [5] suggested that a link between the shedding from the base and the pumping at the free stagnation point through repeated vortex pairing in the shear layers. In this study, Duell and George stated that on one side vortices of shear layer firstly were shed uniformly and then sideways from the upper part of the vehicle. After the course started, the shear layer vortex was shed uniformly from the opposed side then sideways from the base of the vehicle. The shear layer vortex was combined to the next vortex which was shed uniformly from the original site. The structure of vortex is formed as pseudo-helical vortex structure in the shear layer. Vortex pairing occurred as vortices were convected downstream in the shear layer [4].

The resulting vortex characteristic frequency has decreased by the pair of vortex. The average length of circulation was defined as a major important characteristic property of the near wake circulation zone by George and Duell [4]. The length of circulation is symbolized as X_r and was defined as distance between the bottom of the model and the average location of the free stagnation point. When the distance from the separation point on the vehicle is increased, the characteristic frequency in the shear layer is decreased velocity power spectral density distinctive peak gauged at $0.266X_r$. The vehicle schematic view and average near wake throughout X-Z coordinate at

Y=0 is demonstrated in Figure 2.5. In addition, Figure 2.5 shows eddies in the shear layer, final vortex shedding, resulting in free stagnation point fluctuations [4].
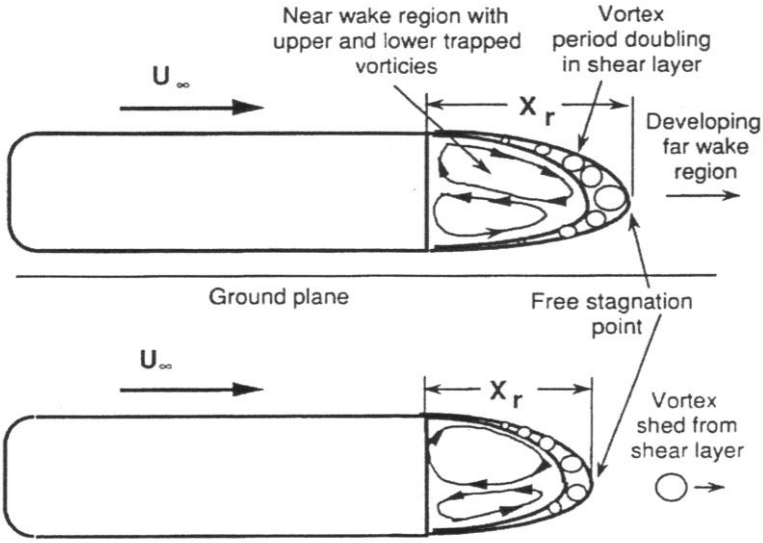
Figure 2.5 Schematic View of the Model and Mean near Wake along X-Z Plane atY=0 at Two Successive Times [4]

Templin and Raimando [6] tested MIRA Notchback models in DSMA closed test section wind tunnel. 0.2, 0.25 and 0.3 scale models were tested by a pressure signature method. Wall interference was researched experimentally. In this study, one solid and two open area ratio slotted wall test section was used. Using three different scale MIRA Notchback models, the blockage interference was investigated for 8.3%, 13.0% and 18.7% area blockage. Wall-induced interference speed at the vehicle position for the solid wall test-section determined with this method. Free air pressures were measured in the 30% slotted wall test sections. Then, comparison was made between the measured and predicted free air pressures. These experiments indicated that a practically interference free testing medium can be provided with a slotted wall test section. Figure 2.6 indicates basic dimensions of the MIRA Notchback car model.
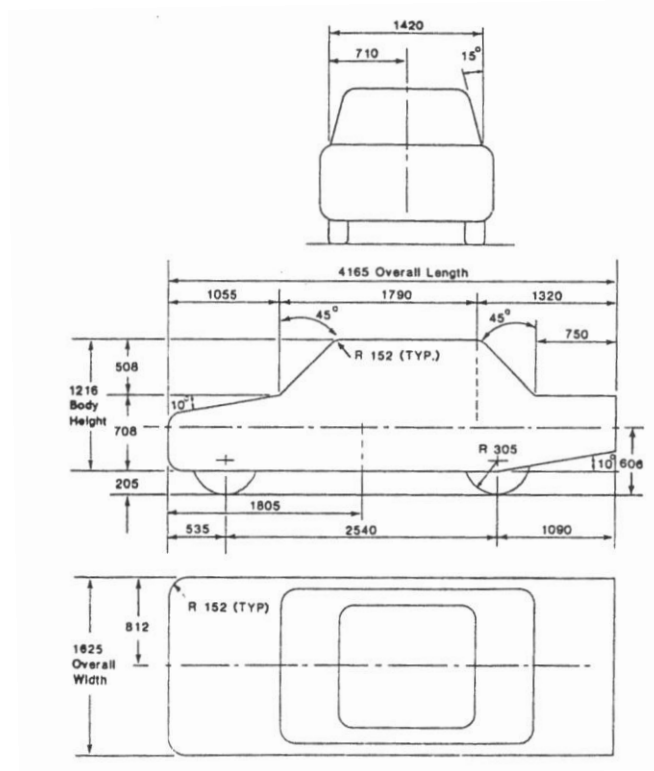
Figure 2.6 MIRA Notchback Car Model [6]

Jack Williams et al [7] tested different scale MIRA Notchback models to compare relative aerodynamic simulation quality. In that study, semi-open jet and slotted wall in Ford/Sverdrup drivability test facility was used. Four MIRA Notchback model and six sport utility vehicles were used. Tests were made for 7%, 11%, 15%, 20%, and 25% area blockage. An external strain gage balance was used in order to measure six component force and moment. A signal conditioning unit was used to amplify the output of strain gage. Experiments were conducted at 1×10^6 Reynolds number for all vehicle models. To obtain the Reynolds number for each model the tunnel speed was altered to balance for the different vehicle model lengths. The boundary layer displacement thickness changed because of alteration in tunnel speed. These experiments showed that the largest model was the best. The C_D vs. the model blockage configuration for the MIRA Notchback model is shown in Figure 2.7.
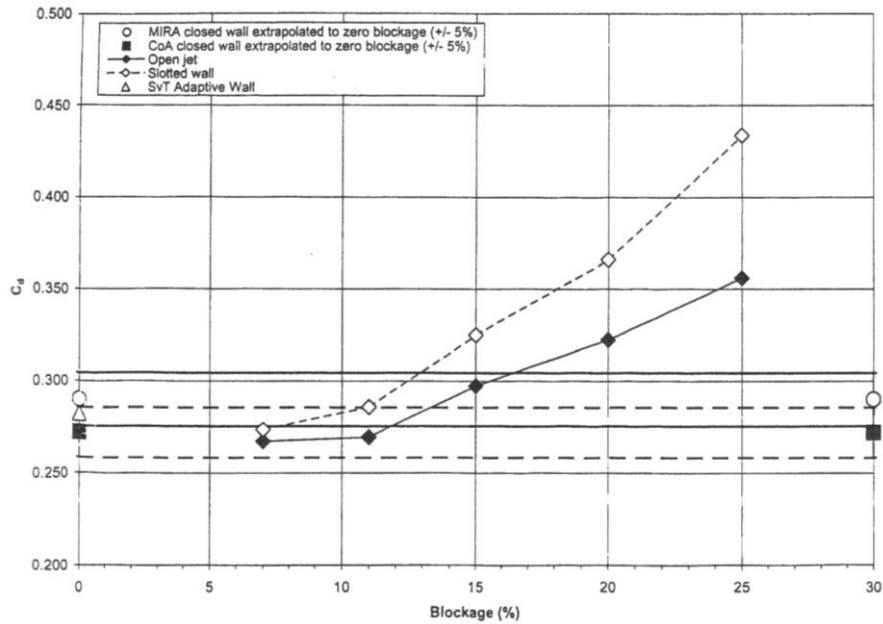
Figure 2.7 C_D as a Function of Model Blockage for MIRA Notchback Model [7]

Consequently, the open jet test section was better than the slotted wall test section at the higher blockage ratios.

Mercker E. [8] investigated the blockage correction effects on passenger cars. The model was tested in a closed test section of a wind tunnel. In that study, full scale MIRA Notchback model was experimented in German-Dutch Wind Tunnel. Three different closed test sections were used. 0.280 (8x6 m^2) and 0.278 (6x6 m^2) drag coefficient values were obtained for full scale MIRA Notchback model.

Gümüşlüol [9] tested 1/4 scale Ahmed Body with the 0° slant angle at a Reynolds number of 3.3x10^5 and 1/18 scale MIRA Notchback model at a Reynolds number of 2.9x10^5. In this study, aerodynamic interactions of two different types of road vehicles were investigated while they were in close-following and passing situations. Drag forces and surface pressures of the reference models at each case were measured. Two different blockage correction methods were applied and the results were discussed. According to these results, the drag coefficient of Ahmed Body was

10

measured as 0.296 with an uncertainty value of 0.013. For the MIRA Notchback model, it was measured 0.329 with an uncertainty value of 0.015.

Örselli [10] performed CFD analyses of 1/4 scale Ahmed Body with the 0° slant angle at a Reynolds number of 3.3×10^5 and 1/18 scale MIRA Notchback model at a Reynolds number of 2.9×10^5. Aerodynamic interactions of two different types of road vehicles were investigated while they were in close-following and passing situations. Drag forces and surface pressures of the reference models at each case were analyzed. As a result of CFD analyses, the mean drag coefficient of Ahmed Body was obtained 0.322 and for the MIRA Notchback model, it was obtained 0.325.

CHAPTER 3

THEORETICAL CONSIDERATIONS

3.1 Understanding Air Flows

There are no ready methods to understand and predict how air will flow around a given vehicle shape because the flow around a road vehicle is three-dimensional, the air does not follow the contours of the body and there is an unsteady wake behind the vehicle shape.

3.1.1 Aerodynamic Drag

The drag force is the most important aerodynamic element for the design of road vehicles. The aerodynamic drag is more effective at speeds above about 65-80 km/h. It can be gained advantages in terms of the economy and the performances by reducing drag.

3.1.2 Drag Coefficient

A dimensionless quality, which is called the drag coefficient (C_D) is utilized to measure the resistance of an object in a fluid medium. The drag coefficient mostly depends on the shape of the object. The drag aerodynamic is dependent on the frontal

area of the object, the air density and the square of the air velocity. This relation can be formulized by

$$Drag = \frac{1}{2}\rho V^2 A C_D \qquad\qquad (3.1)$$
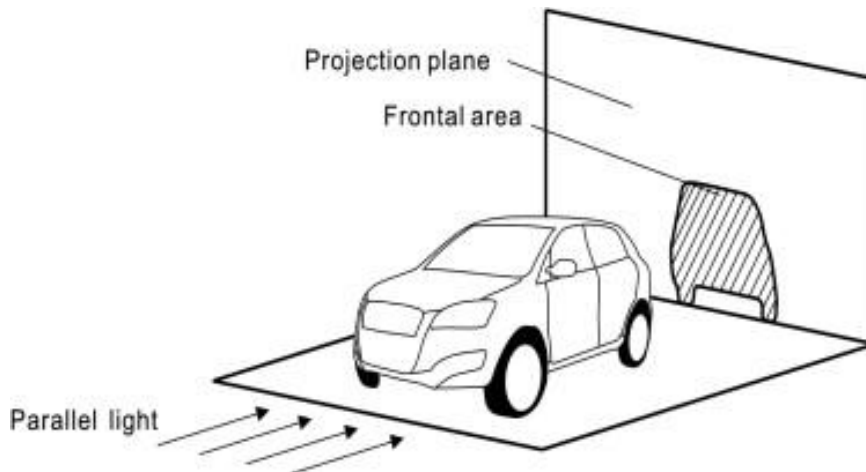
Figure 3.1 Projected Frontal Area [11]

The frontal area can be illustrated with Figure 3.1. The projected frontal area is about 80% of the product of entire height and width. The drag coefficient is not only dependent on the shape of the object but also depends on turbulence level of the flow and Reynolds Number.

3.1.3 Contributions to Aerodynamic Drag

The pressure distributions around the object and the shearing action of the flow on the surface produce the aerodynamic drag force. The shear and pressure forces can be shown by Figure 3.2.
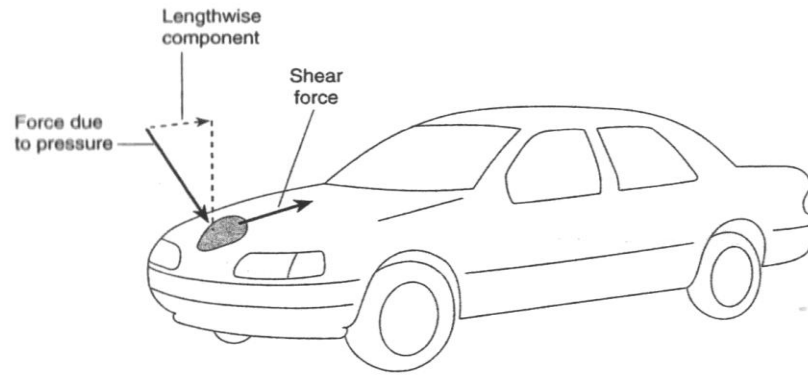
Figure 3.2 Shear and Pressure Forces on a Vehicle [12]

3.1.4 Surface Friction Drag

Surface friction drag occurs from the interplay between the fluid and the surface of the vehicle. The local skin (wall) friction coefficient can be formulized by

$$C_f = \frac{\tau_w}{\frac{1}{2}\rho V^2} \tag{3.2}$$

This type of a drag force is based on the rate where the layer of air which is right next to the surface is trying to slip relative to each other.

3.1.5 Pressure Drag

The shape of the vehicle also produces a drag which is called a pressure drag or a form drag. The main element in the pressure drag is the general size and shape of the vehicle. The boundary layer which is the most important interacting influences produces the pressure distribution around a body. In order to evaluate influences of

the boundary on the pressure distribution, it is considered two dimensional flow around a smooth symmetrical shape. This case is shown in Figure 3.3.
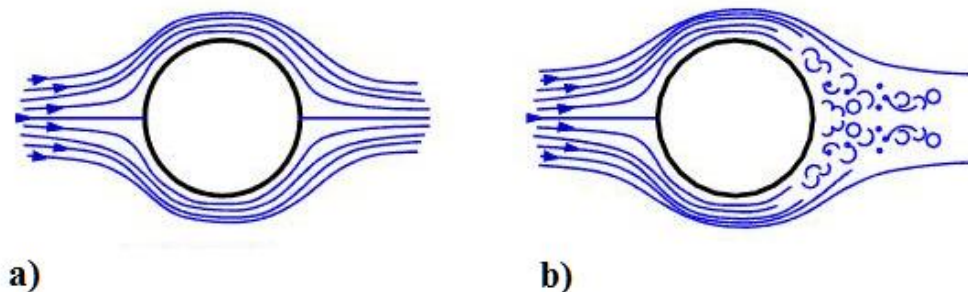
Figure 3.3 The Effects of Viscosity a) Ideal Flow, b) Real Flow [13]

When the air comes to nose, the relative air velocity becomes zero. Then the flow speeds up at the surroundings of the broadest part, the flow reaches a high relative velocity and then decelerates since the flow closes the tail. If there is not the effect of viscosity and pointed corners, the streamline would follow smoothly the shape of the contour as demonstrated in Figure 3.3(a). There would be a symmetric pattern and symmetric pressure distribution. Hence, there would occur equal and opposite forces on corresponding forward and rearward facing parts of the surface so there would not be drag. However in a real flow, due to the existence of viscosity, the streamlines around the shape would appear as indicated in Figure 3.3(b). The pattern of streamline and the distribution of pressure are asymmetrical in reality. There will be a net rearward drag force because the pressure on the rear part of the shape is to mean lower than on the front. The boundary layer normal pressure drag which is also known as the form drag makes contribution to the overall drag comprising of in this way. While the separation of flow occurs, the quantity of pressure drag generated is dependent plenty in the region where flow separates.

16

3.1.6 Pressure Coefficient

The pressure coefficient is indicated by C_p and the ratio is:

$$C_p = \frac{p - p_\infty}{\frac{1}{2}\rho V_\infty^2} \tag{3.3}$$

From this equation it can be seen that the difference between the local static pressure in a flow and the static pressure in the free stream relate to the dynamic pressure of the free stream. Since the pressure coefficient will not change with the vehicle velocity, the pressure coefficient is preferred rather than the actual pressure while describing how the pressure alters around a vehicle.

3.2 Modeling, Similarity, and Dimensional Analysis

Analytical methods cannot always be used since simplification of analysis is limited and a detailed analysis can be complex. In these cases, an experimental test may be used as a common alternative method. However, if the experimental test is not planned and organized, the procedure can be time consuming, expensive or lack direction. These results may occur especially while the experimental procedure requires testing at one set of conditions, geometry, and fluid with the objective to represent a different but similar set of conditions, geometry, and fluid. The time consuming and expensive experimental procedures can be reduced by the dimensional analysis. The dimensional analysis makes the final results normalized for a variety of conditions. Even the different fluid is used, for one test case can predict the performance at dissimilar conditions by a non-dimensional group of results. However, the conditions are similar dynamically. In order to make the

17

dimensional analysis, dependent and independent variables are compiled for the problem and suitable procedure is used to define non-dimensional parameters.

3.2.1 Buckingham Pi Theorem

Buckingham Pi Theorem is a procedure which is used commonly to describe the number and the form of resulting non-dimensional parameters. According to the Buckingham Pi Theorem, the dimensional analysis of the flow on a road vehicle can be summarized as follows:

The parameters which affect the road vehicle drag can be written as:

$$D = f(L, V, \rho, \mu, \varepsilon, \alpha) \tag{3.4}$$

where

L: the length of the vehicle (m)

V: the velocity of the vehicle (m/s)

ρ: density of air (kg/m^3)

μ: the absolute viscosity of air $\left(\frac{N.s}{m^2}\right)$

ε: the equivalent roughness height (m)

α: the yaw angle

The yaw angle can be eliminated because the yaw angle is non- dimensional. Then, primary dimensions of all parameters are written as

$$D = f(L, V, \rho, \mu, \varepsilon, \alpha) \tag{3.5}$$

There are 6 variables (n=6)

D	L	V	ρ	μ	ε
$\{MLT^{-2}\}$	$\{L\}$	$\{LT^{-1}\}$	$\{ML^{-3}\}$	$\{ML^{-1}T^{-1}\}$	$\{L\}$

The number of basic dimensions is $j = 3(M, L, T)$

Repeating parameters are selected as ρ, V, L. Then, $k = n - j = 6 - 3 = 3$ independent pi parameters will be obtained.

$$\Pi_1 = f(\Pi_2, \Pi_3) \tag{3.6}$$

The first parameter Π_1 is got as

$$\Pi_1 = \rho^a V^b L^c D = \left[\left(\frac{M}{L^3}\right)^a \left(\frac{L}{T}\right)^b (L)^c \left(\frac{ML}{T^2}\right) \right] = [M^0 L^0 T^0] \tag{3.7}$$

Concluding the powers for each dimensions

Mass: $a + 1 = 0 \rightarrow a = -1$

Time: $-b - 2 = 0 \rightarrow b = -2$

Length: $-3a + b + c + 1 = 0 \rightarrow c = -2$

19

$$\Pi_1 = \frac{D}{\rho V^2 L^2} \tag{3.8}$$

In place of L^2, the projected frontal area of the vehicle, A can be written for equation (x), and divided 1/2

$$\Pi_1 = \frac{D}{\frac{1}{2}\rho V^2 A} = C_D = Drag\ Coefficient \tag{3.9}$$

Repeating the process with other non- dimensional parameters;

$$\Pi_2 = \rho^d V^e L^f \mu = \left[\left(\frac{M}{L^3}\right)^d \left(\frac{L}{T}\right)^e (L)^f \left(\frac{M}{LT}\right) \right]$$
$$= [M^0 L^0 T^0] \tag{3.10}$$

Solving:

Mass: $d + 1 = 0 \rightarrow d = -1$

Time: $-e - 1 = 0 \rightarrow b = -1$

Length: $-3d + e + f - 1 = 0 \rightarrow f = -1$

$$\Pi_2 = \frac{\mu}{\rho V L} \tag{3.11}$$

$$\Pi_3 = \rho^x V^y L^z \varepsilon = \left[\left(\frac{M}{L^3}\right)^x \left(\frac{L}{T}\right)^y (L)^z (L) \right] = [M^0 L^0 T^0] \tag{3.12}$$

Solving:

Mass: $x = 0$

Time: $y = 0$

Length: $-3x + y + z + 1 = 0 \rightarrow z = -1$

$$\Pi_3 = \frac{\varepsilon}{L} \tag{3.13}$$

The dimensionless equation is

$$\frac{D}{\frac{1}{2}\rho V^2 A} = f\left(\frac{\rho V L}{\mu}, \frac{\varepsilon}{L}, \alpha\right) \tag{3.14}$$

or

$$C_D = f\left(Re, \frac{\varepsilon}{L}, \alpha\right) \tag{3.15}$$

where

C_D: the Drag Coefficient

Re: the Reynolds Number

$\frac{\varepsilon}{L}$: the Relative Surface Roughness

α: the Yaw Angle

On real condition, surface roughness is dependent on materiel, surface, corrosion and deposits. Hence, surface roughness is different from one vehicle to another. In order to estimate the drag forces, the equivalent surface roughness height should be defined [14]. It is supposed that the equivalent roughness height does not depend on Reynolds number. While the model is small, the surface smoothness is worse so the skin friction is affected by surface smoothness. Consequently, the second important factor for road vehicle aerodynamics is the surface roughness.

The yaw angle is the inclination angle of free-stream direction to the body longitudinal axis. Road vehicles are not run at zero yaw angles. Yaw angle is the element of aerodynamic and along the way of travel. Thus, road vehicles generally are exposed the yaw angles. The yaw angle is relevant to drag because the yaw angle resists vehicle to vehicle movement.

3.2.2 Similarity

Generally, the full size prototype testing by an experimental way is impossible or too expensive. One of the solution to deal with this problem is model testing instead of prototype testing. In this procedure the important parameter is to accomplish similarity between the prototype and its test conditions, and the experimental model and its test conditions in the experiments. Similarity for the model and the prototype can be defined as all relevant non-dimensional parameters have the same numerical values [15].

Similarity is categorized into three categories:

1. Geometric Similarity
2. Kinematic Similarity
3. Dynamic Similarity

Geometric Similarity

In fluid mechanics, geometric similarity means the equality of ratio of all corresponding dimensions in the model and prototype. This case requires all body dimensions must have indifferent linear-scale ratio in all three coordinates. In geometric similarity, all flow directions and angles must be conserved.

Kinematic Similarity

The first requirement is geometric similarity and the second requirement is kinematic similarity between the prototype and model. In fluid mechanics, kinematic similarity is stated as the motions of two systems are kinematically similar if homologous particles lie at homologous points at homologous times [16]. For kinematic similarity, the model and prototype must have the indifferent length-scale ratio and time-scale ratio. As a consequence the model and the prototype will have the same velocity-scale ratio. In addition, the flows will have similarly streamline patterns and flow regimes will be the same.

Dynamic Similarity

If the length-scale ratio, the time-scale ratio, and the force-scale ratio are the same for both the prototype and the model, the dynamic similarity is present. As mentioned before, the geometric similarity is the first requirement. Then the kinematic similarity and the dynamic similarity come into being at the same time, but the force and the pressure coefficient of prototype and model are the same. For a compressible flow, Reynolds number and Mach number of the prototype and model and specific-heat ratio are accordingly equivalent dynamic similarity is ensured.

3.3 Wall Interference in Closed Type Wind Tunnels

When tests are conducted in the wind tunnels in order to determine models aerodynamic characteristics, the results obtained may not be a characteristic example since the air jet of the tunnel is limited. The flow in the wind tunnel is affected by the boundary of the jet. This phenomenon is called wall interference.

The solid wind tunnel walls affect the expansion of the streamlines around the body and its wake. This effect is known as a blockage and is the result of velocity rising around the model and its wake. The blockage ratio which means the ratio of model

front area to test section area should not exceed 7.5%. The blockage is categorized into two categories: solid blockage and wake blockage. The solid blockage is the representative of the volume of blockage and the wake bubble formed next to it. In this region the flow velocity raises relatively accordingly the velocity of free stream and the pressure reduces accordingly the inlet pressure.
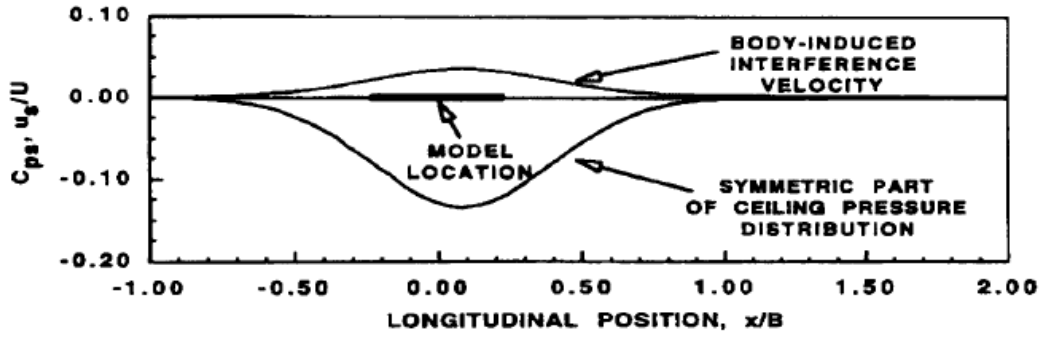
Figure 3.4 Plot for Velocity and Pressure Distributions in a Wind Tunnel Test Section due to the Effect of Solid Blockage [17]

The wake blockage is linked with the boundary caused the flow speed-up created because of the developing viscous wake. The wake blockage is in connection with wind axis drag. Figure 3.5 shows the influence of the wake blockage on the velocity variations and the pressure of the wind tunnel test section.
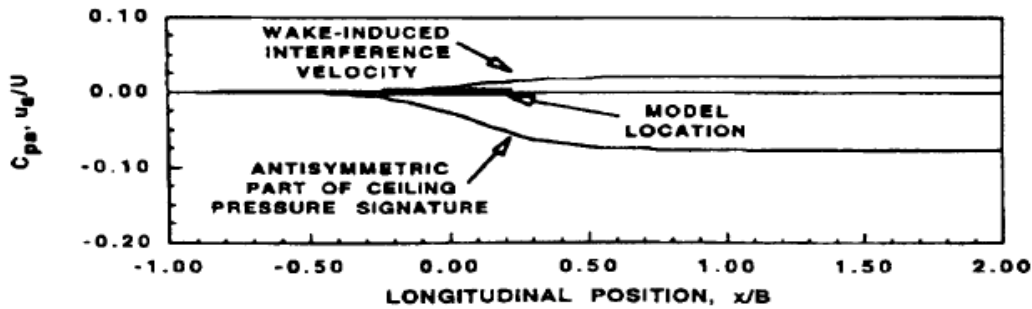
Figure 3.5 Plot for Velocity and Pressure Distributions in a Wind Tunnel Test Section due to the Effect of Wake Blockage [17]

24

In addition, Figure 3.6 demonstrates the joined solid and wake blockage effect components [17].
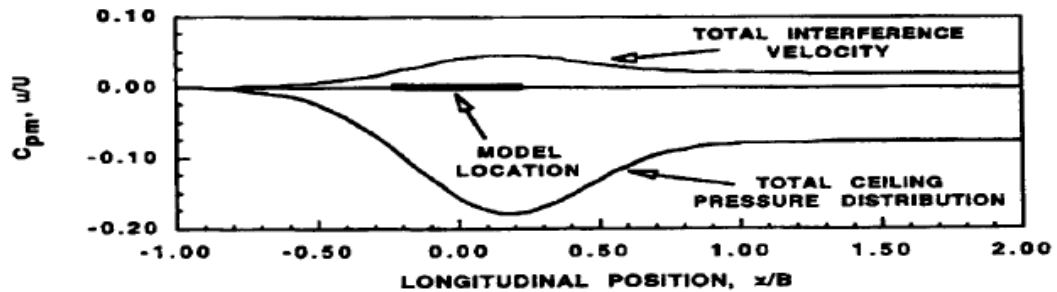
Figure 3.6 Plot for Velocity and Pressure Distributions in a Wind Tunnel Test Section due to the Combined Effect of Solid and Wake Blockage Components [17]

3.4 Blockage Correction Method

In the wind tunnel test section, because of the existence of the walls, the velocities around of the model are higher than if the walls were absent. If the velocities around the body increase, the obtained drag of the model increases. The methods of blockage correction are used to calculate the accurate drag coefficient. In the literature, there are several blockage methods. The continuity method, Maskell's Method, Mercker's Method, Hensel's Velocity Ratio Method and Pressure Signature Method are indicated as examples. Most of the correction methods are based on a mathematical approach assuming symmetry and represented by doublets [18]. In this study, Continuity Method was used as a blockage correction method.

3.4.1 Continuity Method

The continuity method is the simplest method of all. In this method it is assumed that the effective velocity of the airflow at the model is increased according to the cross-sectional areas of the model and the test section ratio.

$$\frac{V_c}{V} = \frac{C}{C - S} \tag{3.16}$$

Here, the corrected velocity is indicated by V_c and the measured value is shown with V. C is the cross sectional areas of the duplex test section and S is the model plus its mirror image. Then the ratio is

$$\frac{q_c}{q} = \left(\frac{V_c}{V}\right)^2 = \left(\frac{C}{C - S}\right)^2 = \left(1 - \frac{S}{C}\right)^{-2} \tag{3.17}$$

The correction for the drag coefficient is

$$C_{D_{corrected}} = \frac{C_D}{q_c/q} \tag{3.18}$$

3.5 Drag Measurement Through Wake Analysis

One of the contributions of occurring total drag is the wake behind the ground road vehicle. The wake is the consequence of the separated flow. The flow in the wake region is complicated, three- dimensional, and unsteady. If the ground road vehicles are improved in terms of a drag coefficient, wake structure is known thoroughly. By means of wake analysis the drag of different vehicle shapes can be measured [19].
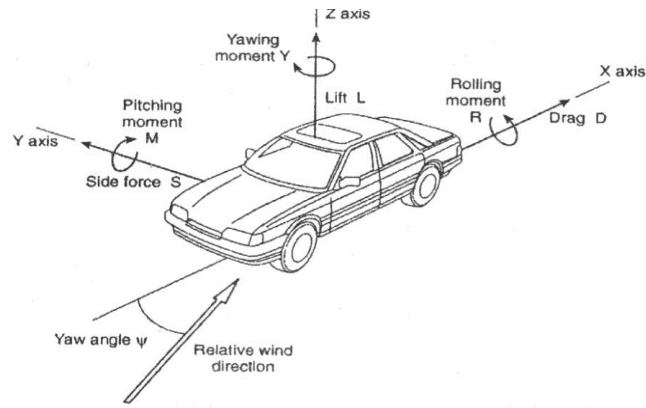
Figure 3.7 Definition of Coordinates [19]

In Figure 3.7, it is shown that a coordinate system is defined in automobile industry. In the x, y, and z- directions the velocity vector is described as following

$$\vec{u} = (U_\infty + u, v, w) \tag{3.19}$$

Then the drag can be calculated from below equation

$$D = \int_{S_3} (p_{0\infty} - p_{03}) dS + \frac{1}{2} \rho \int_{S_3} (v^2 + w^2 - u^2) dS \tag{3.20}$$

where

S_3: measured (y, z) - plane downstream of the model

$p_{0\infty}$: total pressure in the free stream

p_{03}: total pressure at each (y, z) – position in plane S_3

ρ: air density

u, v, w: velocity components

3.5.1 Boundary Layer Correction

Because of the boundary layer, there is a momentum loss in the measured wake. It is necessary to make a correction in order to evaluate obtained data accurately. For a laminar boundary layer, the momentum loss thickness is defined as

$$\theta = 0.664 L Re_L^{-1/2} \tag{3.21}$$

$$Re_L = \frac{\rho U_\infty L}{\mu} \tag{3.22}$$

However, there is no theoretical expression for a turbulent boundary layer. The momentum loss thickness for turbulent boundary layer can be calculated from an empirical expression [19]:

$$\theta = 0.036 L Re_L^{-1/5} \tag{3.23}$$

CHAPTER 4

EXPERIMENTAL SET-UP AND INSTRUMENTATIONS

An experimental plane was planned to examine the drag coefficient of different vehicles. A wind tunnel, the scale vehicle models and a set-up for drag force measurement are the main equipment and instrumentations. The design opinions and other components of the experimental devices are expressed in the following sections.

4.1 The Vehicle Models

In order to examine the influence of the form of a model for aerodynamic vehicle interactions of vehicles, two dissimilar ground vehicle models were used. First vehicle type model is the Ahmed Body with 0° rear slant angle. The scale is 1/4. The Ahmed Body model form looks like a bus. This model creates the main characteristic of flow uniformity around the center, separation of flow and the generation of wake at the rear of the vehicle. The main purpose of investigating the Ahmed Body car vehicle is to figure out how the flow processes affect drag generation. Figure 4.1 demonstrates Ahmed Body model and the characteristic dimensions of the Ahmed Body model is shown in Table 4.1.

Figure 4.1 The Ahmed Body Model

Table 4.1 Dimensions of the Ahmed Body

Dimensions (mm)	Prototype	Model
Vehicle length	1044	261
Vehicle width	389	97
Vehicle height	288	72

The other ground vehicle model is the MIRA Notchback model. The scale is 1/18. This kind of ground vehicle type model is preferred due to shape of vehicle. MIRA Notchback model is also similar to real cars. In Figure 4.2, MIRA Notchback model is demonstrated and the characteristic dimension of the MIRA Notchback model is shown in Table 4.2.

Figure 4.2 The MIRA Notchback Model

Table 4.2 Dimensions of the MIRA Notchback Model

Dimensions (mm)	Prototype	Model
Vehicle length	4133	229
Vehicle width	1612	89
Vehicle height	1206	67

The weight of Ahmed Body model is 890 grams and the 1/18 scale MIRA Notchback model is 367 grams. The material of models is wood. The models have high surface smoothness through vanishing.

4.2 Open Loop Low Speed Wind Tunnel

Experiments were carried out in an Open Loop Low Speed Wind Tunnel as shown in Figure 4. 3. The wind tunnel is operated through an axial flow fan. The motor drive turns the twelve bladed, axial flow fan that drives the flow. The motor drive can be

operated and the velocity adjustments can be made by means of the switches on the control panel.

The wind tunnel consists of diffuser, test section and contraction cone. The aim of contraction cone is to suck a large volume of low velocity air and decrease this large volume to a small volume of high velocity air. Models are located in the test section. Test section dimensions are 500x750x2400 mm. Plexiglass is used to visualize easily for 2 walls of the test section. The air follows the diffuser after test section. In this section, the air velocity decelerates because of the shape of the diffuser. This section is important because it saves money. The operating costs can be minimized by means of reducing power.

Figure 4.3 Open Loop Low Speed Wind Tunnel

4.3 Drag Force Measurement Set-up

The Set-up of a Drag Force Measurement is a structure and its parts are a balance, a power supply, and a Multimeter. Figure 4.4 shows a photograph from the test set-up of force measurement. As shown in Figure 4.5, the iron structure carries a balance. The vehicle models are held by balance. Figure 4.6 demonstrates that this balance

measures the steady drag force on the vehicle model. The dimensions of drag force measurement set-up are given in Appendix A.
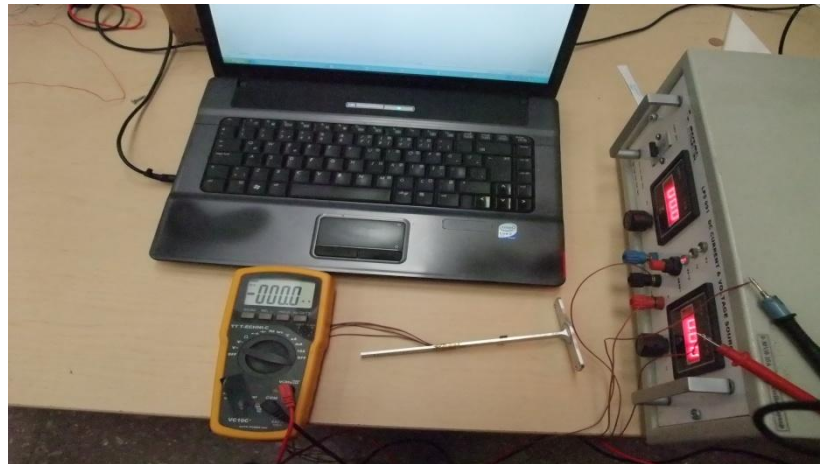
Figure 4.4 Drag Force Measurement Set-up

Figure 4.5 The Iron Structure of the Balance

Figure 4.6 MIRA Model Attached to the Test Set-up

In order to measure drag forces on small models, balance was designed. This set-up system is appropriate for operating in low speed wind tunnels. The schematic view belongs the balance is shown in Appendix A. There are four strain gages on the balance.

4.4 Air Flow Meter

The Fluke 922 Airflow Meter was used in order to measure pressure and air velocity. The Fluke 922 Airflow Meter is a versatile instrument that measures differential pressure and air velocity. The reasons of using The Fluke 922 Airflow Meter for measurement are its high accuracy and easy operation. The Fluke 922 Airflow Meter is appropriate with Pitot tubes. The Fluke 922 Airflow Meter measures differential and static pressure and air velocity. Obtained data can be displayed minimum, maximum and average values. By holding function, the data can be analyzed easily. There is also automatic frequency control.

Figure 4.7 The Fluke 922 Airflow Meter [20]

4.5 Laser Doppler Anemometry

Laser Doppler Anemometry (LDA) is a measuring technique. This technique measures the velocity by using Doppler shift in a laser beam. Laser Doppler Anemometry provides to follow the instantaneous velocity of the fluid. LDA is a substantial measurement instrument for fluid dynamic investigations. It is used widely where sensitivity is important. Tracer particles in the flow are the only requirement to use LDA. The velocity in reversing flow can be measured by means of LDA. Laser Doppler Anemometry consists of wave laser, transmitting optics, receiving optics, a signal conditioner and a signal processor. Beam splitter and a focusing lens are the part of transmitting optics. Receiving optics include a focusing lens an interference filter and a photodetector. The LDA working principle is shown in Figure 4.8.

Figure 4.8 Laser Doppler Anemometry Systems
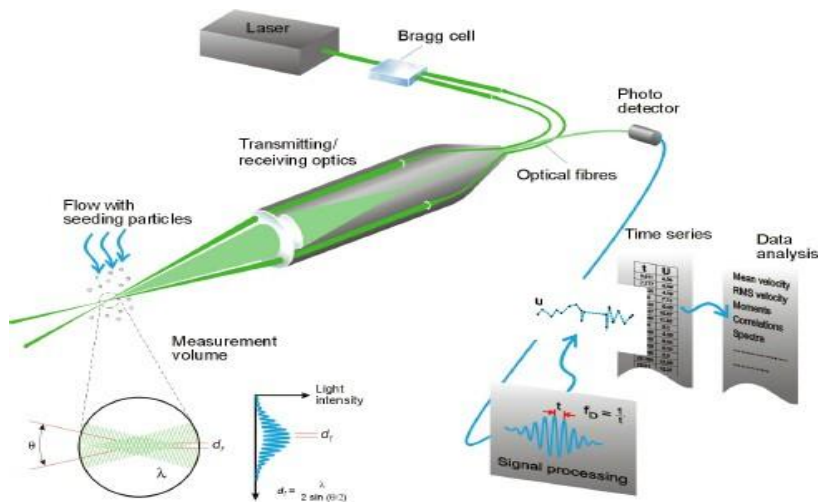
Figure 4.9 LDA working principle [21]

Laser Doppler Anemometry is an ideal measurement technique in wind tunnel investigations for testing aerodynamics of objects or structures and turbulence research.

4.6 Traverse Mechanism

The test section of the low speed wind tunnel was equipped with a traverse mechanism. The Traverse Mechanism was located at the end of the wind tunnel test section. As shown in the Figure 4.10, traverse mechanism can be moved in x, y, and z- coordinates. This traverse mechanism was constructed by Nejat Ulusal and Alişar Tuncer from Ulusal Control Systems Machinery Design Co. Traverse Mechanism was also used in Fluid Mechanics Laboratory of Mechanical Engineering Department for other Master Thesis study that was about Prediction of the Drag on Gimbal System via Balance Technique and Wake Integration Method. Pitot tube was mounted on this mechanism in order to measure the pressure and velocity. Traverse Mechanism is operated by touch screen on the control panel. Figure 4.11 shows the control panel of this mechanism. This mechanism can be operated in x, y, and z- coordinates automatically or manually by means of buttons on the touch screen. There are three sensors on the Traverse Mechanism. These sensors determine the location of the Pitot tube and can also warn the user at the critical location.
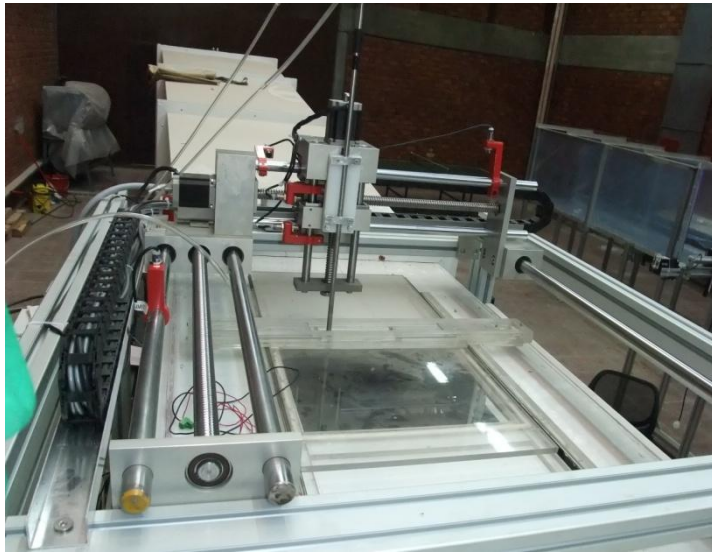
Figure 4.10 Traverse Mechanism
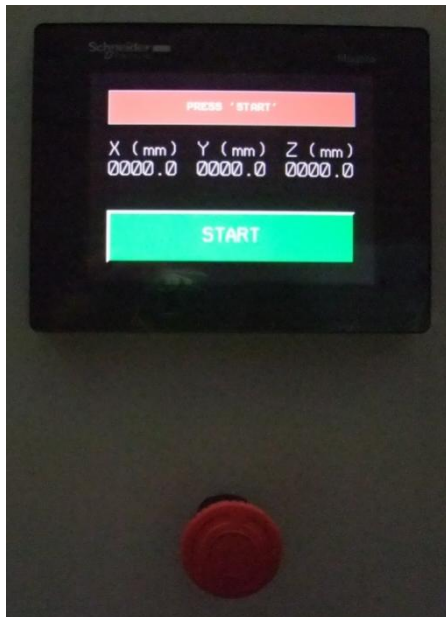
Figure 4.11 Control Panel of the Traverse Mechanism

4.7 Laser-Based Flow Visualizations

In fluid dynamics to get information about flow patterns, flow visualization is used. In experimental studies there are several methods in order to make flow patterns visible. In this study, particle tracer method was used. Particle tracer which was smoke was added to a flow in order to trace the fluid. Then, the particles were illuminated by a sheet of laser light. The instrumentations used to visualize flow are shown in Figure 4.12. The copper structure was used to distribute the flow homogeneously.

Figure 4.12 Smoke Generator and Copper Structure
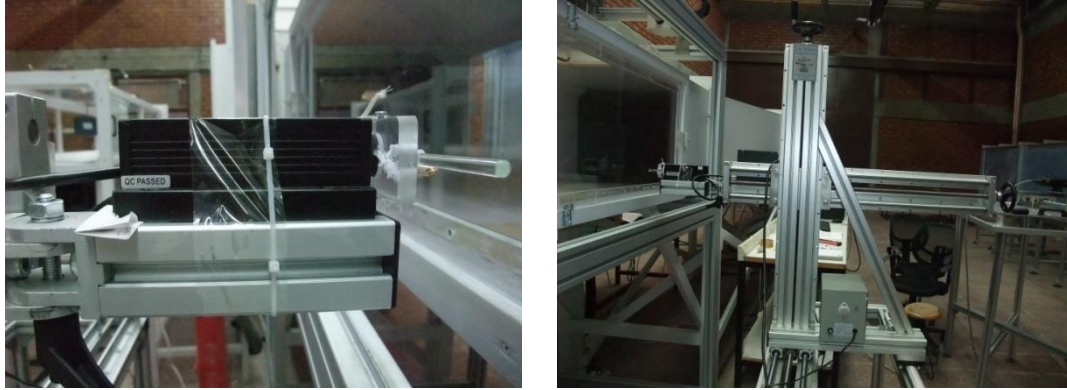
Figure 4.13 Laser System and its Traverse Mechanism

CHAPTER 5

EXPERIMENTAL PROCEDURE

Instruments have to be prepared and calibrated before the experiments are conducted. The calibration of balance, wind tunnel, and determinations of the turbulence level and velocity profile are described in this chapter. The experiment description is also explained in the following sections.

5.1 Calibration of the Balance System

In order to measure the drag of the car vehicles, the calibration was done before the experiments start. Dead weights were used which are known their weights to calibrate the balance system. The outputs of the strain gages were read through Multimeter. Then, the calibration curve was plotted.
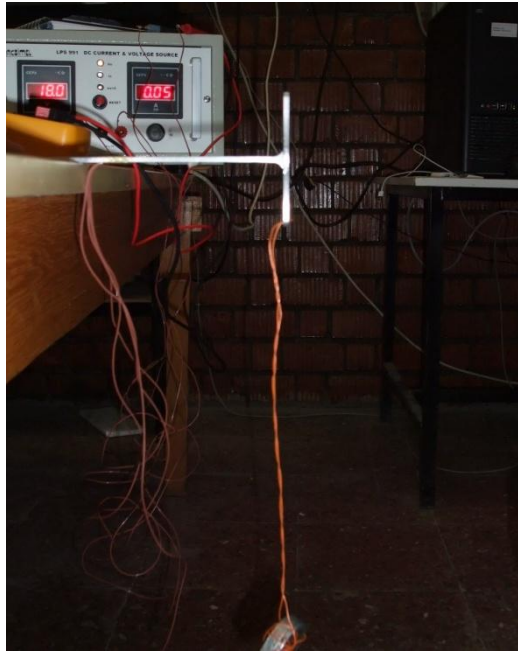
Figure 5.1 Image of How the Balance Calibrated

Table 5.1 The Results of Balance Calibration

Dead Weights (g)	Strain Gauges (mV)
0	-3.2
10	-2.8
20	-2.4
30	-2.0
40	-1.6
50	-1.2
100	0.6
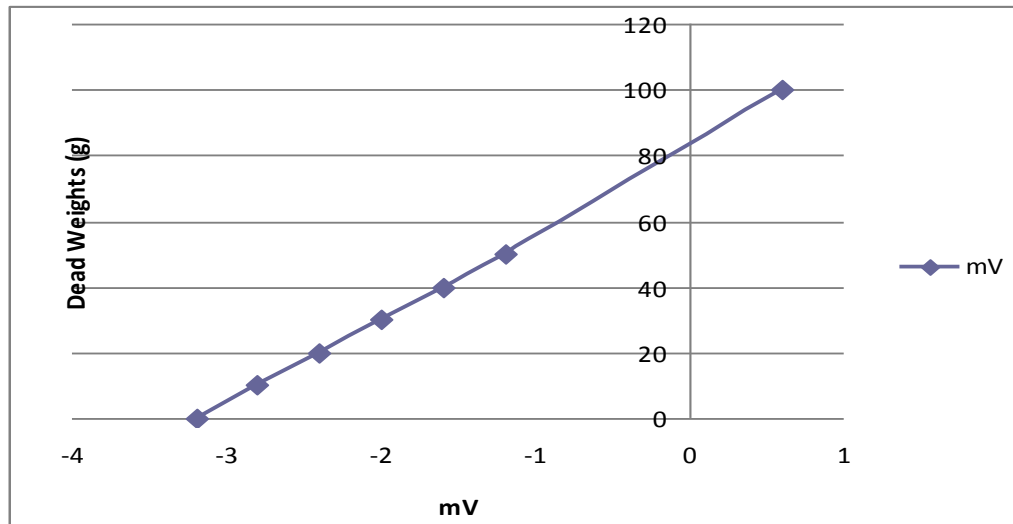
Figure 5.2 Balance Calibration

5.2 Determination of Free Stream Velocity

The temperature of a room was read from the digital thermometer before the each experiment was conducted. According to the room temperature, the air density was calculated. To measure the reference pressure, static and total pressure hole was drilled at the tunnel wall. The total and static pressure were measured from these holes by Pitot tube and manometer. Considering the air density corresponding to the room temperature value, the free stream velocity was calculated by using the dynamic pressure. In order to determine whether the obtained data were same or not for same condition, the procedure was repeated. Laser Doppler Anemometry was also used to measure the free stream velocity. Very close results were obtained for the same condition.

5.3 Determination of Flow Uniformity

The flow uniformity in the wind tunnel test section was determined through Pitot tube. There were measurement restrictions in x- and y- directions because of the traverse mechanism. In Figure 5.3, the coordinate system of wind tunnel test section is demonstrated. As understood from the measurement results, the free stream velocity of the wind tunnel is not constant at all points in the wind tunnel section. The reason of this case is the existence of the boundary layer of the test section ground plane.
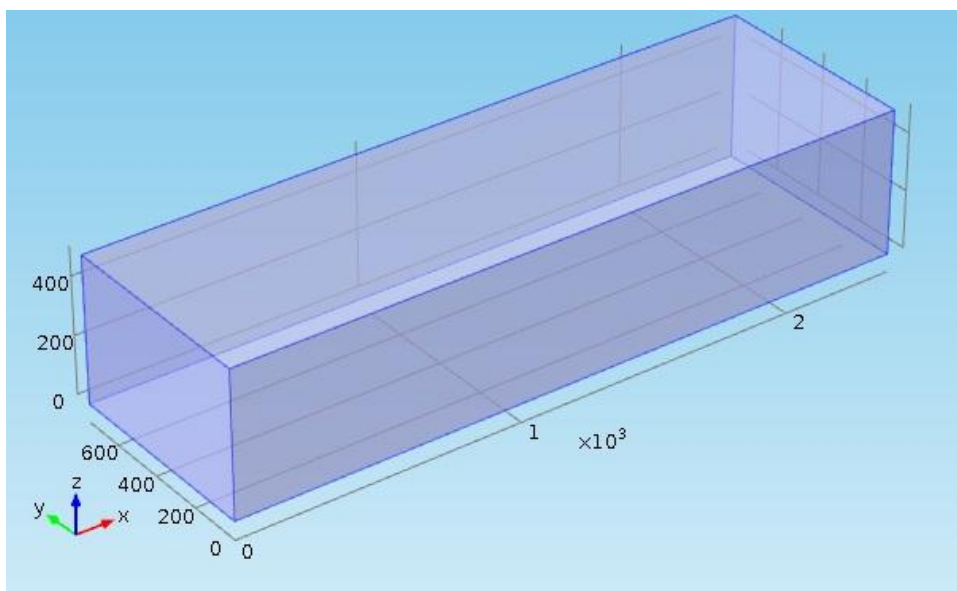
Figure 5.3 The Coordinate System of the Wind Tunnel Test Section
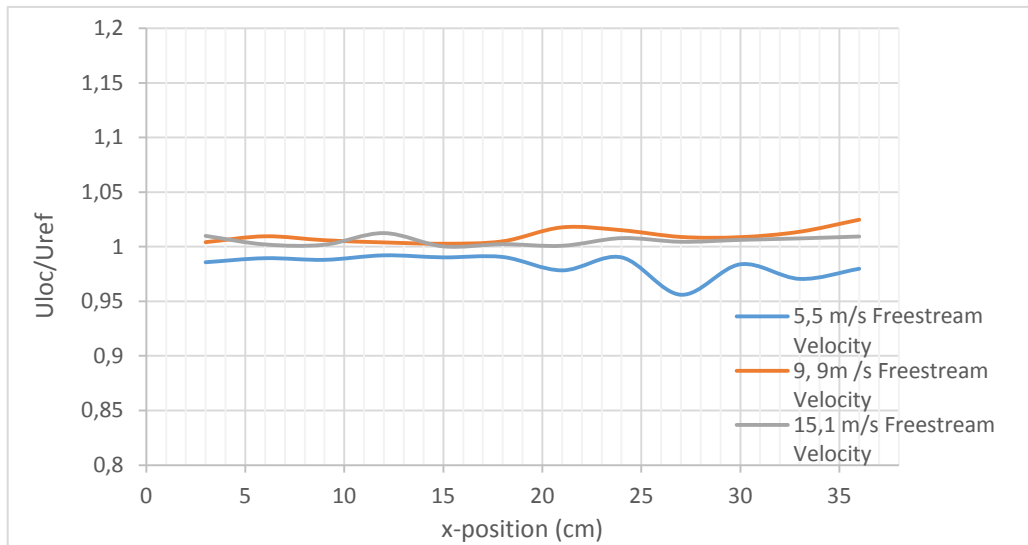
Figure 5.4 Flow Uniformity in the Test Section (x-direction)
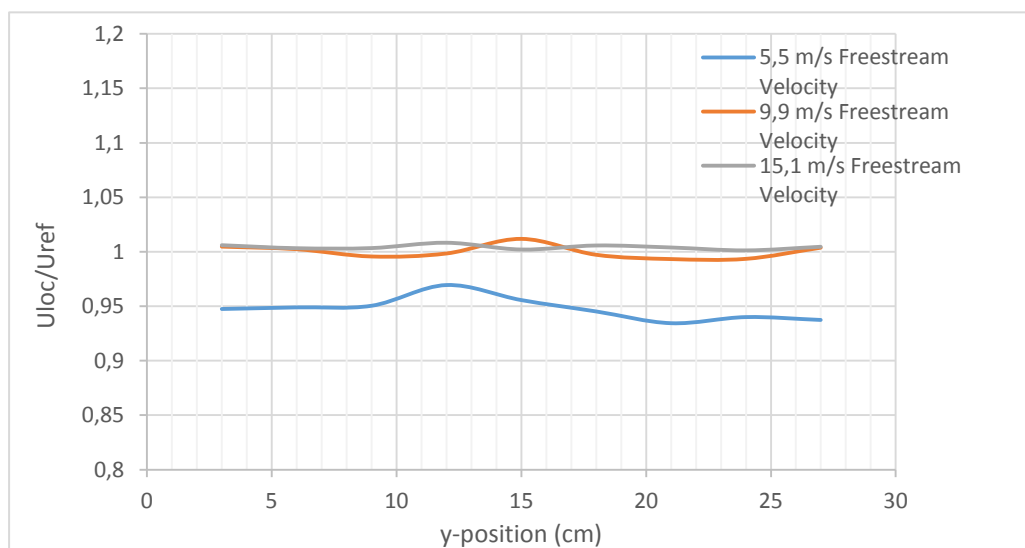
Figure 5.5 Flow Uniformity in the Test Section (y-direction)

45
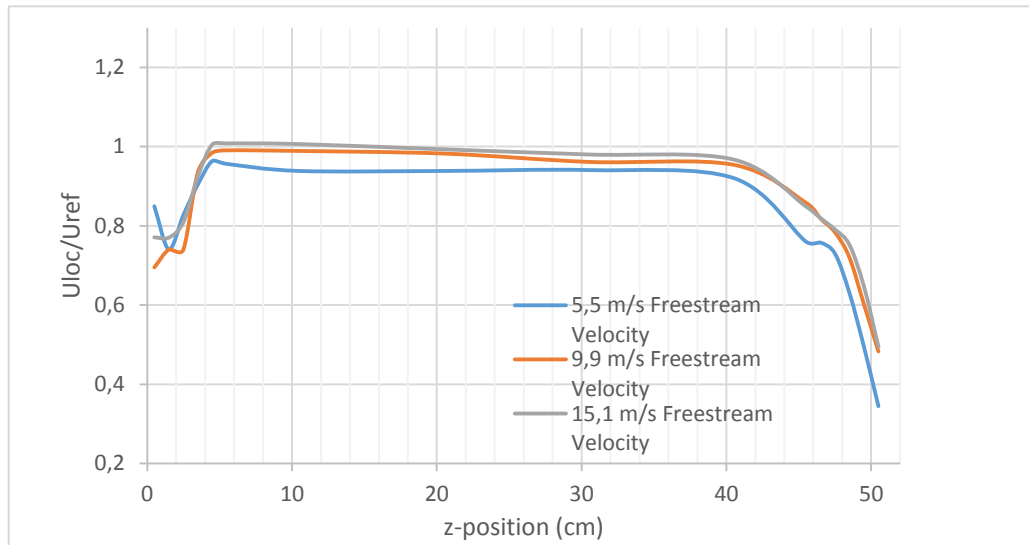
Figure 5.6 Flow Uniformity in the Test Section (z-direction)

5.4 Calibration of Laser Doppler Anemometry

Because the LDA can be calibrated by itself, calibration of LDA was not done before the experiments start.

5.5 Determination of the Turbulence Intensity

In order to comment accurately obtained results, level of the free stream turbulence should be measured. The turbulence intensity of the streamwise velocity fluctuations is symbolized with I_v and formalized with below ratio.

$$I_v = \frac{\sqrt{v^2}}{\bar{V}}$$ (5.5)

In this study, turbulence intensity was determined at the middle of the wind tunnel test section by means of Laser Doppler Anemometry. Table 5.2 demonstrates the turbulence intensity corresponding to the related velocity values.

Table 5.2 Turbulence Intensity of the Wind Tunnel Test Section

Freestream Velocity (m/s)	Turbulence Intensity
1.13	0.72
2.76	0.85
3.90	1.07
5.52	1.46
6.90	1.04
8.72	1.02
9.94	1.41
11.70	1.17
13.51	1.10
15.11	0.89
16.50	0.86
17.90	0.89
19.95	1.22
21.36	0.96
22.91	1.00
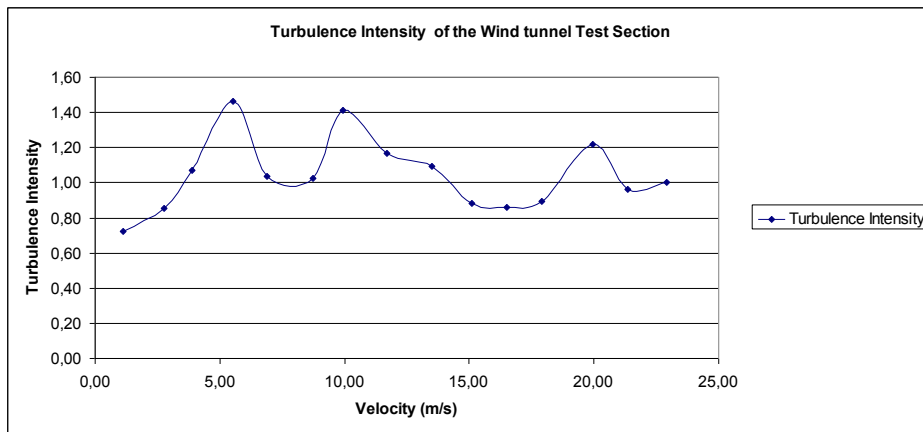
Figure 5.7 Turbulence Intensity of the Wind Tunnel Test Section

5.6 Description of the Experiments

In this study, drag and surface pressure measurements of two different vehicle models were investigated experimentally. Drag measurements were carried out via momentum integral equation and balance technique. At three different Reynolds number, the experiments were conducted for each model. Before the experiments were conducted, free stream velocities in the wind tunnel test section were determined through the Pitot tube and then the experiments were done via Laser Doppler Anemometry to control obtained free stream velocity data. According to obtained free stream data, three different velocities were determined to carry out the experiments easily. To measure the boundary layer thickness in the wind tunnel test section, measurements were done at different locations of the z-direction. Turbulence intensity in the wind tunnel test section was determined via Laser Doppler Anemometry for three different free stream velocity.

Figure 5.8 Ahmed Body Model Situation in the Test Section

Considering the dimensions of the wind tunnel test section and traverse mechanism, an appropriate location was determined for the traverse mechanism. Then, traverse mechanism was set on the wind tunnel test section. After the traverse mechanism was equipped on the wind tunnel test section, the model was located at ground of the wind tunnel test section carefully where the traverse mechanism could move easily around the vehicle model. For different free stream velocities, it was determined that whether the flow is laminar or turbulent. In accordance with model location, boundary layer displacement thickness was calculated for laminar and turbulent conditions.

In order to determine the wake of Ahmed Body and MIRA Notchback model, the plenty of data were acquired at several points of the x, y and z-directions for three different free stream velocities. According to obtained dynamic pressure, velocities were calculated and 3D graph plotted. Then, the equation of drawn graph was determined and drag was calculated via momentum integral method. The velocities of the wake of the Ahmed Body and MIRA Notchback model were also measured by means of Laser Doppler Anemometry. After drag measurements, blockage correction method was applied to obtain accurate drag. The surface pressure distribution of

models was surveyed for different Reynolds number. Lastly, by using smoke generator and laser, flow was visualized around the vehicle models.

CHAPTER 6

RESULTS AND DISCUSSIONS

The obtained of experimental data of the Ahmed Body and the MIRA Notchback model are presented in this chapter. For three different Reynolds number, drag force and surface pressure were measured and wake of reference models were investigated. The obtained results were discussed and compared with previous studies in the literature.

6.1 Balance Technique Results

In this part of results, firstly the drag coefficients of the Ahmed Body then, MIRA Notchback Model were calculated without applying the blockage correction method. These results of drag coefficients were called uncorrected drag coefficient as shown in Table 6.1 and Table 6.2.

Table 6.1 Uncorrected C_d Values of the Ahmed Body

Freestream Velocity (m/s)	Reynolds number (x10^5)	Uncorrected C_d
5.5	0.95	0,580
9.9	1.71	0,597
15.1	2.61	0,616

Although the blockage correction method was applied uncorrected drag coefficients values, because blockage ratios of investigating models do not exceed 7.5%, the drag coefficient values did not change saliently. As a result of these calculations, it was understood that the uncorrected drag coefficient values are higher than corrected values.

Drag Cofficient of Ahmed Body
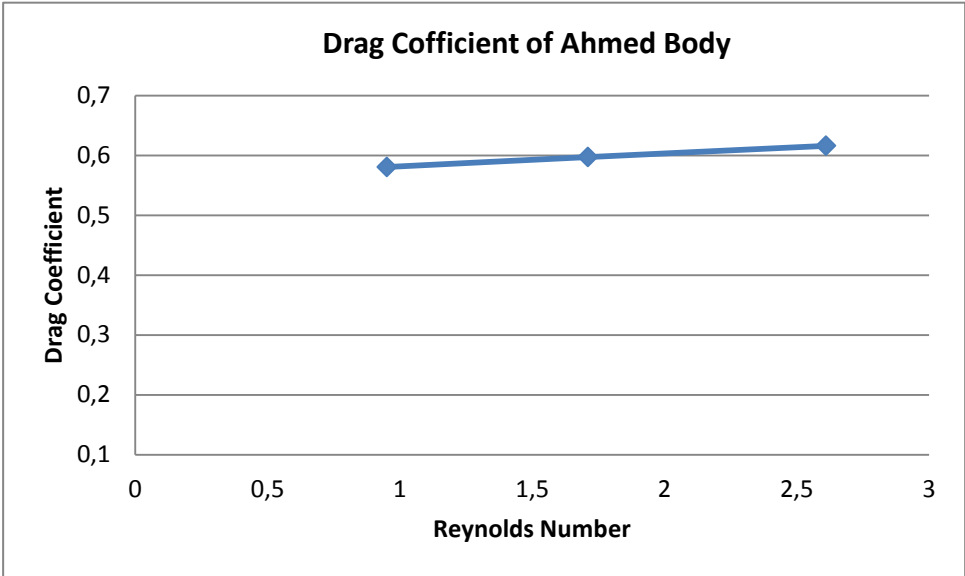
Figure 6.1 Corrected C_d Values of the Ahmed Body After Blockage Correction Method

The experimental measurements were conducted for three different Reynolds Number. According to these results as increasing Reynolds Number the drag coefficient is increasing within the investigated limits. The obtained drag coefficient values in this study are higher than previous works. In the previous works Gümüşlüol [9] determined the drag coefficient of 0^0 rear slant angle Ahmed Body as 0.296 at 3.3×10^5 Reynolds Number. In addition, under the same conditions, Örselli [10] analyzed the same body via CFD then, the drag coefficient of Ahmed Body was found 0.322 at 3.3×10^5 Reynolds Number.

Drag depends on the shape, size and inclination of the object, and on flow conditions of the air passing the object. However, there may be an additional component of drag which is called induced drag.

Attaching the balance system of the reference models may cause the lift force. Then, induced drag occurred. This occurred induced drag contributes the total drag coefficient. Because of this reasons the drag coefficient values may be obtained higher than previous work.

Table 6.2 Uncorrected C_d Values of the MIRA Notchback Model

| Freestream Velocity (m/s)	Reynolds number $(x10^5)$	Uncorrected C_d
5.5	0.83	0,283
9.9	1.53	0,279
15.1	2.29	0,270
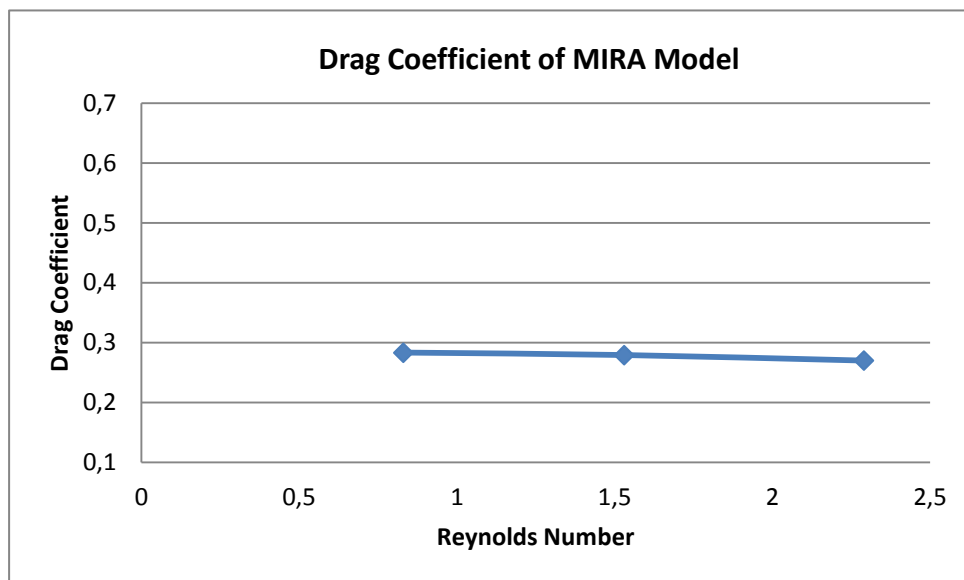
Figure 6.2 Corrected C_d Values of the MIRA Notchback Model After Blockage Correction Method

A similar procedure was applied to the MIRA Notchback model. Because this model has a less bluff shape than Ahmed Body, drag coefficient values are lower. It can be also seen that if the Reynolds number is increasing, the drag coefficient values are decreasing within the investigated limits.

In the previous works, Gümüşlüol [9] determined the drag coefficient of the MIRA Notchback model as 0.329 at $2.9\text{x}10^5$ Reynols number. Örselli [10] found the drag coefficient of the MIRA Notchback model as 0.325 at $2.9\text{x}10^5$ Reynols number via CFD. Comparing these results with previous studies, it is understood that the drag coefficient values were found lower.

6.2 Wake Analysis via Momentum Integral Method Results

Wind tunnel experiments are mainly conducted for measurements of drag coefficient of car models. Drag coefficient can be measured via several common techniques. One of them is balance technique. Via balance system the drag force can be measured however this method does not give any information about the structure of the wake. In addition the wake structure cannot be learned from the pressure distribution of models.

In this method, via static and total pressure probes the velocity was measured. The static and total pressure probe has been commonly used in wind tunnel experiments. The probe was traversed in the wake plane and different downstream positions in order to measure the whole wake.

The obtained results were demonstrated by means of below figures. Then, as mentioned in Chapter 3, surface equations from these 3D plotting were used in equation 3.20 and drag was obtained.
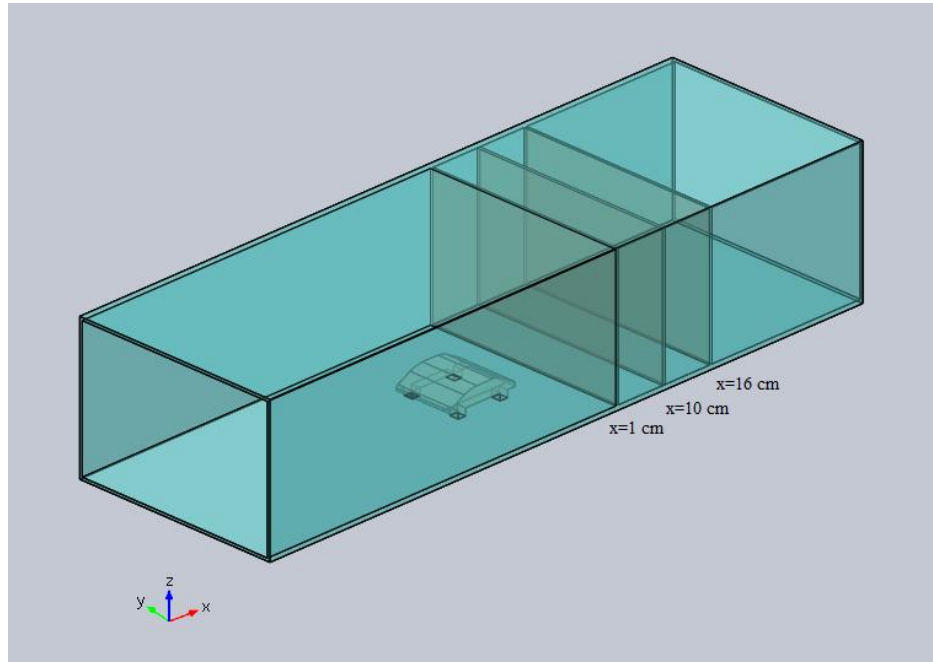
Figure 6.3 The Coordinate System of the Wind Tunnel Test Section
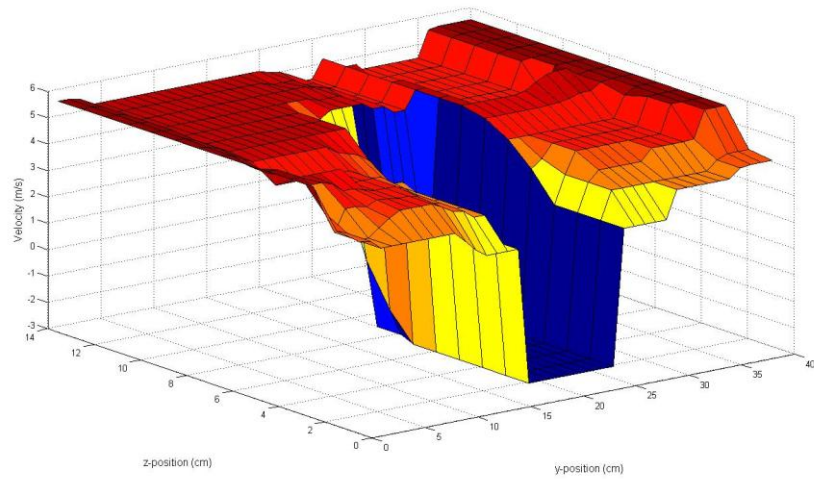
Figure 6.4 Wake Behind the Ahmed Body at Reynolds Number 0.95×10^5 (x=1cm)
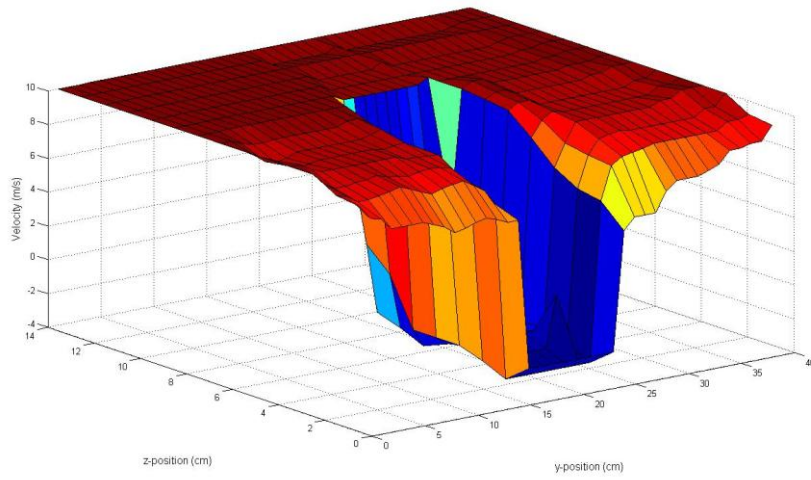
Figure 6.5 Wake Behind the Ahmed Body at Reynolds Number 1.71×10^5 (x=1cm)
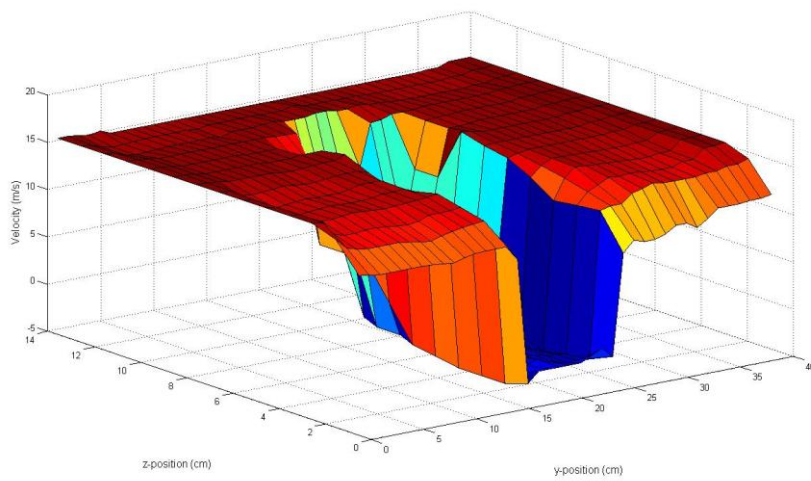
Figure 6.6 Wake Behind the Ahmed Body at Reynolds Number $2,61 \times 10^5$(x=1cm)
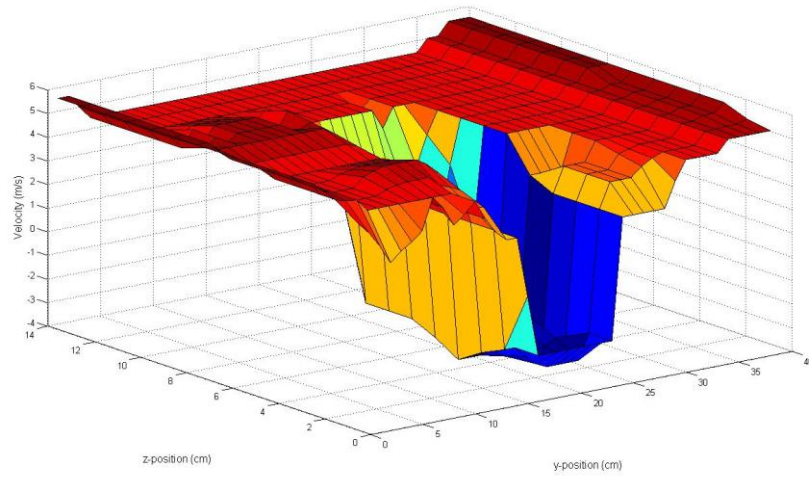
Figure 6.7 Wake Behind the Ahmed Body at Reynolds Number $0.95\text{x}10^5$ (x=3cm)
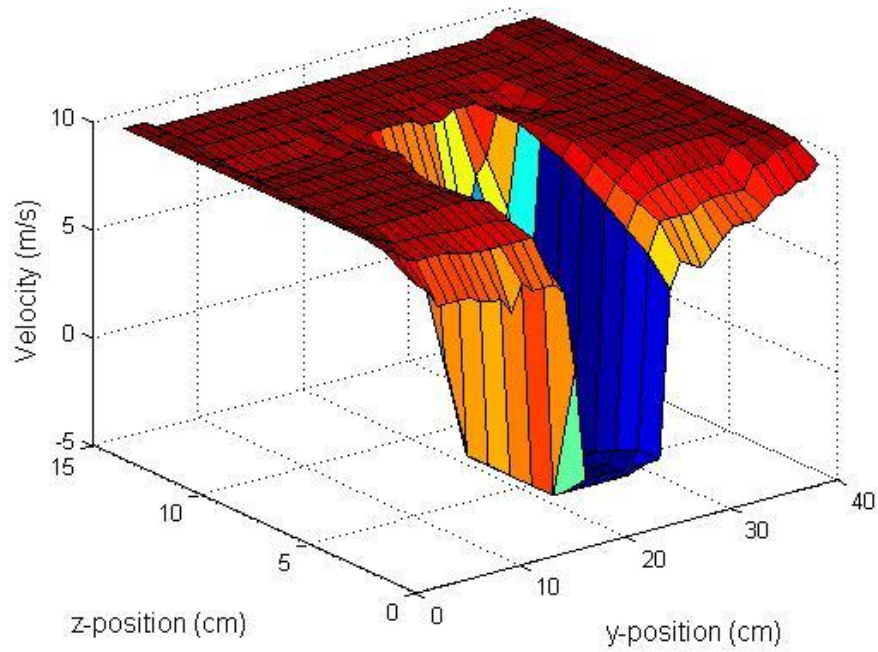
Figure 6.8 Wake Behind the Ahmed Body at Reynolds Number $1.71\text{x}10^5$ (x=3cm)
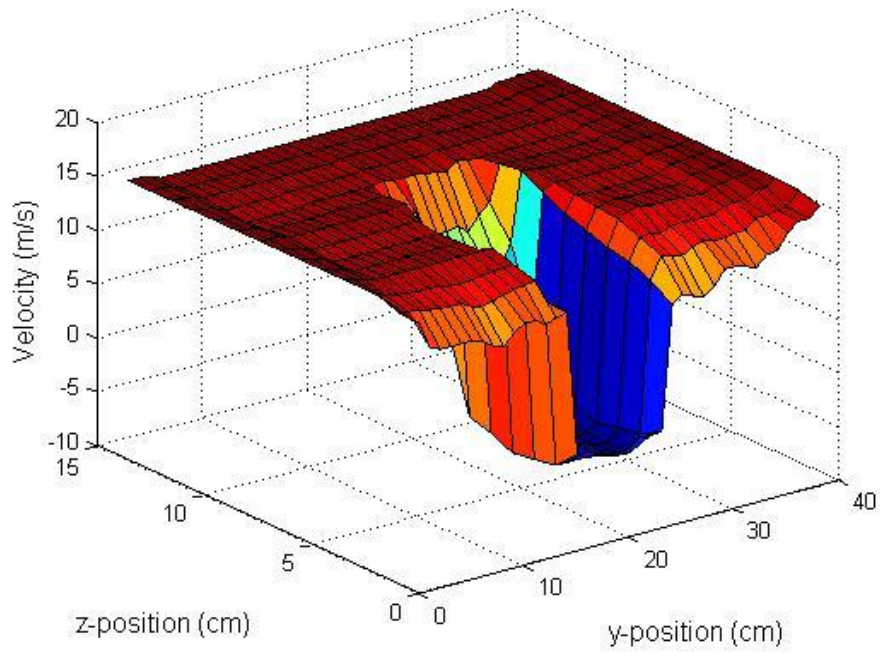
Figure 6.9 Wake Behind the Ahmed Body at Reynolds Number 2.61×10^5 (x=3cm)
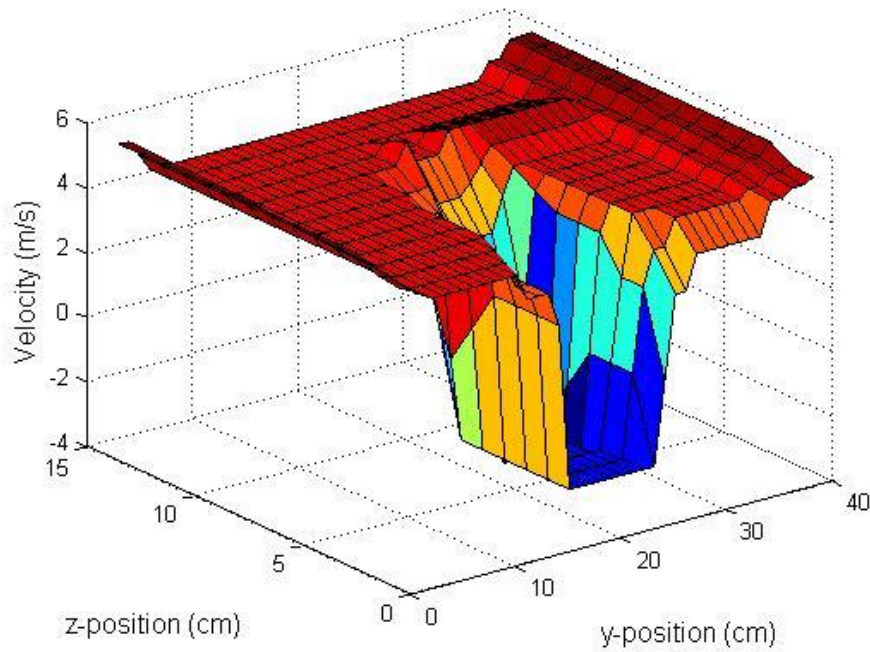
Figure 6.10 Wake Behind the Ahmed Body at Reynolds Number 0.95×10^5 (x=5cm)
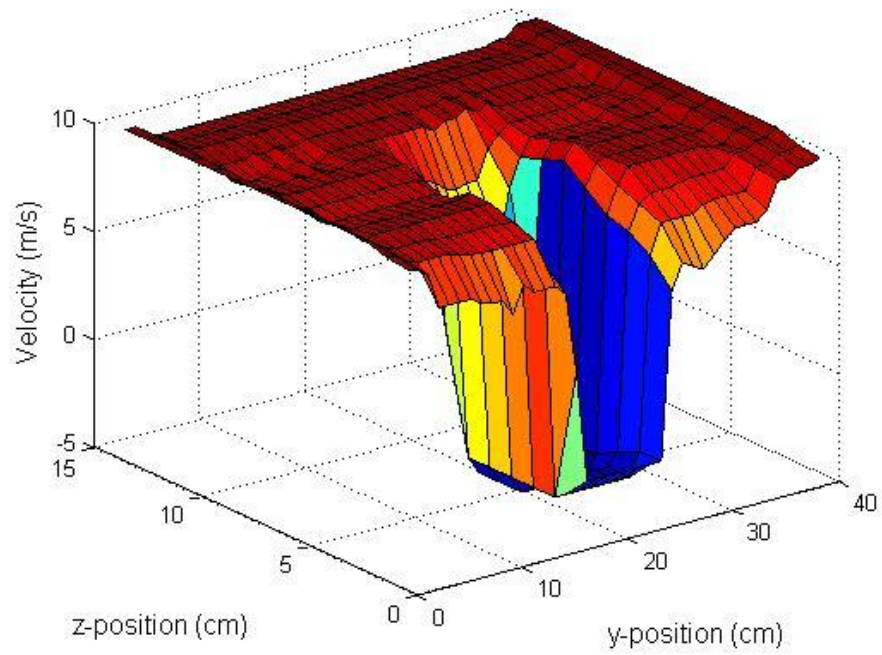
Figure 6.11 Wake Behind the Ahmed Body at Reynolds Number $1.71x10^5$ (x=5cm)
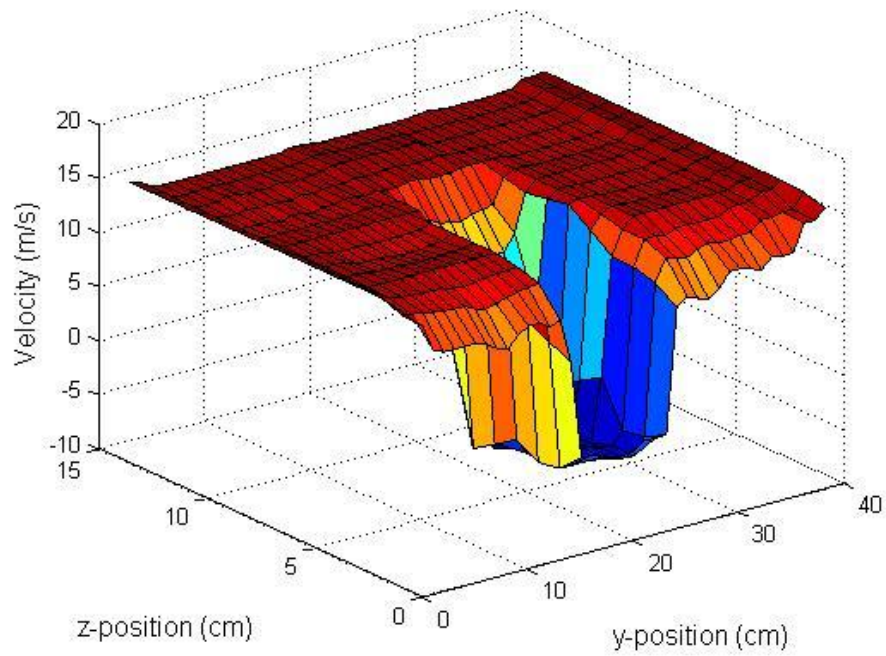
Figure 6.12 Wake Behind the Ahmed Body at Reynolds Number $2.61x10^5$ (x=5cm)
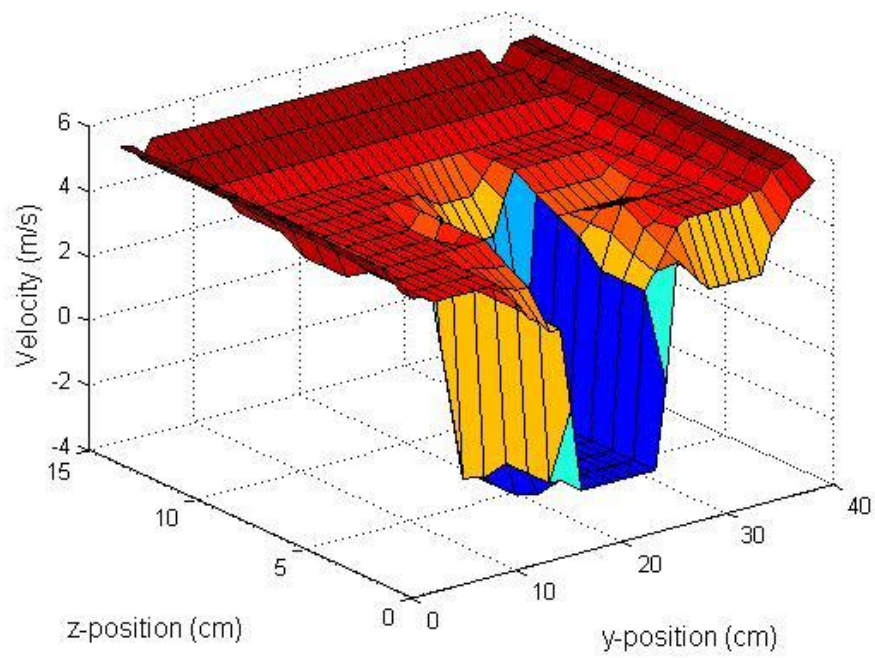
Figure 6.13 Wake Behind the Ahmed Body at Reynolds Number 0.95×10^5 (x=7cm)
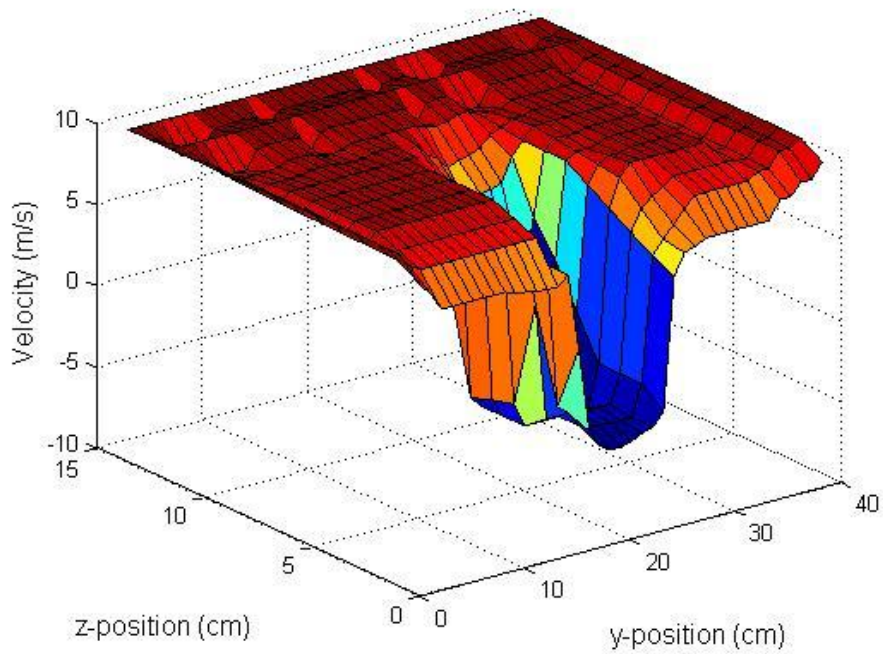
Figure 6.14 Wake Behind the Ahmed Body at Reynolds Number 1.71×10^5 (x=7cm)
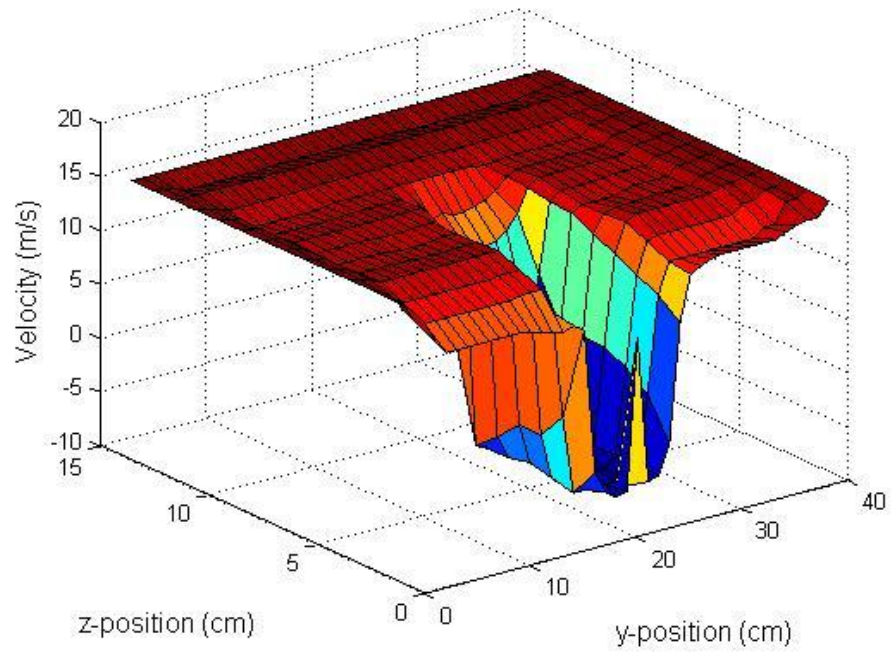
Figure 6.15 Wake Behind the Ahmed Body at Reynolds Number 2.61×10^5 (x=7cm)
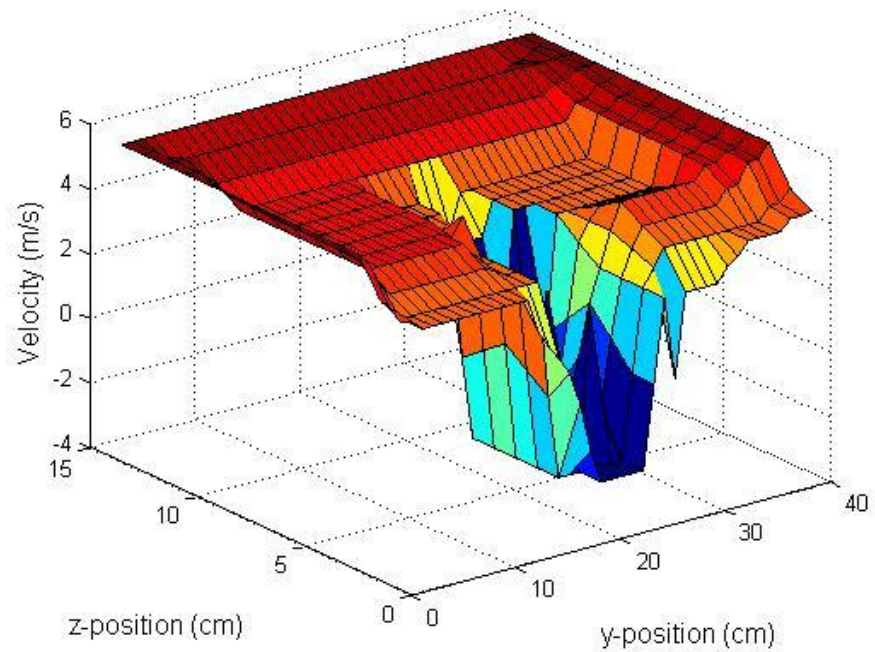
Figure 6.16 Wake Behind the Ahmed Body at Reynolds Number 0.95×10^5 (x=12cm)
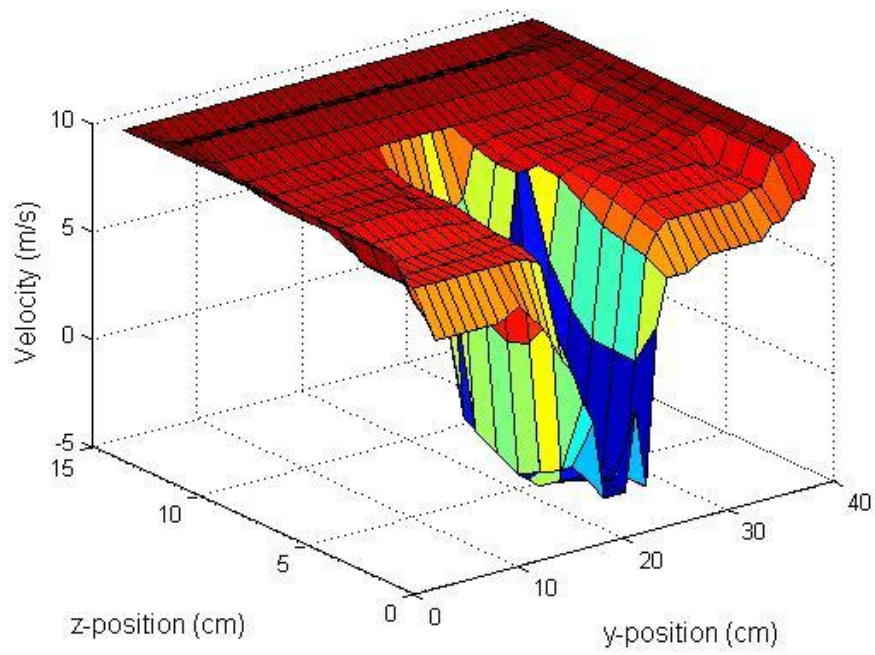
Figure 6.17 Wake Behind the Ahmed Body at Reynolds Number 1.71×10^5 (x=12cm)
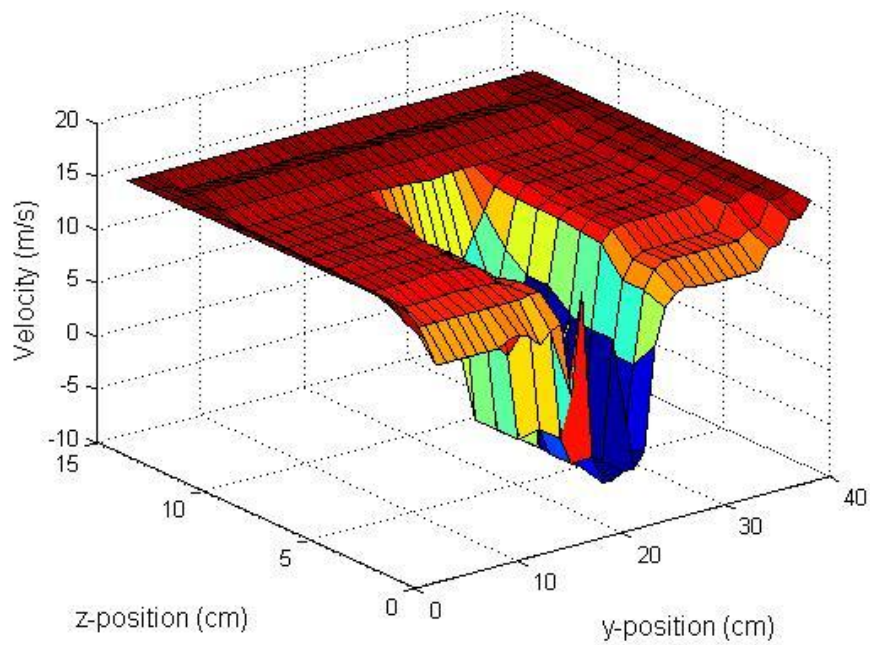
Figure 6.18 Wake Behind the Ahmed Body at Reynolds Number 2.61×10^5 (x=12cm)
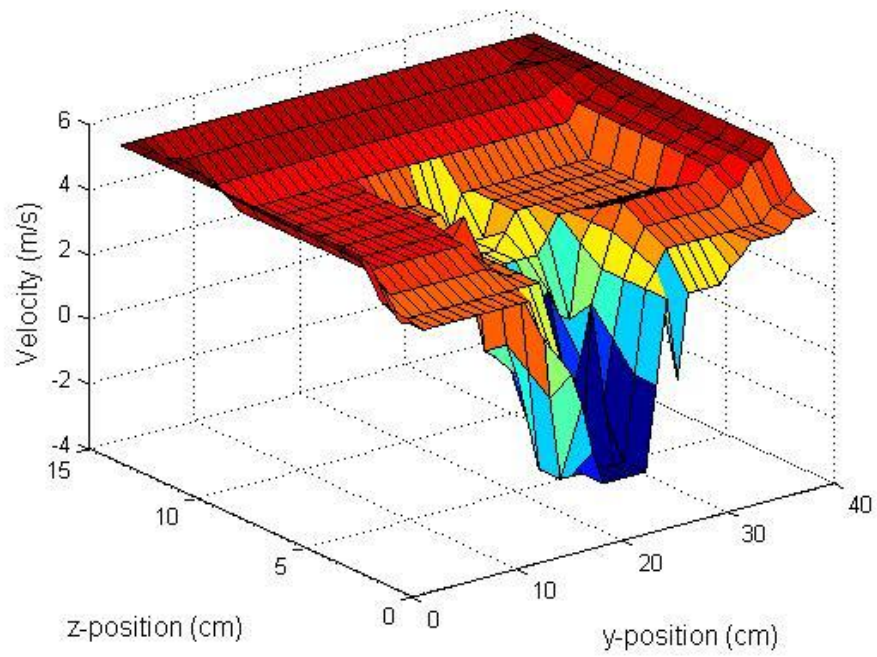
Figure 6.19 Wake Behind the Ahmed Body at Reynolds Number $0.95\text{x}10^5$ (x=14cm)
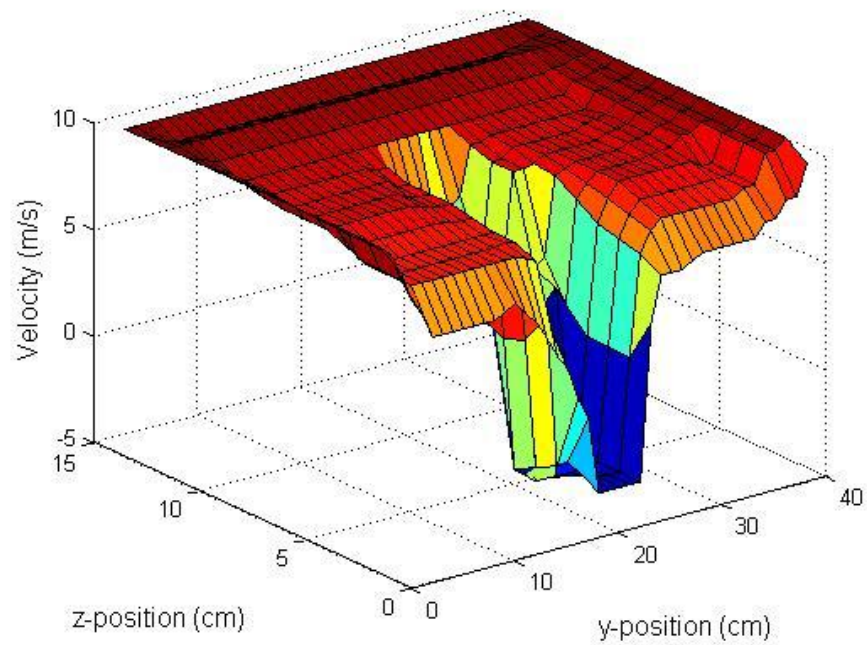

Figure 6.20 Wake Behind the Ahmed Body at Reynolds Number $1.71\text{x}10^5$ (x=14cm)
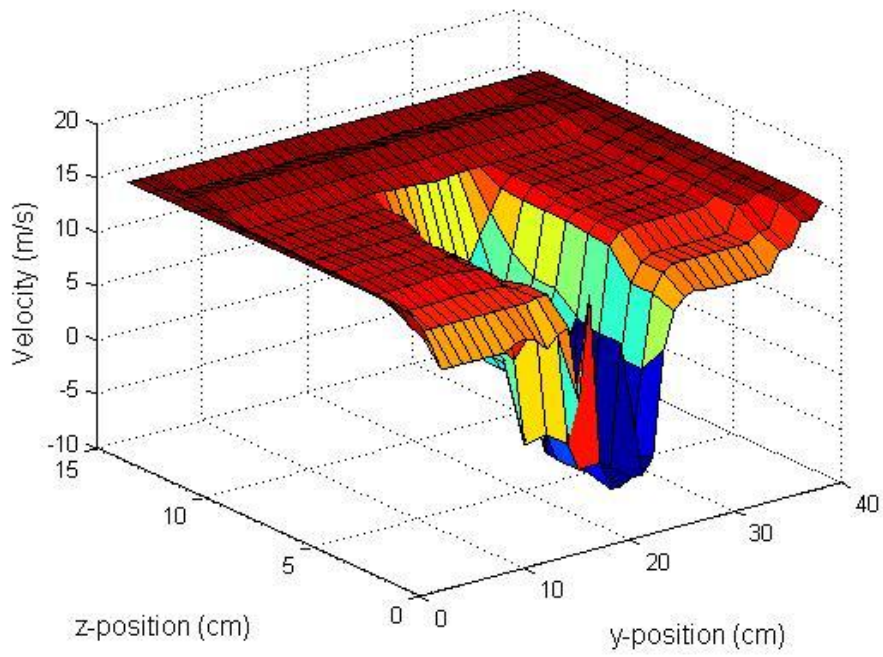
Figure 6.21 Wake Behind the Ahmed Body at Reynolds Number 2.61×10^5 (x=14cm)
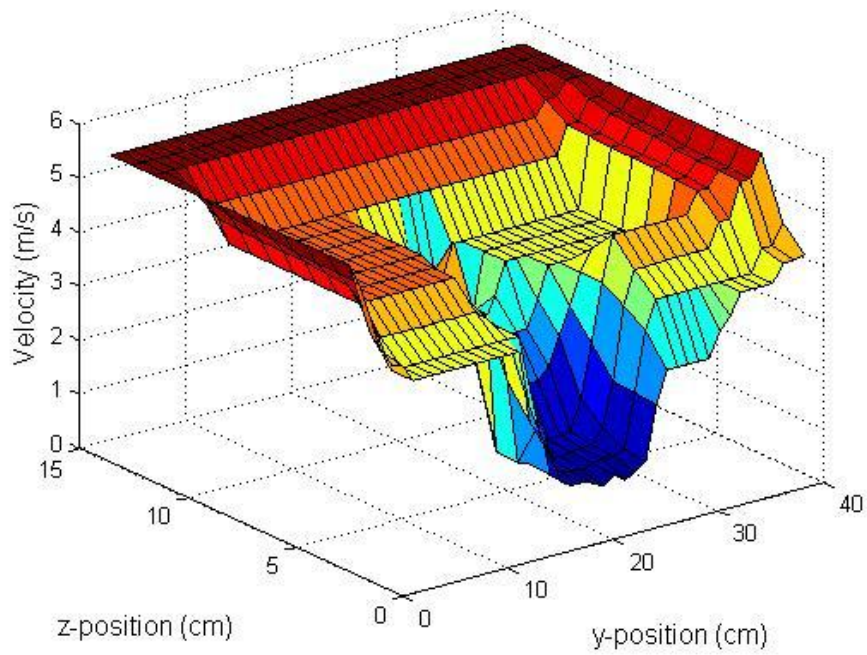
Figure 6.22 Wake Behind the Ahmed Body at Reynolds Number 0.95×10^5 (x=16cm)
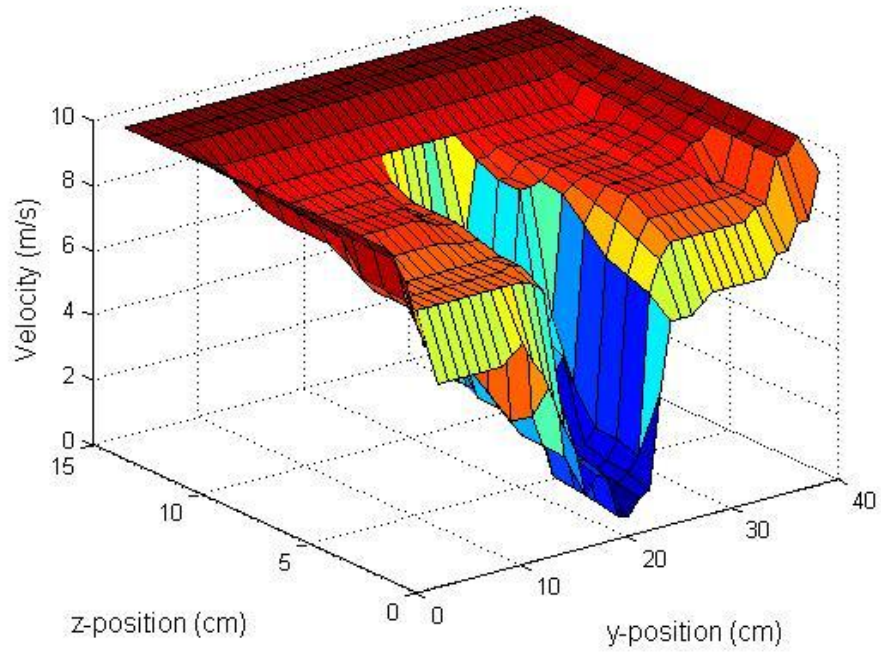
Figure 6.23 Wake Behind the Ahmed Body at Reynolds Number 1.71×10^5 (x=16cm)
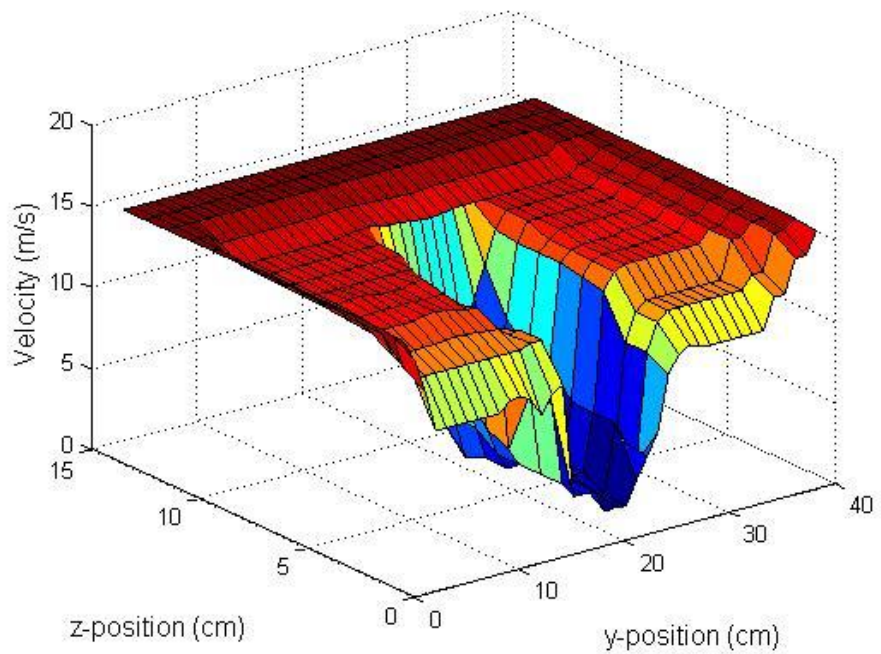
Figure 6.24 Wake Behind the Ahmed Body at Reynolds Number 2.61×10^5 (x=16cm)
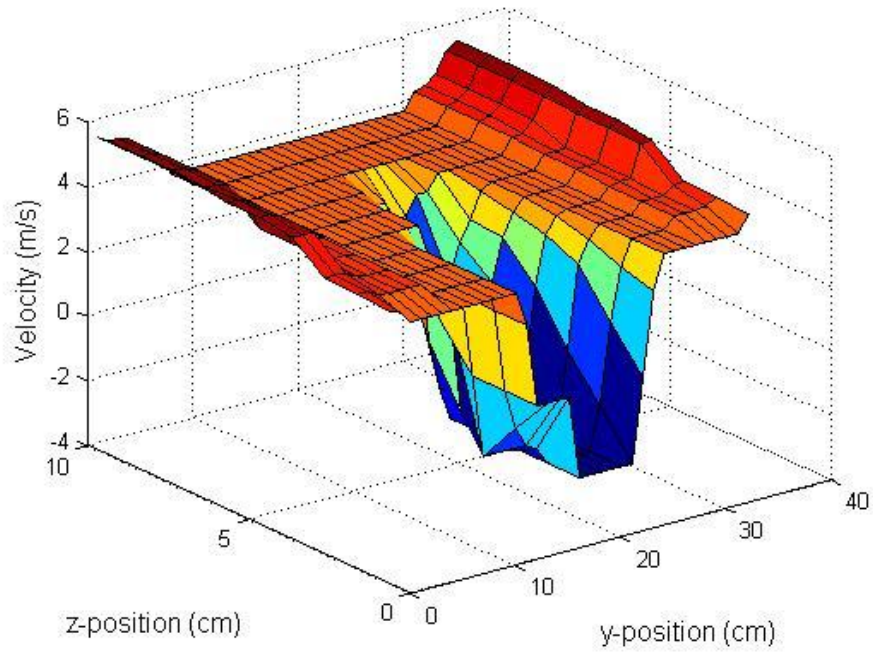
Figure 6.25 Wake Behind the MIRA Notchback Model at Reynolds Number
0.83×10^5 (x=1cm)
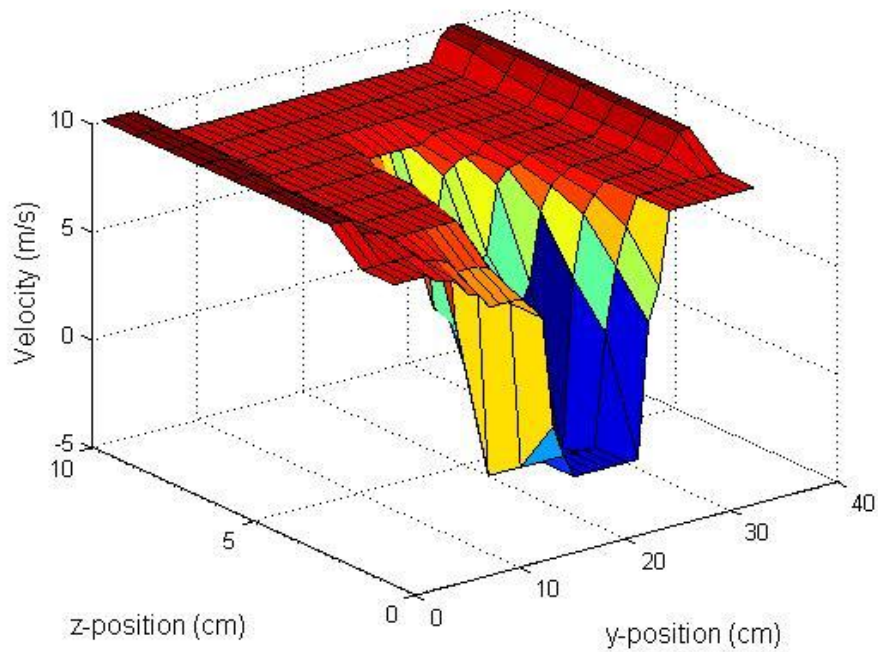
Figure 6.26 Wake Behind the MIRA Notchback Model at Reynolds Number
1.53×10^5 (x=1cm)
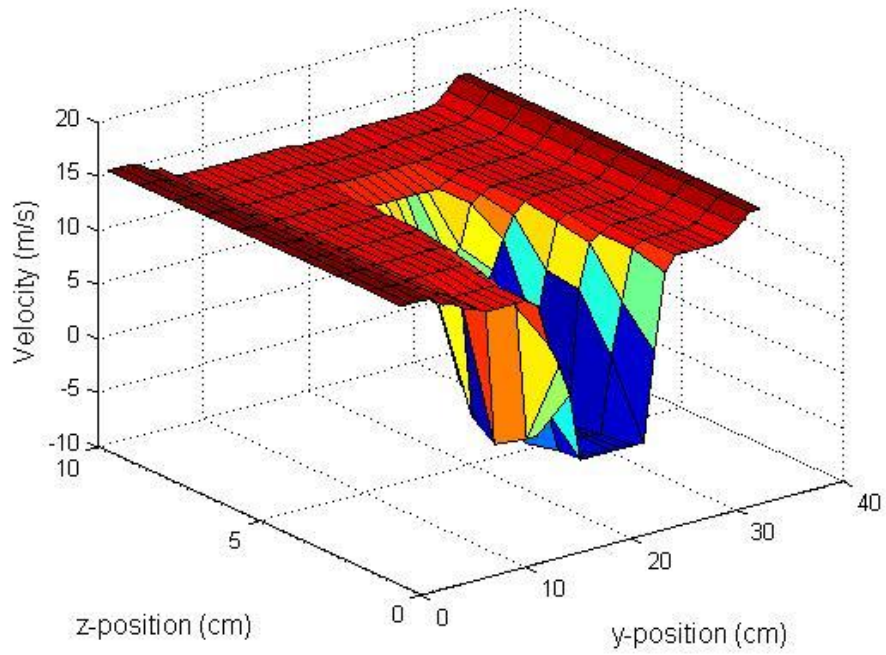
Figure 6.27 Wake Behind the MIRA Notchback Model at Reynolds Number
2.29×10^5 (x=1cm)
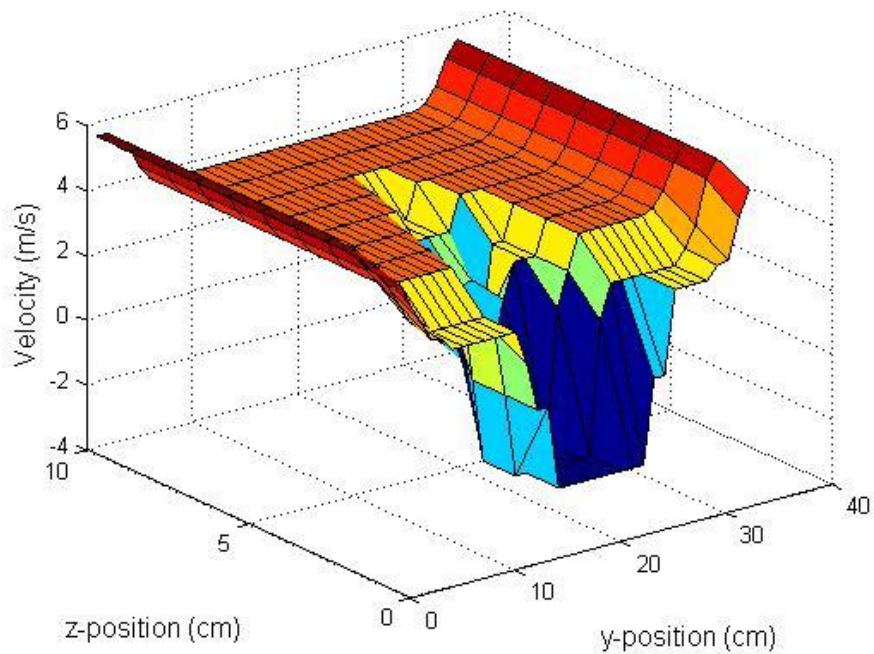
Figure 6.28 Wake Behind the MIRA Notchback Model at Reynolds Number
0.83×10^5 (x=4cm)
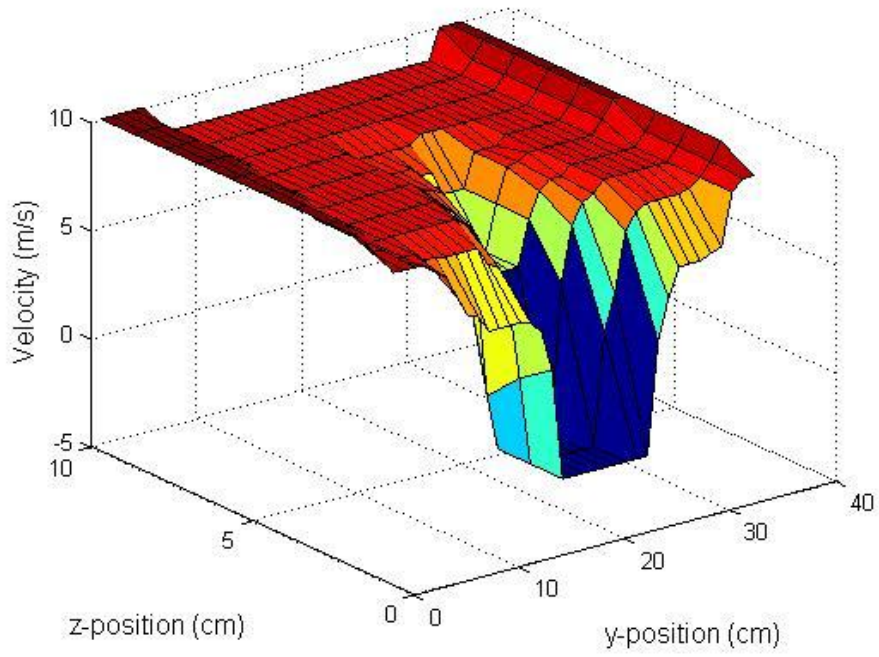
Figure 6.29 Wake Behind the MIRA Notchback Model at Reynolds Number
1.53×10^5 (x=4cm)
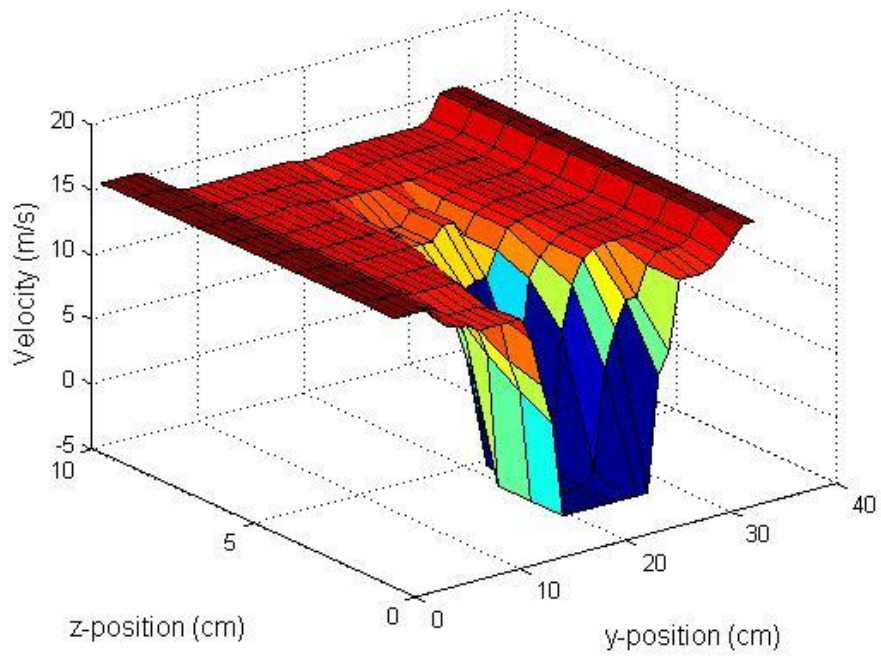
Figure 6.30 Wake Behind the MIRA Notchback Model at Reynolds Number
2.29×10^5 (x=4cm)
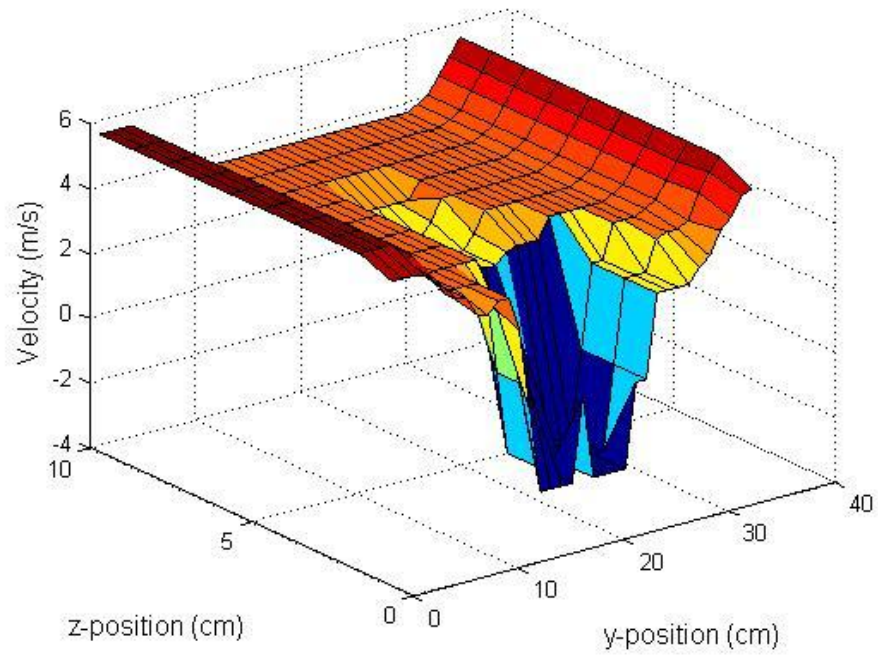
Figure 6.31 Wake Behind the MIRA Notchback Model at Reynolds Number
0.83×10^5 (x=7cm)
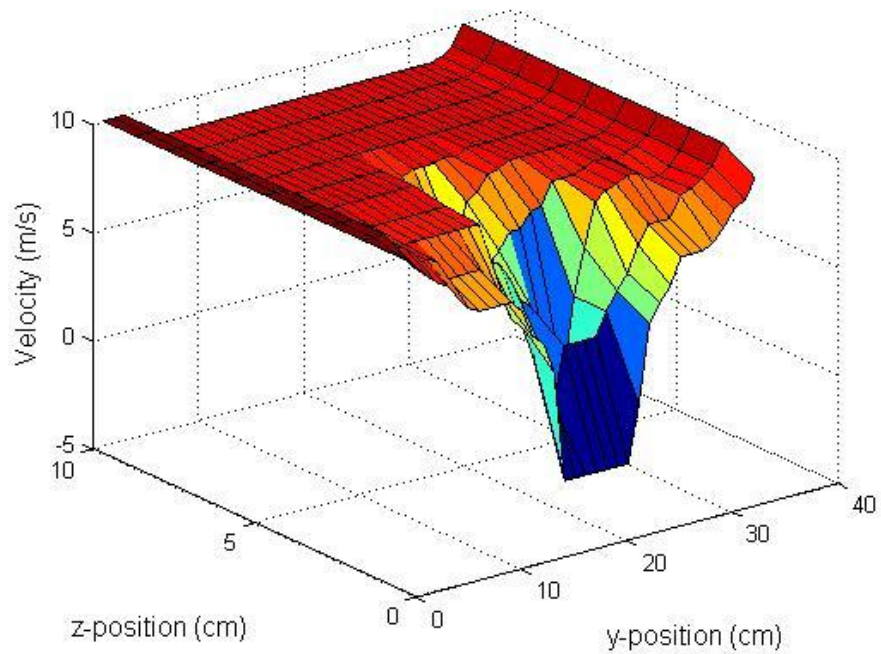
Figure 6.32 Wake Behind the MIRA Notchback Model at Reynolds Number
1.53×10^5 (x=7cm)
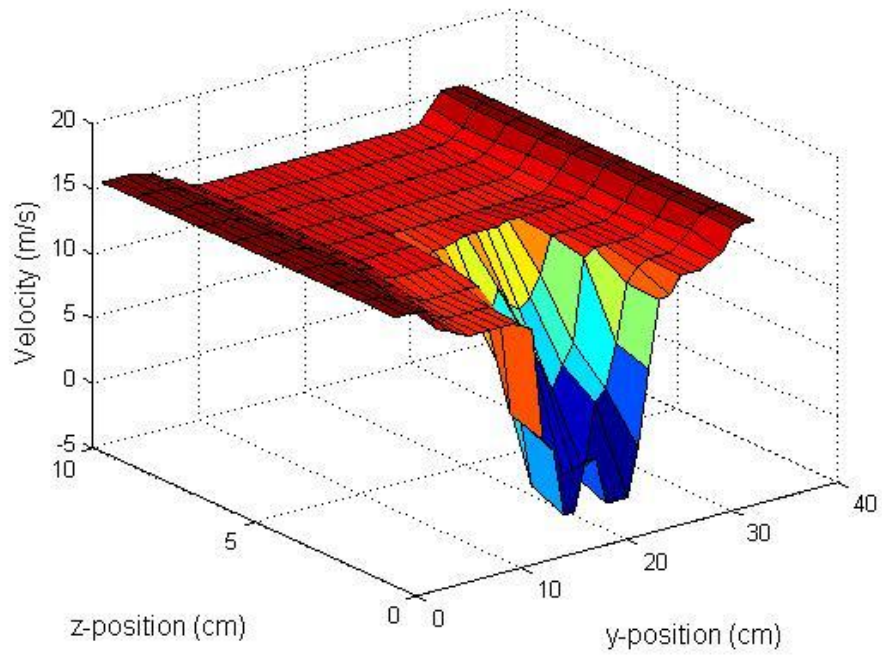
Figure 6.33 Wake Behind the MIRA Notchback Model at Reynolds Number
2.29×10^5 (x=7cm)
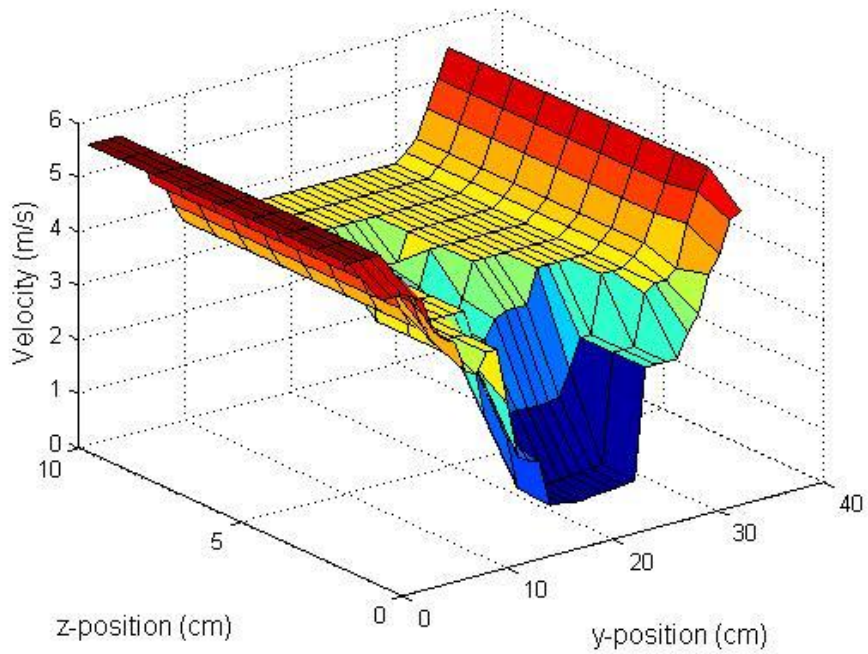
Figure 6.34 Wake Behind the MIRA Notchback Model at Reynolds Number
0.83×10^5 (x=10cm)
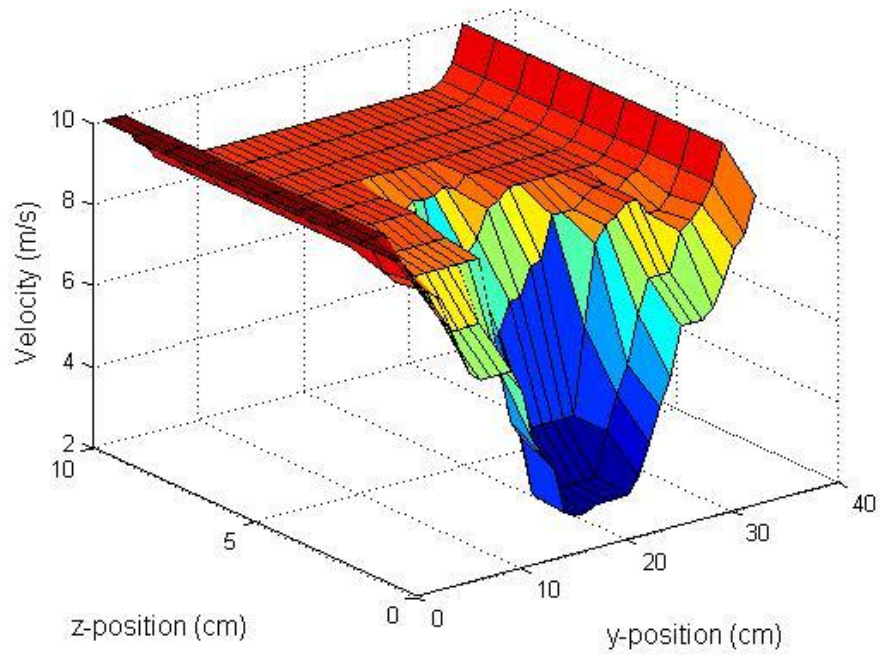
Figure 6.35 Wake Behind the MIRA Notchback Model at Reynolds Number
1.53×10^5 (x=10cm)
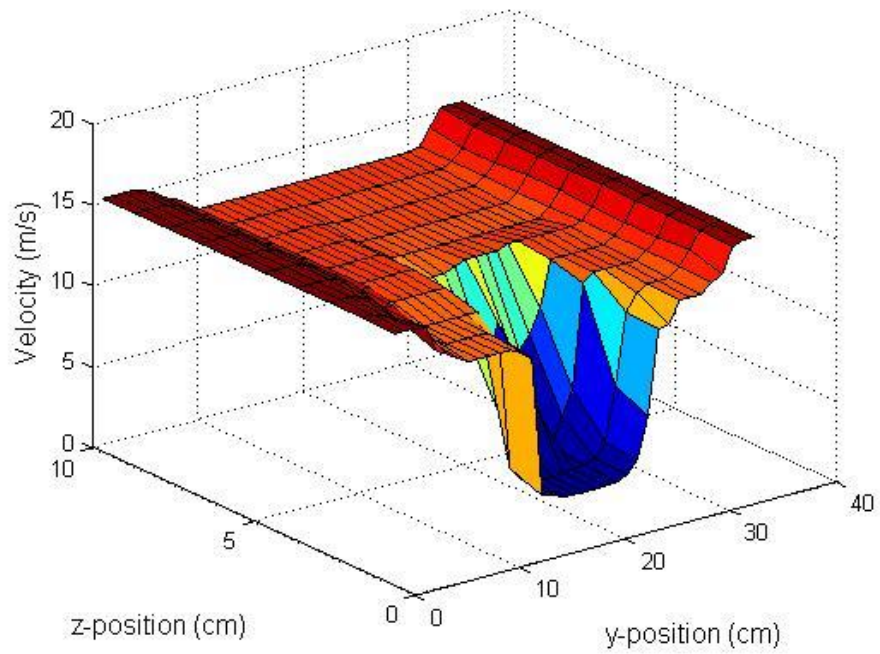
Figure 6.36 Wake Behind the MIRA Notchback Model at Reynolds Number
2.29×10^5 (x=10cm)

In order to obtain above figures, plenty of data were measured behind the Ahmed Body and MIRA Notchback model. The measurements were completed at 10 cm in the x-direction because of the Ahmed Body has a bluff body more than MIRA Notchback model. The velocity in the wake was smaller than the free stream velocity. Velocity at some points had minus values. This means that there were reverse velocities behind the reference model. These minus regions were determined via manometer firstly. Then, the values of these velocities were measured by the commercial hot-wire system At y-coordinate as moving away from the wake of model, the velocity increased and then, reached the free stream velocity. When the Pitot tube was very close to the reference model, the velocity distribution in the wake was too complicated. Especially because of the boundary layer in the test section ground, sometimes the velocity could not reach the free stream velocity. As moving away at x-coordinate velocity distribution was obtained as expected.

Table 6.3 The Drag Coefficient Results of Ahmed Body

x (cm)	Reynolds Number $(0,95 \times 10^5)$		Reynolds Number $(1,71 \times 10^5)$		Reynolds Number $(2,61 \times 10^5)$	
	C_d	The Difference Between Measured Value (%)	C_d	The Difference Between Measured Value (%)	C_d	The Difference Between Measured Value (%)
1	2,183	276,4	1,229	105,9	1,372	122,7
3	2,127	266,7	1,138	90,6	1,296	110,4
5	1,921	231,2	1,104	84,9	1,118	81,5
7	1,868	222,1	0,916	53,4	1,097	78,1
12	1,627	180,5	0,803	34,5	0,868	40,9
14	1,592	174,5	0,794	33,0	0,792	28,6
16	1,017	75,3	0,688	15,2	0,733	18,9

Table 6.4 The Drag Coefficient Results of MIRA Notchback Model

| x (cm) | Reynolds Number $(0,83 \times 10^5)$ | | Reynolds Number $(1,53 \times 10^5)$ | | Reynolds Number $(2,29 \times 10^5)$ | |
	C_d	The Difference Between Measured Value (%)	C_d	The Difference Between Measured Value (%)	C_d	The Difference Between Measured Value (%)
1	1,158	309,2	0,685	145,5	0,549	103,3
4	1,242	338,9	0,599	114,7	0,512	89,6
7	0,738	160,8	0,497	78,1	0,473	75,2
10	0,537	89,7	0,349	25,1	0,329	21,8

In the literature for the 30^0 slant angle Ahmed Body, it is predicted that the most appropriate downstream location in order to conduct experiments is 0.3L (L is the length of the Ahmed Body). However, there were reverse flows at 0,3L cm away from the rear surface in this study. Reverse flows affected the results adversely. Because of the reverse flows, measurement errors and assumptions in the calculations the drag coefficient of reference models are quite higher than literature.

6.3 Pressure Distribution Results

Surface pressure distributions of the Ahmed Body and MIRA Notchback model are shown in this part. Locations of pressure taps are demonstrated in Appendices part. Pressure distributions are presented for different Reynolds number.
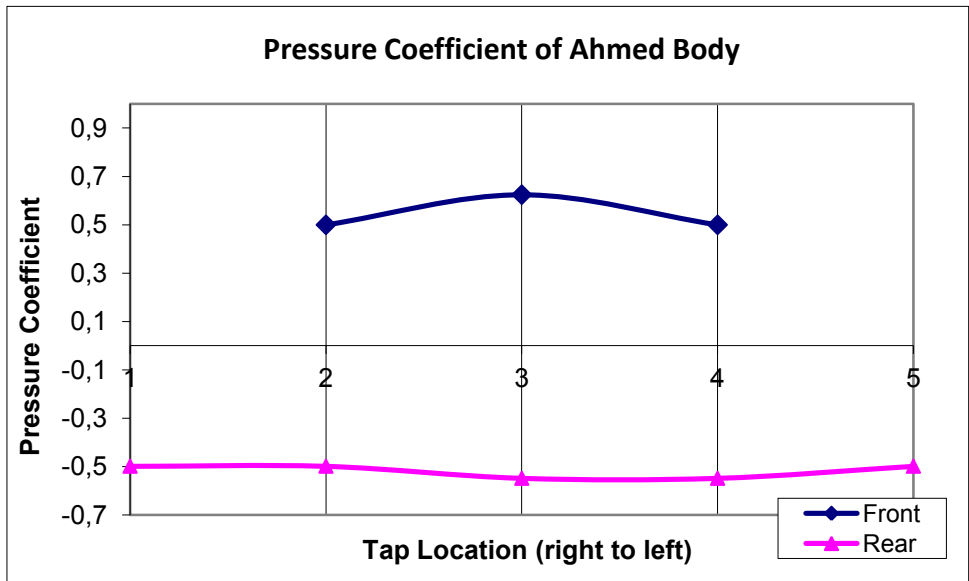
Figure 6.37 Pressure Coefficient Distribution at the Centerlines of Front and Rear Surfaces for Reynolds number 0.95×10^{5}
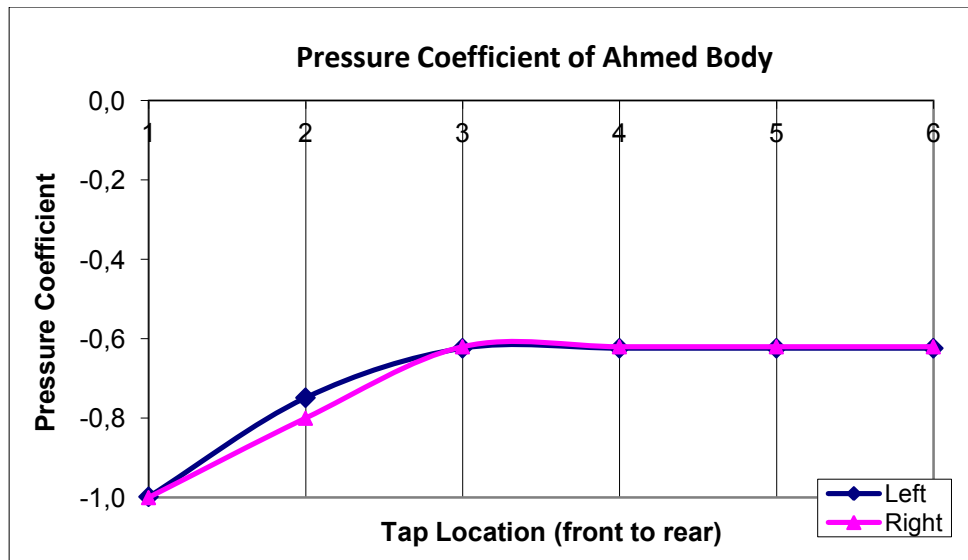
Figure 6.38 Pressure Coefficient Distribution at the Centerlines of Right and Left Surfaces for Reynolds number 0.95×10^{5}
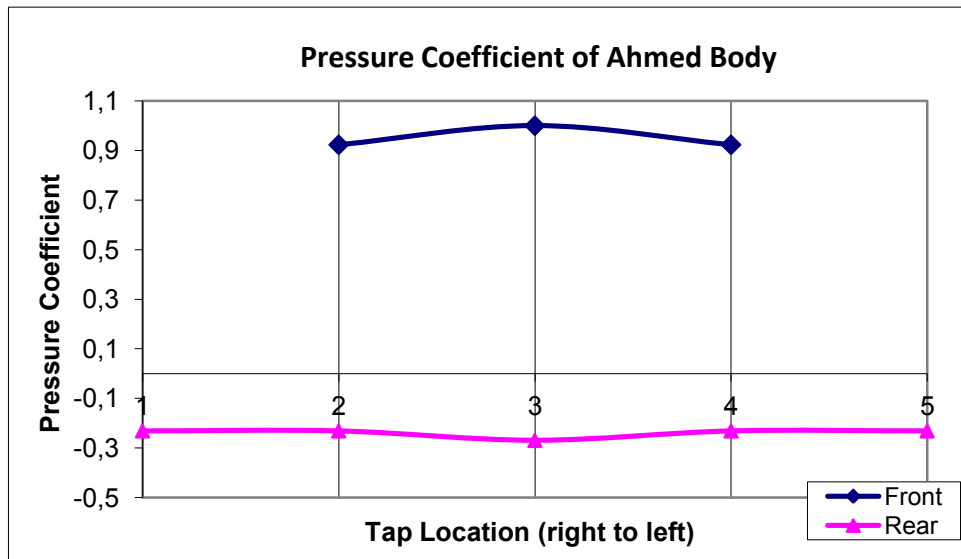
Figure 6.39 Pressure Coefficient Distribution at the Centerlines of Front and Rear Surfaces for Reynolds number 1.71×10^{5}
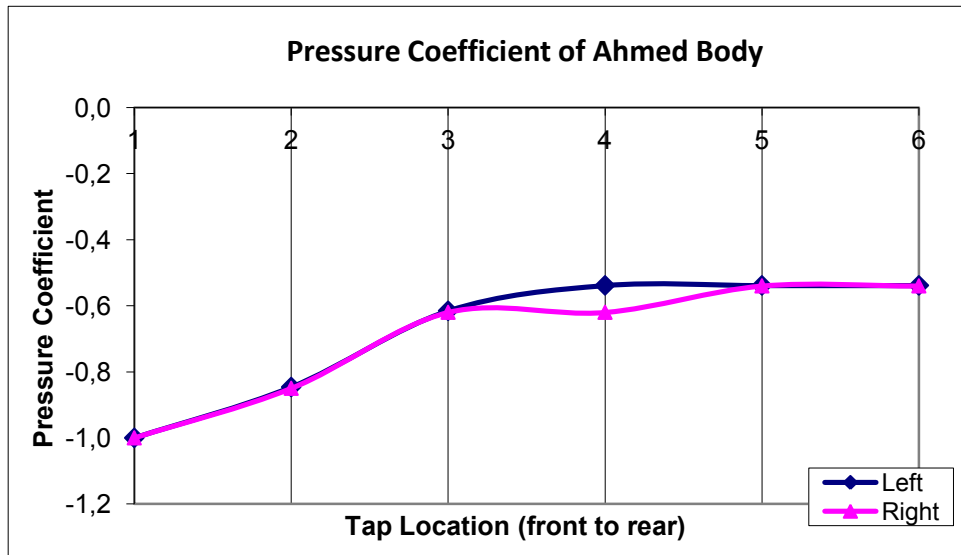
Figure 6.40 Pressure Coefficient Distribution at the Centerlines of Right and Left Surfaces for Reynolds number 1.71×10^{5}
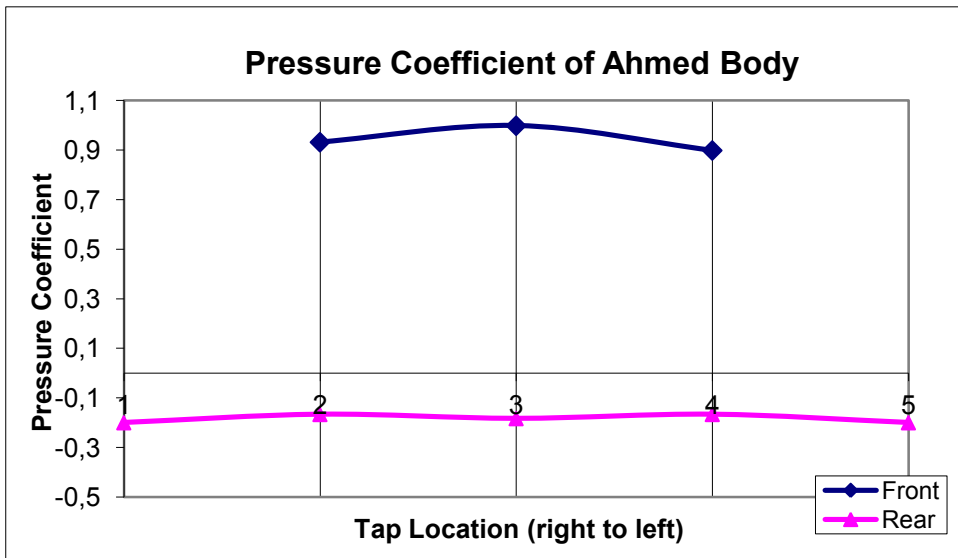
Figure 6.41 Pressure Coefficient Distribution at the Centerlines of Front and Rear
Surfaces for Reynolds number $2.61\text{x}10^5$
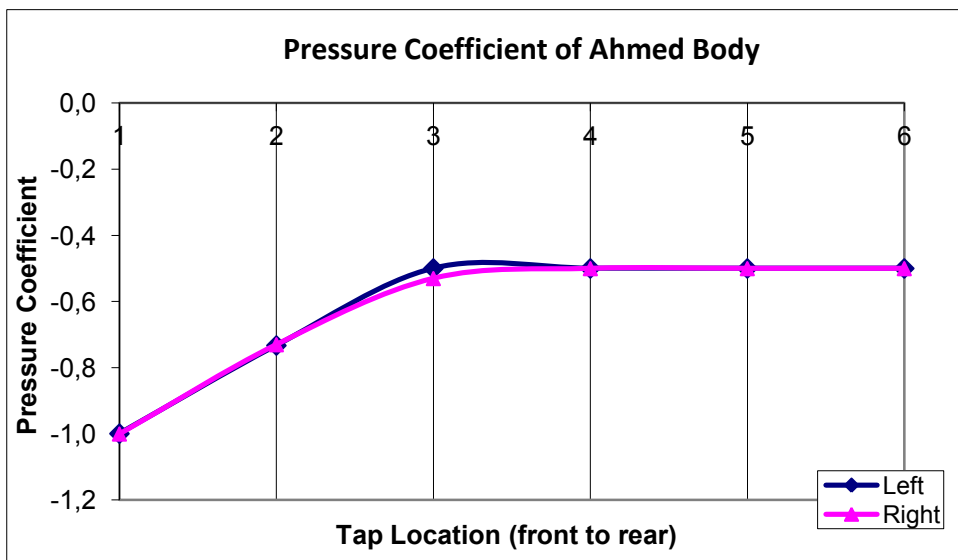
Figure 6.42 Pressure Coefficient Distribution at the Centerlines of Right and Left
Surfaces for Reynolds number $2.61\text{x}10^5$
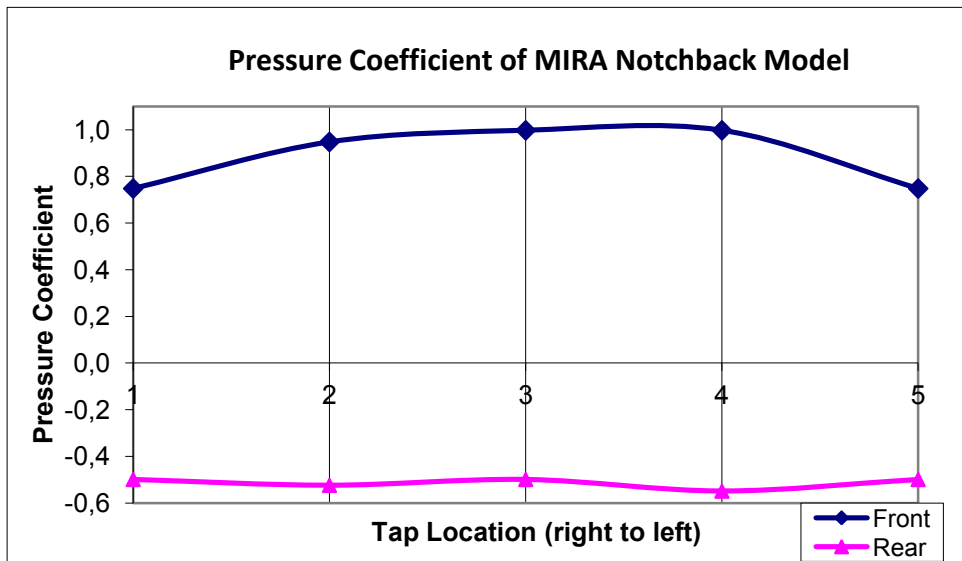
Figure 6.43 Pressure Coefficient Distribution at the Centerlines of Front and Rear Surfaces for Reynolds number 0.83×10^5
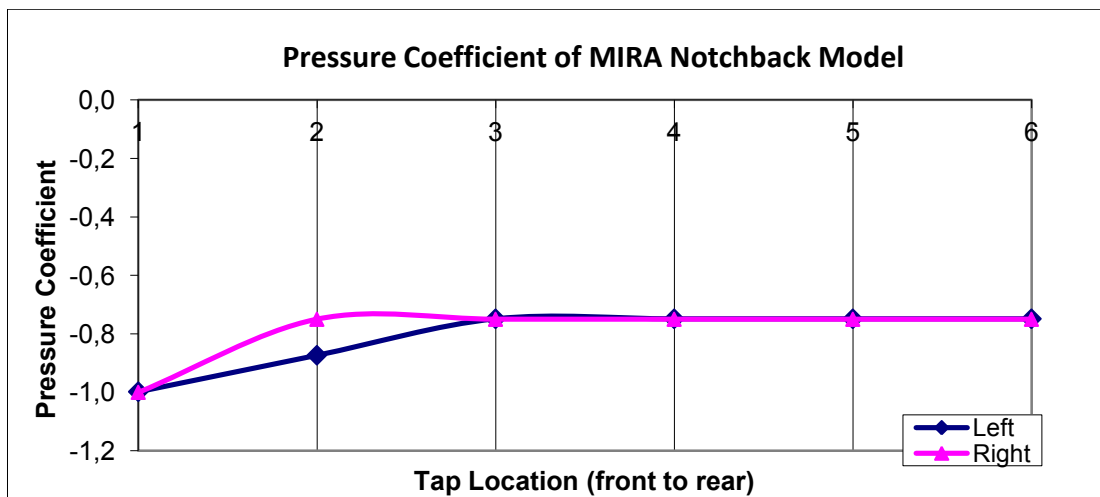
Figure 6.44 Pressure Coefficient Distribution at the Centerlines of Right and Left Surfaces for Reynolds number 0.83×10^5
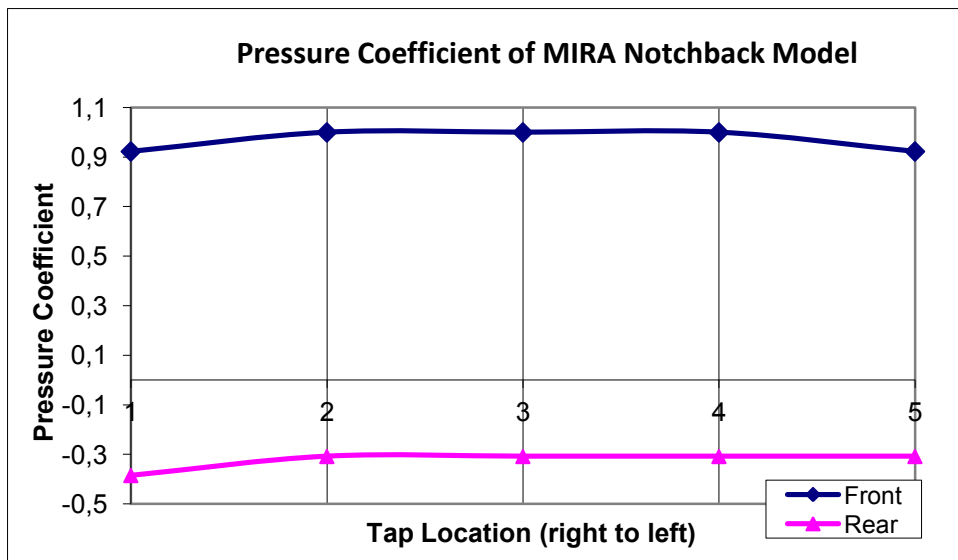
Figure 6.45 Pressure Coefficient Distribution at the Centerlines of Front and Rear Surfaces for Reynolds number 1.53×10^5
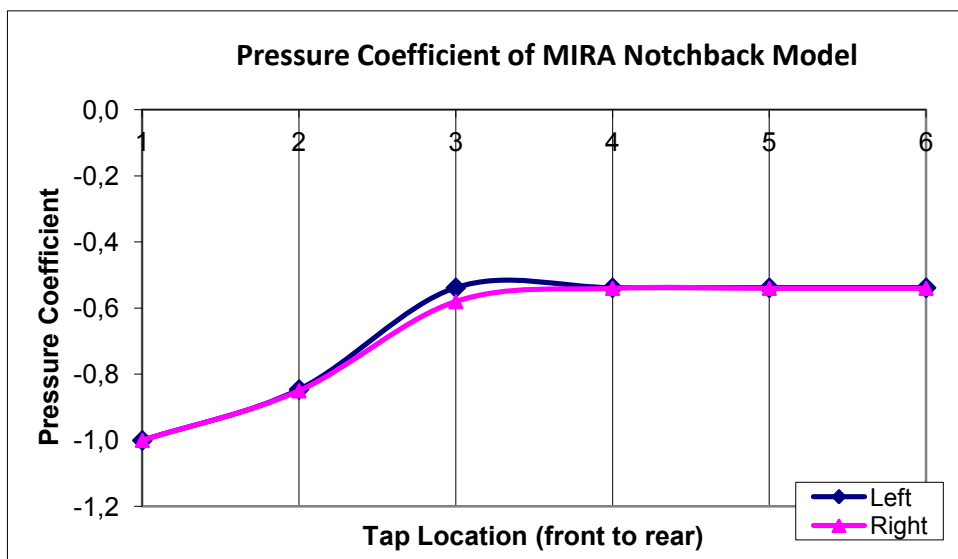
Figure 6.46 Pressure Coefficient Distribution at the Centerlines of Right and Left Surfaces for Reynolds number 1.53×10^5
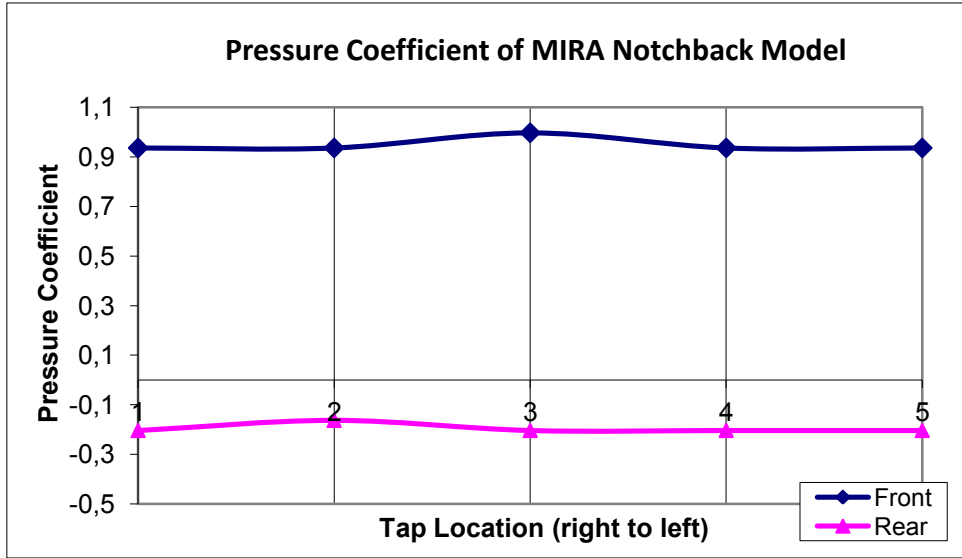
Figure 6.47 Pressure Coefficient Distribution at the Centerlines of Front and Rear Surfaces for Reynolds number 2.29×10^5
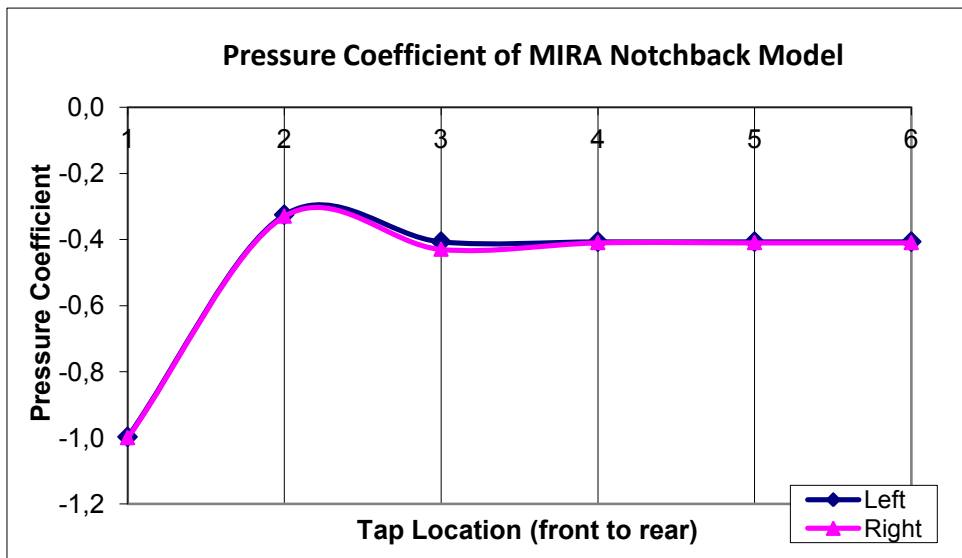

Figure 6.48 Pressure Coefficient Distribution at the Centerlines of Right and Left Surfaces for Reynolds number 2.29×10^5

Pressure coefficient is the pressure difference between each tap and the reference location divided by dynamic pressure at the reference location. In order to determine pressure coefficients of reference models, many pressure taps were located on centerline of each surface. There are three pressure tap locations in front, five tap locations at rear and six pressure tap locations at left and right surface of the Ahmed Body. The MIRA Notchback model has five tap locations at rear and front surface and six tap locations at left and front surfaces.

According to theory, it is expected that the pressure coefficient values measured at left and right surfaces should be same because it is assumed that there is not yaw angle or another model to cause an aerodynamic effect on the reference models. However, at the left surface obtained pressure coefficient values are not equal to right surface ones. The reason for this result may be the existence of side forces in the wind tunnel test section. In addition, although the reference models were tried to locate very carefully at the test section ground, there were slip with respect to location. There were also measurement errors.

As seen in these figures, if the Cp value is zero that shows the pressure is the same as the free stream pressure. When the value of Cp is one, the pressure is stagnation pressure and this point can be called stagnation point. If the Cp has minus value that means there is suction. Around the Ahmed Body the points have positive coefficients up to one and negative pressure coefficients. Negative coefficients can be less than minus one. However pressure coefficients will not exceed plus one since the highest pressure that is obtained is the stagnation pressure.

Drag coefficients of left and right surfaces have negative values. At the first pressure tap, the pressure coefficient value of left and right surface almost -1. The reason of this value is this pressure tap location is very near to the edge between the front and side edges. At this location air molecules slow down then there will be a reduction in speeds and increase in pressures.

When investigating the pressure tap location in front surface, it can be seen that the pressure coefficients have positive values. When the air molecules approach the front of the reference models, they begin to compress and in doing so air molecules increase the pressure in front of the model.

In front surface, the middle tap location pressure coefficient is 1 in front surface. This middle pressure tap location can be called the stagnation point. That means the static pressure which is read from this pressure tap is equal to the total pressure in the wind tunnel test section.

Pressure coefficient values are negative at the rear surface. According to theory, the pressures should be constant at the rear surface. The pressure reduction occurs at the rear end of the reference model because a continuous vacuum in the rear model sucks in the opposite direction of the motion of the reference model. In this study, the pressure coefficient values were not obtained constant. The reason for this result may be the measurement errors in the experiments.

Comparing with previous studies, front and rear pressure distribution results of the Ahmed Body and MIRA Notchback model were as predicted. The measurements from rear tap locations would be same. According to theory, pressure coefficient values of the left and right surfaces would be overlapped. In this study very close values of pressure distributions were observed at left and right surfaces.

CHAPTER 7

CONCLUSIONS AND RECOMMENDATIONS

In this chapter, the conclusions and comments of the experimental results are discussed. In addition some recommendations are also presented.

7.1 Conclusions

In the scope of this study, aerodynamic interactions of two different types of vehicles ere investigated at three different Reynolds number. Drag forces and surface pressures of the models at each Reynolds number were measured according to this aim. Continuity method was used as a Blockage correction method. The results were discussed and compared with the results of the studies found in the literature.

The drag coefficient of Ahmed Body was measured as 0.580 at 0.95×10^5 Reynolds number, 0.597 at 1.71×10^5 Reynolds number and 0.616 at 2.61×10^5 Reynolds number. The drag coefficient of the MIRA Notchback model was measured as 0.283 at 0.83×10^5 Reynolds number, 0.279 at 1.53×10^5 Reynolds number and 0.270 at 2.29×10^5 Reynolds number.

For the measurements conducted at METU Mechanical Engineering Fluid Mechanics Laboratory. The blockage ratio of 1/4 scale Ahmed Body is 3.1% and 1/18 scale MIRA Notchback model is 2.6%.

The drag coefficients of Ahmed Body measured via balance system were higher than the drag coefficient of literature. The main reason for this result may be induced

drag. Attaching the balance system to the model may cause lift force. This lift force may generate the induced drag. Induced drag influences the total drag adversely. When comparing the obtained drag coefficient of MIRA Notchback model with literature, it is understood that the results are convenient.

Surface pressure measurements of reference models were conducted for three different Reynolds number. Although because of the measurement errors there were some differences between the obtained results and literature, the results are appropriate. In front surface of the model, the pressure coefficient values are positive. At the rear surface of the model, the pressure coefficients have negative values.

Drag coefficient of Ahmed Body and MIRA Notchback model which are found via wake analyze method are quite higher than literature. There are some reasons. First of all, the reverse flow of the wake affects the calculations and results. In addition, the v- and w- components of velocity were neglected. These neglecting influence the results adversely. The tool which was used in order to determine the surface equations of 3D plotting produced the approximations. Moreover, in the measurements, the velocity could not reachin all directions within the investigation limits. These deficiencies affect the measurement results unfavorably.

7.2 Future Work Recommendations

As a future work, the following recommendations can be taken into consideration. CFD analyses of reference models can be performed at the same conditions. Drag force of Ahmed Body and MIRA Notchback model can be investigated at high Reynolds number. In order to measure other aerodynamic forces or moments of reference models, a new balance system can be designed. Different models can be investigated at the same wind tunnel test section and the effect of model size on aerodynamic forces can be compared.

REFERENCES

[1] Hucho W.H., Sovran G., "Aerodynamics of Road Vehicles", Annual Reviews of Fluid Mechanics, 485-537, 1993.

[2] Ahmed, S.R., Ramm, G. And Faltin, G., "Some salient features of the time averaged ground vehicle wake" SAE Transactions, Volume 93, Part 2, 473-503, 1984.

[3] Sims-Williams D.B. and Dominy R.G., "Experimental Investigation into Unsteadiness and Instability in Passenger Car Aerodynamics", SAE Transactions, SAE Paper 980391, 1998.

[4] Duell E.G., George A.R., "Experimental Study of a Ground Vehicle Body Unsteady Near Wake", SAE Transactions, Volume 108, 1589-1601, 1999.

[5] Berger E., Scholz D., Schumm M., "Coherent Vortex Structures in the Wake of a Sphere and Circular Disk at Rest and Under Forced Vibrations", Journal of Fluids and Structures", 231-257, 1990.

[6] Templin J.T. andRaimondo S., "Experimental Evaluation of Test Section Boundary Interference Effects in Road Vehicle Tests in Wind Tunnels", Journal of Wind Engineering and Industrial Aerodynamics, Volume 22, 129-148, 1986.

[7] Williams J., Wallis S., Hoffman J., Martindale B., Arnette S., "Effect of Test Section Configuration on Aerodynamic Drag Measurements", SAE Transactions, Volume 110, Part 1, 680-694, 2001.

[8]   Mercker E., "A Blockage Correction for Automotive Testing in a Wind Tunnel with Closed Test Section", Journal of Wind Engineering and Industrial Aerodynamics, Volume 22, 149-167, (1986).

[9]   Gümüşlüol Ü., "Experimental Investigation of the Aerodynamic Interactions of Vehicle in Close-Following and Passing Situations", MSc Thesis, METU, June, 2006.

[10]   Örselli E., "Computation of Drag Force on Single and Close-following Vehicles", MSc Thesis, METU, September, 2006.

[11]   Wu J., Liu J., "Development of a Predictive System for Car Fuel Consumption Using an Artificial Neural Network", Expert Systems with Applications, Volume 38, 4967-4971, 2011.

[12]   Barnard, R.H., "Road Vehicle Aerodynamic Design", 1st Edition, Longman, 1996.

[13]   Fluid Flow, www.roymech.com, last visited on July 2013.

[14]   Aksel H., "Fluid Mechanics", Middle East Technical University, 2010.

[15]   Modeling, Similarity, and Dimensional Analysis, www.mcgraw-hill.com, last visited on July 2013.

[16]   White, F.M. "Fluid Mechanics" 4th Edition, McGraw Hill Education, 1998.

[17]   Sahini D., "Wind Tunnel Blockage Corrections: a Computational Study", MSc Thesis, Texas Tech University, 2004.

[18] Tiainen J.S., "Use of CFD to Design a Future CFD/Experimental Wind Tunnel Program to Investigate the Blockage Effects of Bluff Bodies with Significant Upwash", MSc Thesis, Cranfield University, September, 2002.

[19] Talamelli A., Westin J., "Drag Measurements Through Wake Analysis", Vehicle Aerodynamics, Stockolm, 2004.

[20] Fluke 922 Airflow Meter, www.fluke.com, last visited on July 2013.

[21] Measurement principles of LDA, www.dantecdynamics.com, last visited on July 2013.

[22] Description of Drag, www.cortana.com, last visited on July 2013.

[23] Vehicle Aerodynamics, www.kasravi.com, last visited on July 2013.

[24] Murad N., Naser J., Alam F., Watkins S., "Computational Fluid Dynamics Study of Vehicle A-Pillar Aeroacustics", Applied Acoustics, Volume 74, 882-896, 2013.

[25] Hackett J. E., Sugavanam A., "Evaluation of a Complete Wake Integral for the Drag of a Car-like Shape" SAE Technical Papers Series 840507, 1984.

[26] Gullman-Strand J., Angele K., "Wake Analysis and Measurements", Department of Mechanics, KTH, August, 2000.

[27] Browand F., Michaelian M., "Field Experiments Demonstrate Fuel Savings for Close-Following", California PATH Research Report, UCB-ITS-PRR-200-14, University of California, 2004.

[28] Taştan U., "Investigation of Turbulence Models Used in Automotive Industry", MSc Thesis, METU, September, 2011.

[29] İçingür, Y., Solmaz, H., "Determination of Drag Coefficients of Various Automobile Models in a Low Speed Wind Tunnel", Journal of Faculty of Engineering and Architecture of Gazi University, Volume 26, 455-460, 2011.

[30] Potter M.C., Foss J.F., "Fluid Mechanics", Michigan State University, 1975.

[31] Markland E., "Ön Bilgi Kapsamlı Hava Akımı", Cardiff University, 1976.

[32] Scibor-Rylski A.J., "Road Vehicle Aerodynamics", The City University, 1975.

[33] Hucho W.H., "Aerodynamics of Road Vehicles", Federal Republic of Germany, 1986.

[34] Çengel Y.A., Cimbala J.M., "Fluid Mechanics", McGraw Hill Education, 2008.

[35] ME-410 Characteristics of an Airfoil Lecture Notes, 2013.

[36] Stepper Motor, www.wikipedia.com, last visited on December 2013.

APPENDIX A

SCHEMATIC VIEW OF THE BALANCE
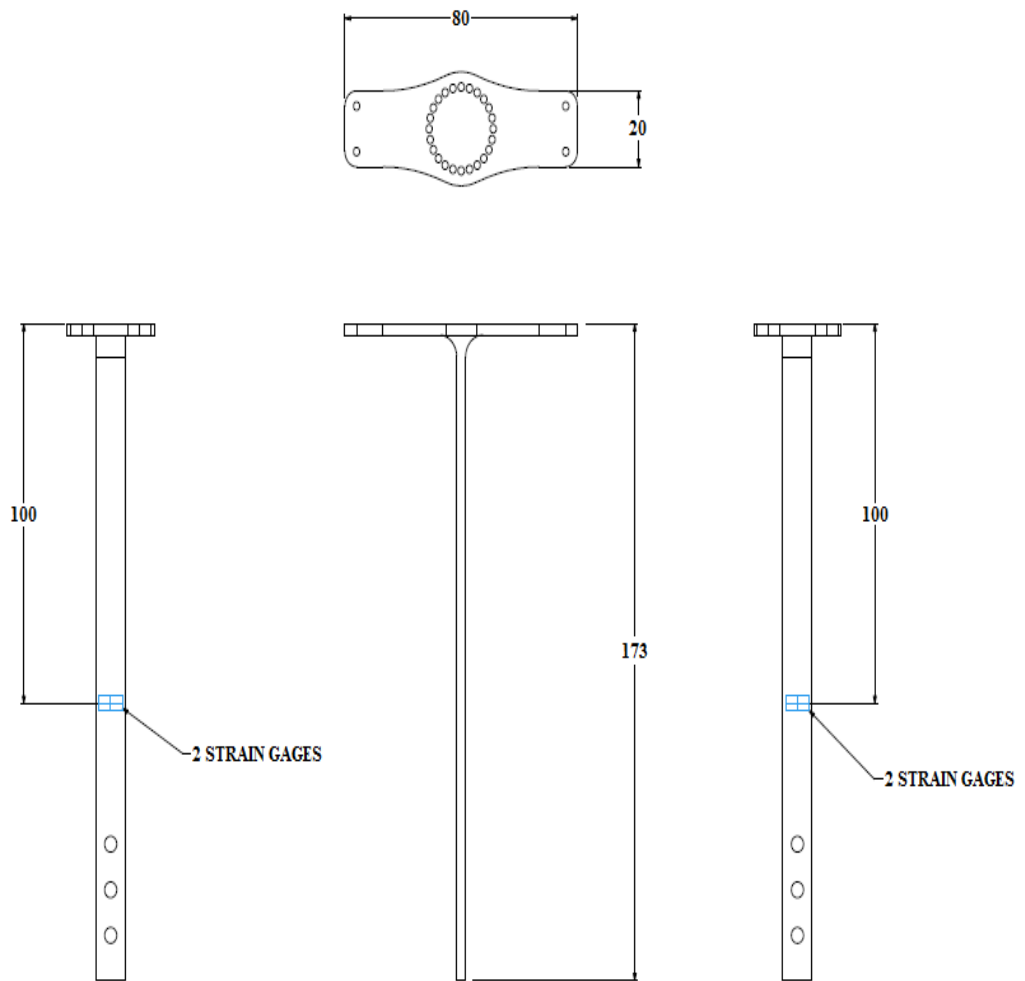
APPENDIX B

LASER-BASED FLOW VISUALIZATIONS RESULTS

Flow visualizations captured with a camera is a very good technique in order to observe the structure of the wake. However, this method is not quantitative. Laser-based flow visualization technique is qualitative method. It gives only insight in the wake structure.

Flow visualization of the Ahmed Body results were obtained by means of Laser light. Smoke was used as tracer particle. Figures demonstrate the flow behind the Ahmed Body and MIRA Notchback model.
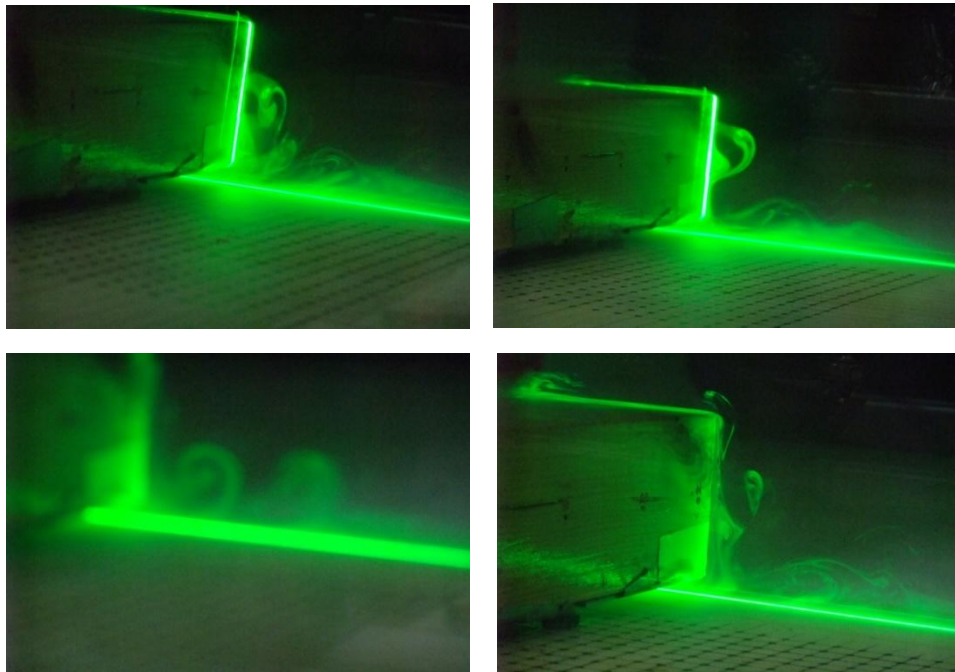
Figure B.1 Flow Structure Behind the Ahmed Body
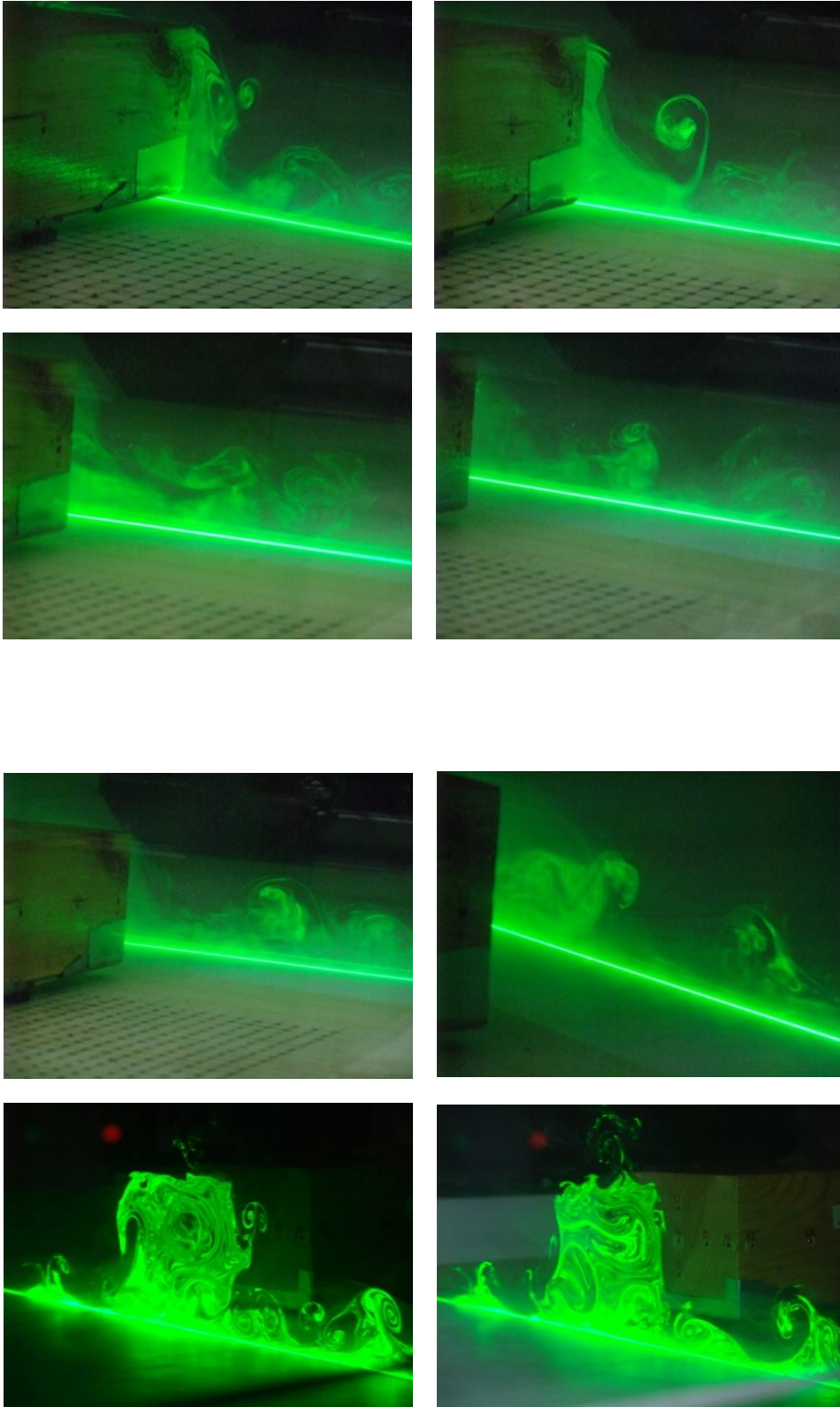
Figure B.1 (Continued) Flow Structure Behind the Ahmed Body
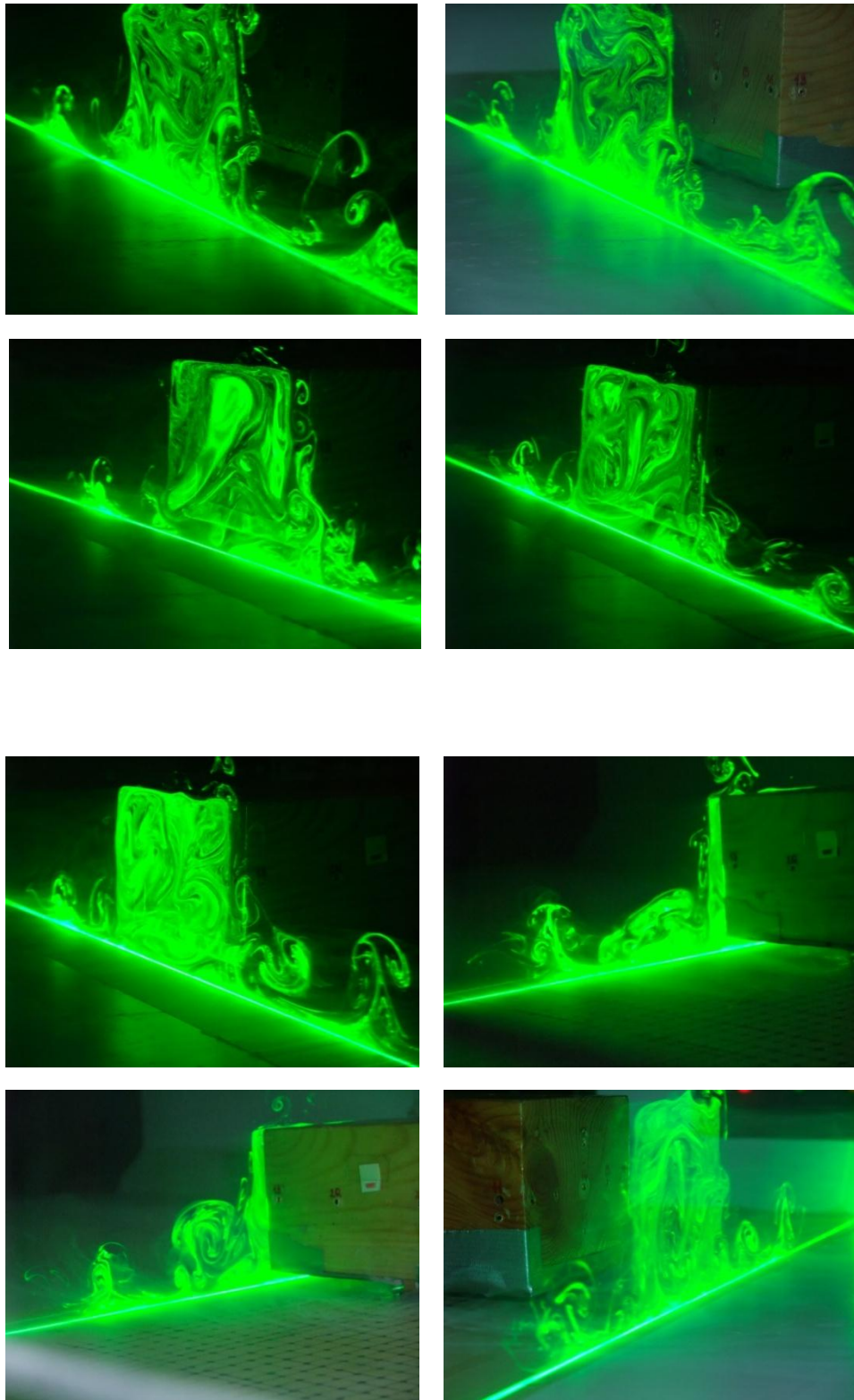
Figure B.1 (Continued) Flow Structure Behind the Ahmed Body
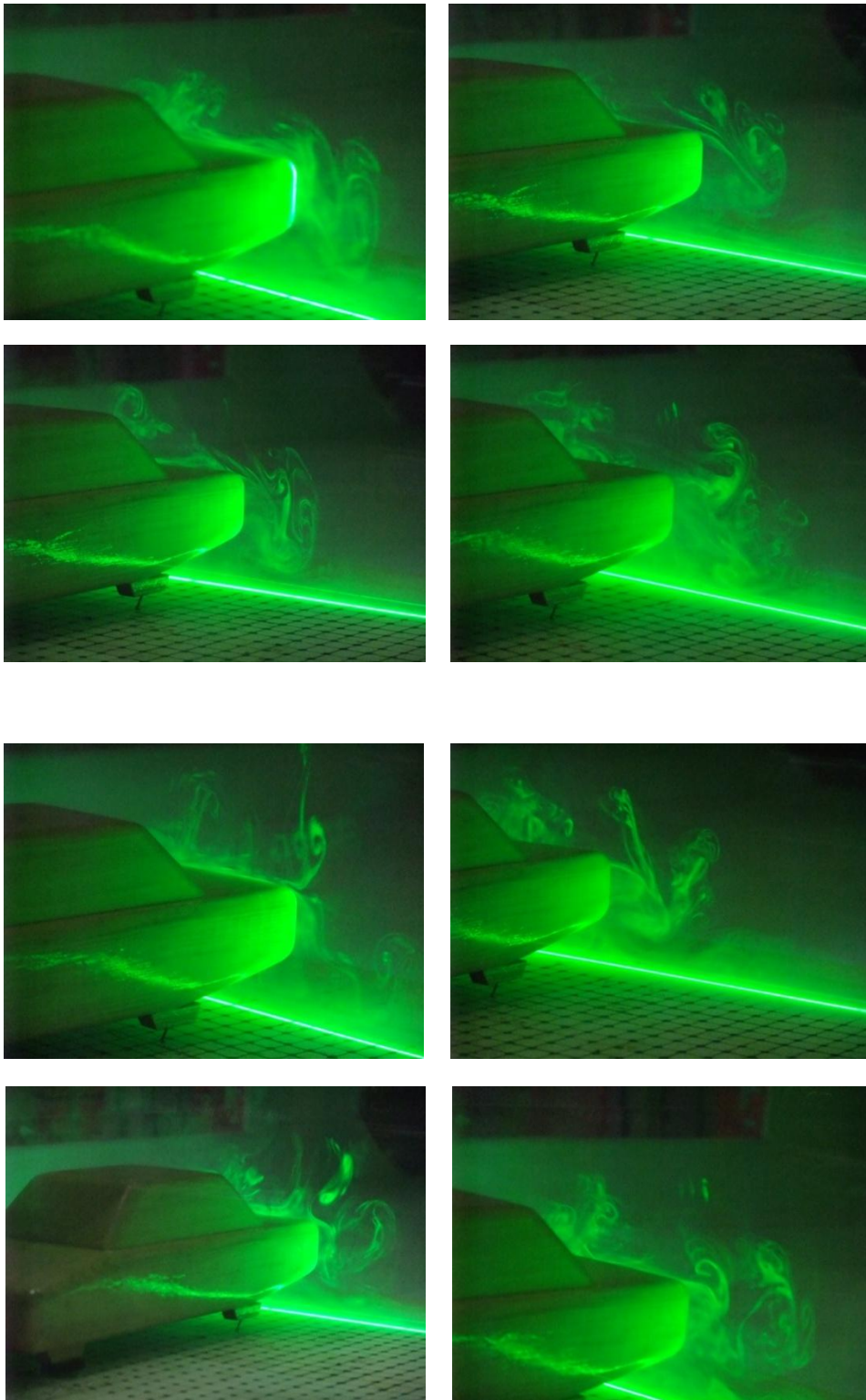
Figure B.2 Flow Structure Behind the MIRA Notchback Model
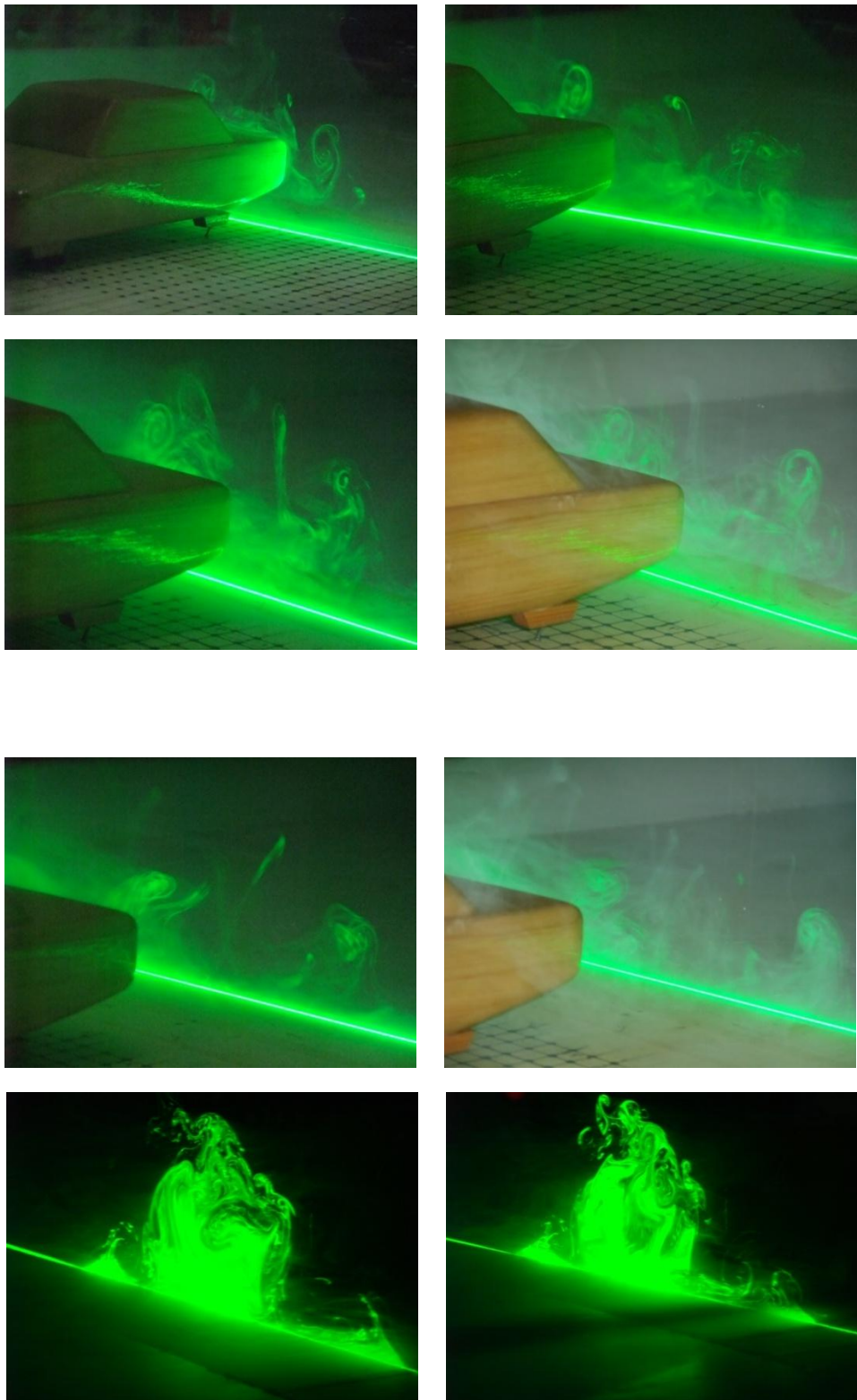
Figure B.2 (Continued) Flow Structure Behind the MIRA Notchback Model
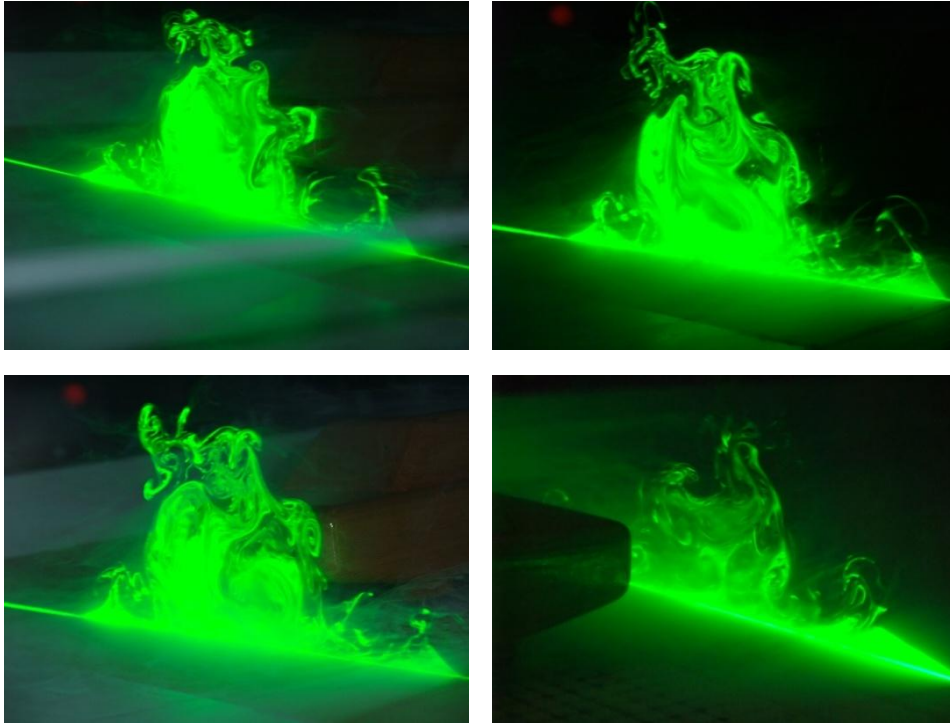
Figure B.2 (Continued) Flow Structure Behind the MIRA Notchback Model

In this part of the study, laser light illuminated the rear of reference models and the wake was photographed. At the beginning of this study, the laser light was very close the rear surface of reference models. Then, the laser light was moved away from the rear surface of the bodies in the x- direction.

The aim of this study is investigating the vortex which was mentioned in the Chapter 2. When laser light was very close the rear surface of reference models, the wake of the bodies were very complicated. However, as moving away in the x- direction, the vortex of reference models could be photographed more easily. In addition, in order to investigate the symmetrical vortex in the wake, the photographing was done from the different perspective.

It is seen that because Ahmed Body has a more blunt shape and sharp edges than MIRA Notchback model and Ahmed Body has a rectangular base with a 0° rear slant angle, the wake of these reference models is different with each other. It is

understood that the size and shape of body are very important parameters which affect the wake of the reference models considerably.

APPENDIX C

NUMERICAL INTEGRATION

In order to determine the drag coefficient via momentum integral method below equation was used.

$$D = \int_{S_3} (p_{0\infty} - p_{03})dS + \frac{1}{2}\rho \int_{S_3} (v^2 + w^2 - u^2)dS \qquad \text{(C.1)}$$

At the beginning of the experiments the wind tunnel of the freestream velocity components were analyzed by Comsol Multiphysics. It was obtained that the v- and w- components of velocity were negligible.

$$D = \int_{S_3} (p_{0\infty} - p_{03})dS + \frac{1}{2}\rho \int_{S_3} -u^2 dS \qquad \text{(C.2)}$$

According to this analyze results and lack of a measurement technique system, the v- and w- component of the velocity were neglected. However, there were u, v, w- components of velocity behind the reference models in the wake. This neglecting affected the results of calculations. The u^2 term of momentum equation was found by the curve fitting toolbox of Matlab. The pressures are the total pressure in the free stream and the total pressure of plane in the wake. These pressures were measured during the experiments via mentioned measurement instruments.

In order to see the accuracy and reliability of the curve fitting toolbox, numerical integration calculation was done for one plane.

In this part of the study, the momentum equation was calculated numerically. Then, the pressure difference between the total pressure in the freestream and total pressure in the wake plane was integrated according to y- and z- directions.

This numerical integration was calculated for the 15.1 m/s freestream velocity at 16 cm downstream location. This plane was chosen because there was not reverse flow which affects the calculation adversely.

After series calculations the drag coefficient was calculated as 0.689. When comparing this result with drag coefficient of Ahmed Body which was determined by balance technique, it is seen that the difference between them is about 12%. However, the difference between them was about 19%. When comparing this result with drag coefficient of Ahmed Body which was found via using curve fitting toolbox, the difference between two calculation methods is about 7%. Because all measured data was taken into account by integration numerically, the drag coefficient of Ahmed Body is better than drag coefficient of Ahmed Body found by curve fitting toolbox.

APPENDIX D

TAP LOCATIONS OF THE REFERENCE MODELS
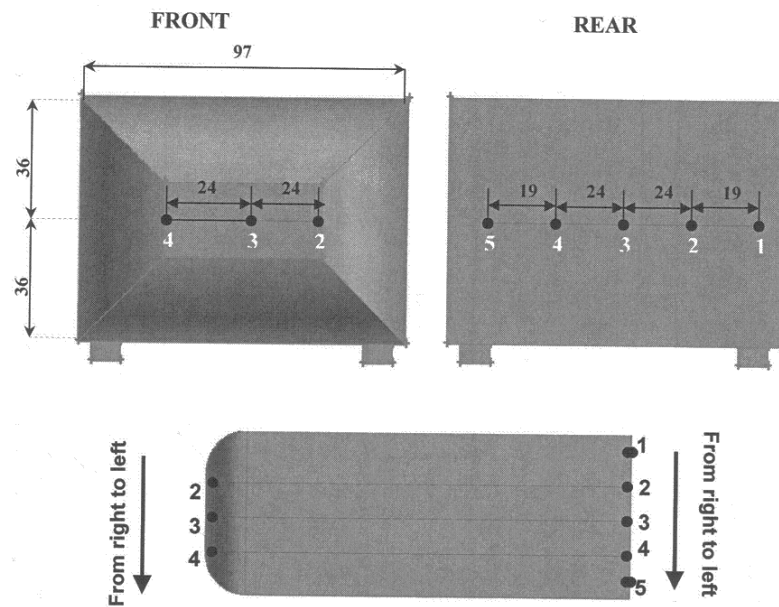
Figure D.1 Tap Locations at the Front and Rear Surfaces of Ahmed Body
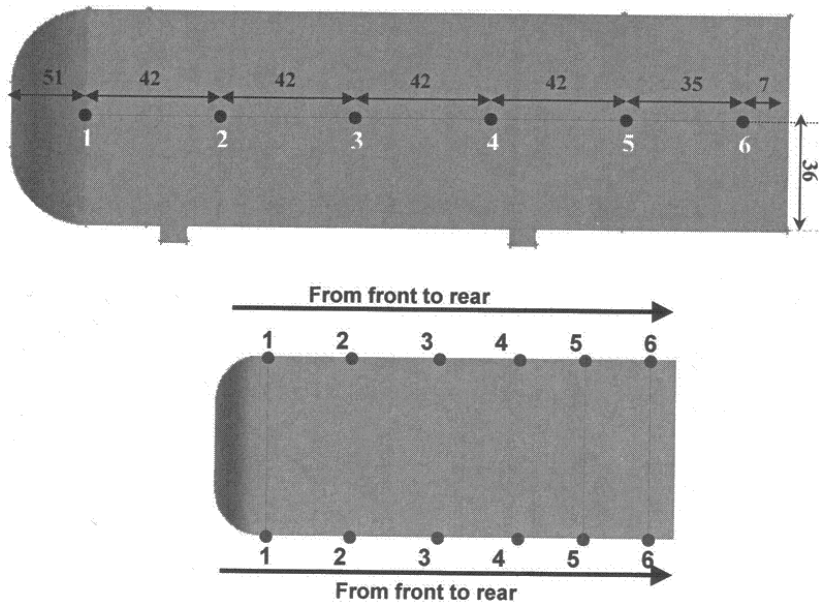
Figure D.2 Tap Locations at the Right and Left Surfaces of Ahmed Body
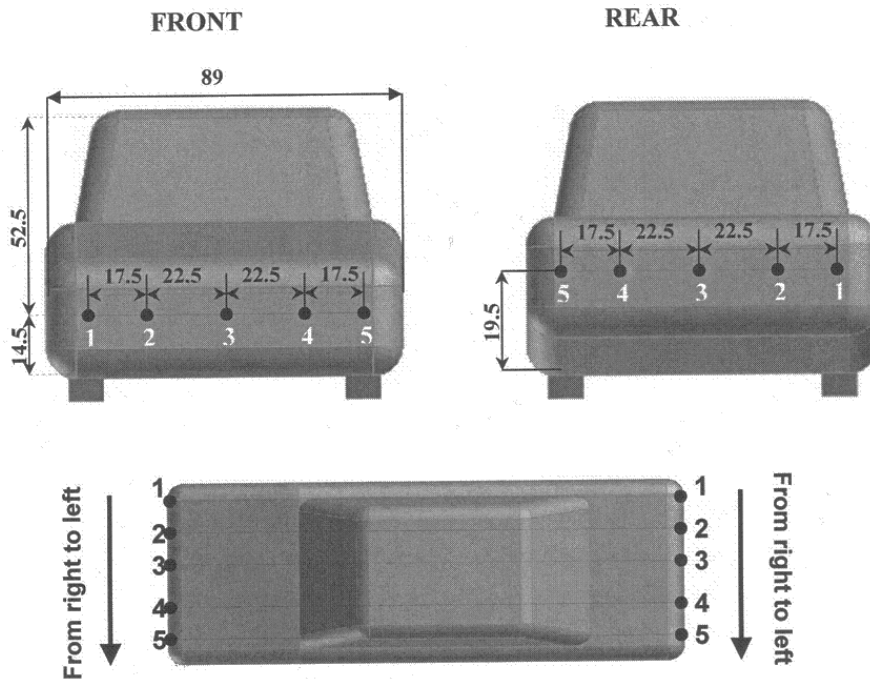
Figure D.3 Tap Locations at the Front and Rear Surfaces of MIRA Notchback Model
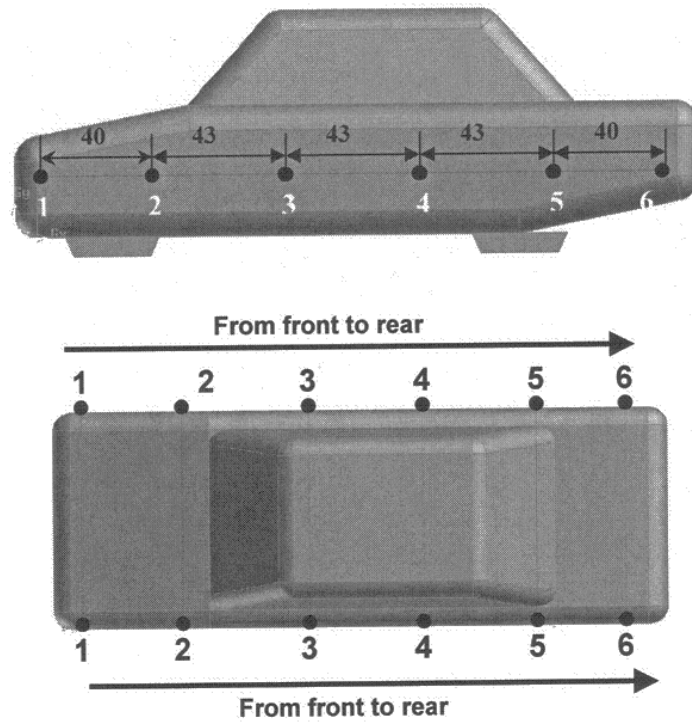
Figure D.4 Tap Locations at the Right and Left Surfaces of MIRA Notchback Model

APPENDIX E

EFFECT OF THE GROUND PLANE BOUNDARY LAYER ON DRAG MEASUREMENTS

If a flat plate is used in order to model the road surface in the wind tunnel, the boundary layer will occur. Because the vehicle moves in the air, the boundary layer does not happen on the real road surface. Hence, the boundary layer thickness of the ground plane should be minimized in the wind tunnel. On the smooth flat plate for incompressible flow, the critical Reynolds number is 500000 in the boundary layer for transition from laminar to turbulent flow.

$$Re = \frac{U_\infty x_{crit}}{\nu} \qquad (E.1)$$

Because the model was located at 1360 mm(x-coordinate) in the wind tunnel test section, the first case (5.52 m/s) can be accepted as a laminar boundary layer. However other cases (9.94 m/s and 15.11 m/s) should be considered as turbulent boundary layers.

Blasius represented a solution for two dimensional, steady and incompressible flow. This solution can be summarized as:

$$\frac{\delta^*}{x} = \frac{1.721}{\sqrt{Re_x}} \qquad (E.2)$$

According to the above equation, the displacement thickness is 3.43 mm at x=1413 mm.

For 9.94 m/s and 15.11 m/s, the critical x-values are 784 mm and 516 mm. Hence, after these points the case should be evaluated as a turbulent boundary layer. There are no precise solutions for the boundary layer in the turbulent case. However, the turbulent boundary layer outcomes can also acquired by means of an approximate momentum integral equation. This method gives below equation:

$$\frac{4}{5}\delta^{5/4} = 0.239 \left(\frac{\nu}{U}\right)^{1/4} x \qquad \text{(E.3)}$$

$$\frac{\delta}{x} = 0.379 \left(\frac{\nu}{Ux}\right)^{1/5} \qquad \text{(E.4)}$$

$$\frac{\delta}{x} = 0.379(Re_x)^{-1/5} \qquad \text{(E.5)}$$

δ^* is about 1/8 of the boundary layer thickness for the turbulent boundary layers [27]. Therefore, the displacement thickness is about 2.6 mm for 9.94 m/s and 1.7 mm for 15.11 m/s at the end of the ground plane. The ground clearances of Ahmed Body and MIRA Notchback model are 9 mm. So, ground plane boundary layer effects may be neglected.

APPENDIX F

UNCERTAINTY ANALYSIS

Experimental uncertainty estimates are applied in order to assess the confidence in the results. The uncertainties in the experiments are estimated by the following procedure.

Consider a variable X_i and its uncertainties x_i , this form is represented as

$$X_i = X_{mean_{(measured)}} \pm \delta_{x_i} \tag{F.1}$$

where,

$$X_{mean} = \frac{1}{n} \sum_{i=1}^{n} x_i \tag{F.2}$$

the standard deviation of the data set is

$$\sigma = \left(\frac{n}{n-1}\right)^{0,5} \sigma_f \tag{F.3}$$

The deviation of for a finite number of measurement is

$$\sigma_f = \sqrt{\frac{1}{n} \sum_{i=1}^{n} (x_i - x_{mean})^2} \tag{F.4}$$

The uncertainty of a result may depend on the uncertainties of the individual measured quantities and on low these quantities are combined. In general if a result Q is a function of more than one variable X_i, then the expected value Q_{mean} will be calculated through the expected values of the affecting, $X_{i_{mean}}$ and will have an overall uncertainty,

$$\delta q = \left[\left(\frac{dq}{dx_1} \delta x_1 \right)^2 + \left(\frac{dq}{dx_2} \delta x_2 \right)^2 + \cdots \right]^{0,5}$$

(F.5)

The partial derivatives of q with respect to X_i's are the sensitivity coefficients for the result q with respect to measurement X_i. When several independent variables are used in the function of q, the individual terms are combined with RSS method [35]. Then,

$$Q = Q_{mean} \pm \delta q$$

(F.6)

F.1 Uncertainty in the Drag Force

Drag force was measured by balance technique. In order to find the uncertainties in drag force measurement experiments. Uncertainty is found by using the above equations. In this study, after applying the uncertainty analysis procedure, the uncertainty was obtained for Ahmed Body ± 0.004 N and for MIRA model $\pm 0,005$ N.

F.2 Uncertainty in the Density

The density of air is a function of pressure and temperature. The uncertainty of air density is calculated by using Root-Sum Square method. Uncertainty of air density can be calculated by using Equation F.5. Air density from ideal gas relation is

$$\rho_{air} = \frac{p}{RT} \tag{F.7}$$

Uncertainty in the density was obtained as

$$\delta\rho_{air} = \pm 6.3 x 10^{-3} kg/m^3$$

F.3 Uncertainty in the Freestream Velocity

Uncertainty in the freestream velocity was obtained with below Equation of dynamic pressure

$$p_{dyn} = \rho_{air} \frac{V^2}{2} \tag{F.8}$$

$$V = \left[\frac{2p_{dyn}}{\rho_{air}}\right]^{1/2} \tag{F.9}$$

Uncertainty in the freestream velocity was calculated by

$$\delta V = \left[\left(\frac{dV}{dp_{dyn}} \delta p_{dyn}\right)^2 + \left(\frac{dV}{d\rho_{air}} \delta \rho_{air}\right)^2\right]^{0.5} \tag{F.10}$$

$$\frac{dV}{dp_{dyn}} = \frac{1}{(\rho_{air})^{0.5} (p_{dyn})^{0.5}}$$

$$\frac{dV}{d\rho_{air}} = -\frac{(p_{dyn})^{0.5}}{(\rho_{air})^{1.5}}$$

Uncertainties in the freestream velocities are shown with Table F.1.

Table F.1 Uncertainties of Freestream Velocities

V (m/s)	δV (m/s)
5.5	±0.05
9.9	±0.08
15,1	±0.09

F.4 Uncertainty in the Frontal Area

As a result of measurements of the model frontal areas, the uncertainty of the frontal area is

$$\delta A = \pm 0.0002 \ m^2$$

F.5 Uncertainty in the Drag Coefficient

Drag coefficient can be obtained by using below equation

$$C_D = \frac{D}{\frac{1}{2}\rho V^2 A} \tag{F.9}$$

Because of drag coefficient is a function of more than one variable, the uncertainty in the drag coefficient is calculated according to the Equation F.5.
The uncertainty of Ahmed Body is

Table F.2 Uncertainties of Drag Coefficients

$V\ (m/s)$	δC_d
5.5	± 0.014
9.9	± 0.055
15.1	± 0.033

The uncertainty of MIRA model is

Table F.3 Uncertainties of Drag Coefficients

$V\ (m/s)$	δC_d
5.5	± 0.016
9.9	± 0.06
15.1	± 0.03

F.6 Uncertainty in the Pressure Coefficient

$$C_p = \frac{(p_{local} - p_\infty)}{\left(\frac{1}{2}\rho U_\infty^2\right)} \tag{F.10}$$

The uncertainty in the pressure coefficient can be calculated with the Equation F.11.

$$\left[\left(\frac{\partial C_p}{\partial p}W_p\right)^2 + \left(\frac{\partial C_p}{\partial V}W_V\right)^2 + \left(\frac{\partial C_p}{\partial \rho}W_\rho\right)^2\right]^{1/2} \tag{F.11}$$

The uncertainty analyses were done for each pressure coefficient measurement. After this procedure, the uncertainties in the pressure coefficients of Ahmed Body and MIRA Notchback model were so low.

APPENDIX G

TRAVERSE MECHANISM

In this study, traverse mechanism was used to analyze the wake of reference models. Traverse mechanism was one of the ME407 projects. However, in order to use for the wind tunnel experiments and get the data with high accuracy, the traverse mechanism was improved by Ulusal Control Systems Machinery Design Co.

The traverse mechanism can be operated in x, y and z-direction. The movement of this mechanism is provided via a step motor as seen in Figure G.1.
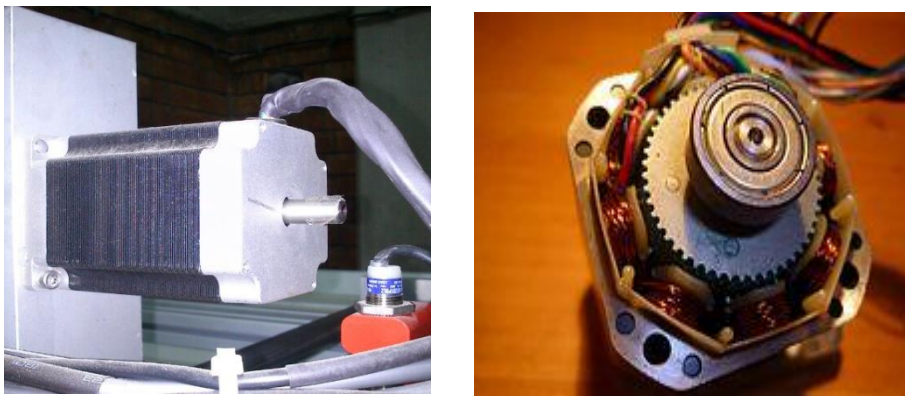

Figure G.1 Step Motor [36]

The brushless DC motor is called the stepper motor or step motor. The stepper motor completes a full rotation via equal steps. Without using feedback sensor, the position of the motor can be directed in order to move or hold at one of these steps. Step motors have electromagnets. An external control circuit energies these electromagnets. The motor shaft turn is made by electromagnets and gear.

Since the step motors were used, the speed of traverse mechanism is not fast as expected. Step motor has some disadvantages. One of them is skipping step at high operation speed. Although the step motor has disadvantages, the reason of using step motor is that it was already provided for ME407 project. In addition the step motor is suitable for used driving card.

The Toshiba TB6560AHQ is a step motor driver. Toshiba TB6560AHQ is used in order to drive step motor at low vibration and high performance forward and reverse rotation. In addition, Toshiba TB6560AHQ step motor driving card is cheap, and practical for the data acquisition process.

Traverse mechanism is operated via control panel as shown in Figure F.2. The screen is touchable and the movement of traverse mechanism in x, y and z- direction can be controlled automatically or manually.
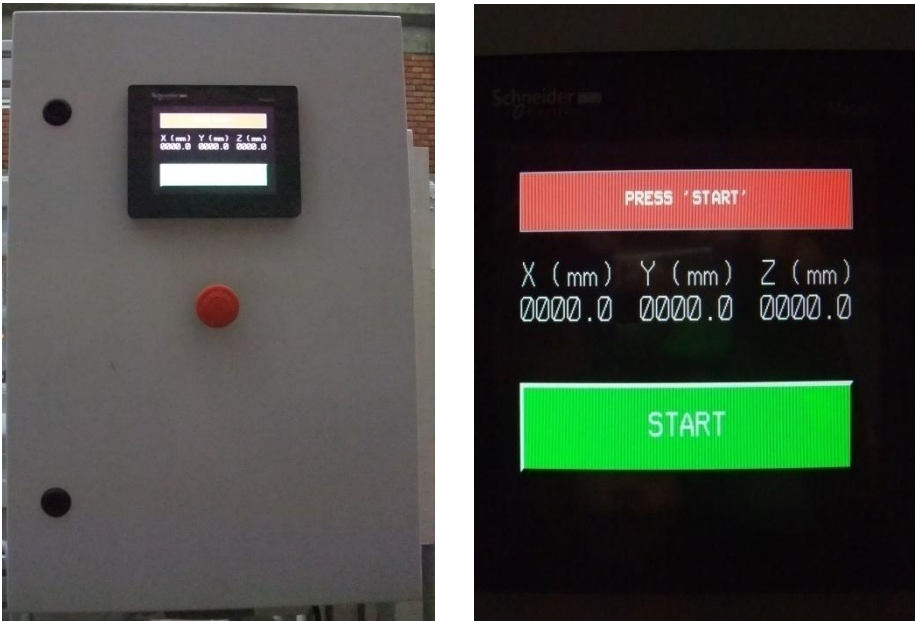

Figure G.2 Control Panel of Traverse Mechanism

When the traverse mechanism is operated, the button of 'GO HOMING' appears on the screen. The traverse mechanism goes the reference points by this button. After

completion this movement, the screen is appeared as seen in Figure G.2. The desired coordinates are typed on this screen then; the 'ENTER' and 'GO' button are touched. If the traverse mechanism is wanted to operate manually, the buttons as shown in Figure G.3 are used.
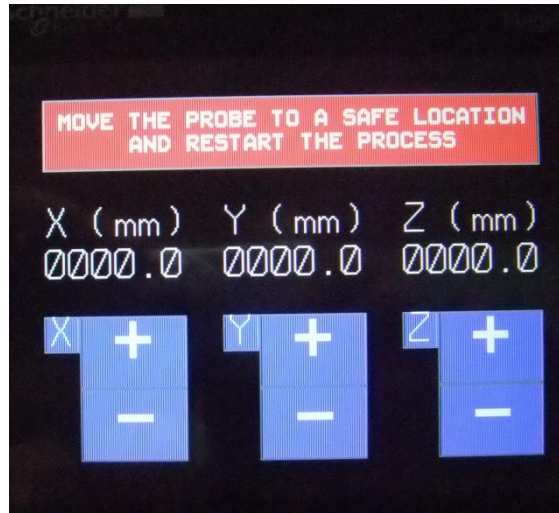

Figure G.3 Control Panel Screen

An instrument converts a physical quantity into a signal is called a sensor. The sensor is a converter. In this traverse mechanism, the sensor measures the position of the beams and converts them into a signal. These sensors have very high sensitivities. Traverse mechanism senses its movement by sensors on the mechanism beams. There are six sensors in order to perceive the locations. The sensors are indicated in Figure G.4.

Figure G.4 Sensor of Traverse Mechanism

When the traverse mechanism reaches the critical points, the traverse mechanism stops the movement and gives the alarm. After getting away from the critical position, the traverse mechanism can be operated again.

The traverse mechanism is settled in on the wind tunnel test section. For the purpose of keeping from air leakage, a cover was designed by ME407 project students. This cover is made of plexiglass. By means of this cover, the traverse mechanism can move easily at in any direction without disrupting air flow. Figure G.5 indicates the cover.
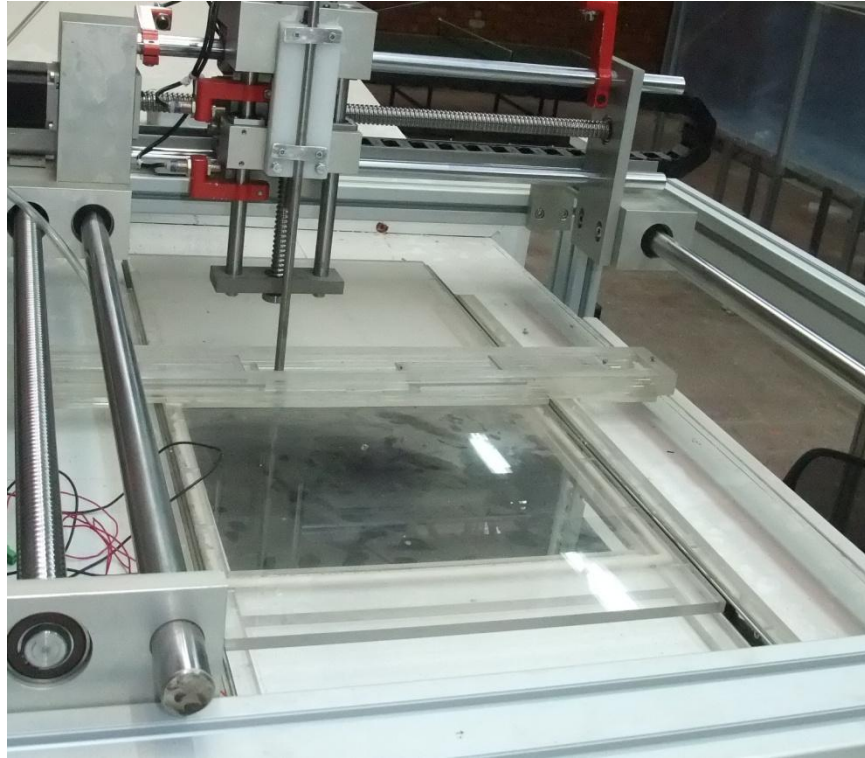
Figure G.5 The Plexiglass Cover

The traverse mechanism has heavy structure. The structure of the mechanism could damage the wind tunnel test section whether the traverse mechanism had settled in on the wind tunnel test section directly. To avoid this problem, the aluminum structure was used to load traverse mechanism around the test section as shown in Figure G.6.

Figure G.6 The Aluminum Structure of Traverse Mechanism